GEOCHEMICAL MODELING OF CARBONATES ACIDIZING WITH HCL USING TOUGHREACT

BY

MOHAMED SHERIF MOSTAFA KAMAL MAHROUS

A Thesis Presented to the

DEANSHIP OF GRADUATE STUDIES

KING FAHD UNIVERSITY OF PETROLEUM & MINERALS

DHAHRAN, SAUDI ARABIA

In Partial Fulfillment of the
Requirements for the Degree of

MASTER OF SCIENCE

In

PETROLEUM ENGINEERING

MAY 2017

KING FAHD UNIVERSITY OF PETROLEUM & MINERALS

DHAHRAN- 31261, SAUDI ARABIA

DEANSHIP OF GRADUATE STUDIES

This thesis, written by **Mohamed Sherif Mahrous** under the direction of his thesis advisor and approved by his thesis committee, has been presented and accepted by the Dean of Graduate Studies, in partial fulfillment of the requirements for the degree of **MASTER OF SCIENCE IN PETROLEUM ENGINEERING.**

Dr. Abdullah Sultan
(Advisor)

Dr. Dhafer Al Shehri
Department Chairman

Dr. Mohamed Azaroual
(Member)

Dr. Salam A. Zummo
Dean of Graduate Studies

Dr. Abeeb Awotunde
(Member)

22/3/17
Date

Dr. Abdulazeez Abdulraheem
(Member)

Dr. Mohamed Mahmoud
(Member)

© Mohamed Sherif Mahrous

2017

Dedication

To whom I am forever grateful, yet always disregardful, to the light in my life,
to my parents;
Wafaa & Sherif

ACKNOWLEDGMENTS

Looking back to this thesis work, I realize that my contribution is a small portion of the total efforts done in this work. This thesis work wouldn't have been done without the valuable inputs of several individuals who I would like to thank here.

*To my thesis advisor; Dr. Abdullah Sulta*n,
From our very first meeting, you were my fountainhead of motivation and perseverance. Somehow, no matter what difficulties we are facing, I found in our meetings the inspiration to carry on with this research work. I personally think that this is something you do intuitively, you just pass on to me a small flame of the zealous blaze, that is your soul. I can easily say that without your moral support, other than the technical support, this work wouldn't have been done the way it is presented here today. Our long meetings to the late hours of the evening are something that I will always cherish, and something that I will definitely miss.

To my committee members;
Dr. Mohamed Azaroual
I would like to acknowledge your huge contribution in this thesis work, specifically in the geochemical aspect. I would also like to thank you for your constant encouragement for me and continuous praise for my work in every skype meeting and each email correspondence. This is something that meant so much for me, coming from an industry expert like yourself. Although I learned a lot from you technically, I think what will always stick with me is what I have learned from you on a personal level. Your modest and kind personality is something that I will always look up to.

Dr. Abeeb Awotunde
Thank you for introducing me to the world of reservoir simulation.

Dr. Mohamed Mahmoud
Thank you for introducing me to the world of well stimulation.

Dr. Abdulazeez Abdulraheem
Thank you for being a part of this committee.

To the Egyptian community in KFUPM;
Thank you for making KFUPM another home for me.

TABLE OF CONTENTS

ACKNOWLEDGMENTS ..... **v**
Table of Contents ..... **vi**
LIST OF TABLES ..... **viii**
LIST OF FIGURES ..... **ix**
ABSTRACT ..... **xi**
ملخص الرسالة ..... **xiii**
CHAPTER 1 INTRODUCTION **1**
1.1. Problem Statement **5**
1.2. Thesis Objectives **8**
CHAPTER 2 LITERATURE REVIEW **9**
2.1. Mathematical Modeling of Matrix Acidizing **9**
CHAPTER 3 METHODOLOGY **21**
3.1. TOUGHREACT **21**
3.2. TOUGHREACT in Matrix Acidizing **27**
3.3. CODE COMPILATION, CALIBRATION & TESTING **28**
CHAPTER 4 REACTION ADVECTION DIFFUSION (RAD) SIMULATIONS **49**
4.1. Meshes Used in RAD Simulations **49**
4.2. Definition of the Chemical System **60**
4.3. Model Initialization **65**
4.4. Model Input Parameters **69**
4.5. Time Step Information and Breakthrough Criterion **73**
CHAPTER 5 RESULTS & DISCUSSION **77**
5.1. Two-Dimensional (2D) Simulations Results **77**
5.2. Three-Dimensional (3D) Simulations Results **87**
5.3. Effect of Aqueous Kinetics on Acidization Curve & Dissolution Patterns **89**
5.4. Pressure Decline Curve **94**
CHAPTER 6 CONCLUSIONS & RECOMMENDATIONS **97**
Appendix A: Scripts for TOUGHREACT Modules Compilation **99**
Appendix A.1. Module EOS1 Compilation Script **99**

Appendix A.2. Module ECO2N Compilation Script 99
Appendix B: Scripts for Submitting Jobs to the HPC Cluster 100
Appendix B.1. Module EOS1 Job Submission Script 100
Appendix B.2. Module ECO2N Job Submission Script 100
Appendix C: Comparison between Reported Equilibrium Constants 101
References 106
Vitae 112

LIST OF TABLES

Table 2.1 Constants Used in Previous Numerical Work..... 19
Table 3.1 TOUGH2 Modules..... 22
Table 3.2 TOUGH+ Modules and its applications..... 23
Table 3.3 TOUGHREACT Modules and its applications..... 25
Table 3.4 Chemical Composition for Calibration Problem #1..... 31
Table 4.1 List of Chemical Reactions in the HCl/Calcite System 60
Table 4.2 List of Primary and Secondary in the HCl/Calcite System..... 62
Table 4.3 Total & Equilibrium Concentrations of Primary Species for Initial Water 68
Table 4.4 Total & Equilibrium Concentrations of Primary Species for Injection Water . 68
Table 4.5 Input Parameters for Reactive Simulations..... 72
Table 4.6 Convergence Criteria for RAD Simulations 74
Table 5.1 Basic and Full Speciation Systems 90

LIST OF FIGURES

Figure 1.1 Dissolution patterns resulting from injecting Texas chalk by 0.5 M HCl. After Fredd & Fogler. 3
Figure 1.2 Typical acidization curve resulting from injecting 0.5 M HCl in limestone. After Panga. 4
Figure 1.3 A typical speciation diagram for carbonic acid 8
Figure 3.1 One-Dimensional Radial Mesh for Calibration Problem #1. 31
Figure 3.2 Comparison in CO2 Gas Saturation Distributions. 32
Figure 3.3 Comparison in pH Distributions 32
Figure 3.4 Comparison in Porosity Distributions. 33
Figure 3.5 Comparison in Dawsonite Change of Abundance Distributions 33
Figure 3.6 Comparison in Ankerite Change of Abundance Distributions 34
Figure 3.7 Replotting of figure (5.3): Comparison in pH Distributions. 34
Figure 3.8 One-Dimensional Cartesian Mesh for Advection Testing Problem #1 37
Figure 3.9 Modifications of the One-Dimensional Cartesian Mesh. 39
Figure 3.10 Pressure Distributions TOUGHREACT Against Our Calculations.. 40
Figure 3.11 Difference Between TOUGHREACT Results and Our Results for Each Grid Cell at Different Times. 40
Figure 3.12 2D Schematic of Testing Advection Problem #2.. 42
Figure 3.13 Porosity Distribution for Advection Testing Problem #2. 42
Figure 3.14 Permeability Distribution for Advection Testing Problem #2. 43
Figure 3.15 Modifications of the Two-Dimensional Cartesian Mesh. 45
Figure 3.16 Pressure Distributions at Times 0.5, 5, and 15 days of TOUGHREACT Against Our Calculations. Figures on the left represent our results, while figures on the right represent TOUGHREACT. 46
Figure 3.17 Difference Between TOUGHREACT Results and Our Results for Each Grid Cell at Different Times. 47
Figure 4.1 Two-Dimensional Mesh for Reaction Advection Diffusion Simulations 50
Figure 4.2 Porosity Distribution of the Two-Dimensional Mesh of Reaction Advection Diffusion Simulations 51
Figure 4.3 Uniform Porosity Probability Density Function of the Two-Dimensional Mesh of Reaction Advection Diffusion Simulations. 51
Figure 4.4 Permeability Distribution of the Two-Dimensional Mesh of Reaction Advection Diffusion Simulations 52
Figure 4.5 Log Normal Permeability Probability Density Function of the Two-Dimensional Mesh of Reaction Advection Diffusion Simulations 53
Figure 4.6 Schematic of the 1”x4” Core Used in Dong & Hill Experiment. 54
Figure 4.7 Three-Dimensional Mesh for Reaction Advection Diffusion Simulations. Dark grey cells represent the 1”x4” cylindrical core, while white cells represent no-flow cells. 54

Figure 4.8 Porosity Distribution of the Three-Dimensional Mesh of Reaction Advection Diffusion Simulations. 56
Figure 4.9 Uniform Porosity Probability Density Function of the Three-Dimensional Mesh of Reaction Advection Diffusion Simulations 56
Figure 4.10 Permeability Distribution of the Three-Dimensional Mesh of Reaction Advection Diffusion Simulations 57
Figure 4.11 Log Normal Permeability Probability Density Function of the Two-Dimensional Mesh of Reaction Advection Diffusion Simulations 57
Figure 4.12 Acid Inlet in Experiments (left) and Our Simulations (Right).. 59
Figure 4.13 Comparison in Reported Equilibrium Constant Variation with Temperature for Calcite Mineral Reaction from Different Thermodynamic Databases 64
Figure 5.1 Comparison Between Dissolution Patterns from Our Results (fig a), Experiemental Work (fig b), and Previous Numberical SImualtions (fig c).. 79
Figure 5.2 Acidization Curves from 2D RAD Simulations.. 84
Figure 5.3 Acidization Curve and the Resulting Dissolution Pattern as Reported Experimentally by Fredd and Fogler 85
Figure 5.4 Acidization Curve at Different Temperatures as Reported Experimentally by Bazin. Notice the one-third slope for rates above the optimum. 86
Figure 5.5 Acidization Curve Comparison Between Experimental Results and TOUGHREACT Results 88
Figure 5.6 Acidization Curve and the Resulting Dissolution Pattern for Basic and Full Speciation Simulation. 91
Figure 5.7 Effect of Different Acid Concentrations on the Acidization Curve After Wang and Hill (Left). Effect of Full Speciation and Basic Speciation on the Acidization Curve (Right). Notice the Similarity in Trends. 93
Figure 5.8 Time Evolution of Pressure Decline Curve and Dissolution Pattern at the Optimum Injection Rate. 96

ABSTRACT

Full Name : Mohamed Sherif Mahrous

Thesis Title : GEOCHEMICAL MODELING OF CARBONATES ACIDIZING WITH HCL USING TOUGHREACT

Major Field : Petroleum Engineering

Date of Degree : May, 2017

Modeling of wormholing phenomenon is one of the challenging research problems due to the complexity of the process which requires coupling of multi-phase fluid flow, species transport, and geochemistry. There is not a single model that captures all of these aspects of the wormholing phenomenon which requires further development of more accurate 3D multiphase/multiphysics models. This challenge is the principal motive for this work. The objective of this work is to model carbonate acidizing more accurately from a geochemical point of view. All previous numerical models consider only the acid/rock reaction and the transport of hydrogen ions only. In this work, we also account for chemical reactions between the aqueous species, including the dissolved CO_2, under full-speciation transport. This is done using TOUGHREACT; a code for reactive modeling of non-isothermal multiphase flow of fluids in physically and chemically heterogeneous porous and fractured media. This code solves the Reaction-Advection-Diffusion (RAD) equation not only for Hydrogen ions, but also for all other primary species. Coupling of transport and reaction equations is done using a Sequential Non-Iterative Approach (SNIA). Aqueous kinetics are assumed at equilibrium, while rock/acid reaction is kinetically constrained. Single-phase 2D & 3D simulations of HCl injection in limestone rock are performed under a linear flow

geometry. Results of the full speciation simulations are validated with previous experimental work, and compared with results from previous numerical models. This has been accomplished with special focus on the treatment design parameters; optimum injection rate, and volume of acid injected to achieve breakthrough.

The simulations results show that; 1) the full-speciation model captures the different dissolution patterns reported experimentally, 2) confirm the existence of an optimum injection rate that corresponds to minimum volume of acid injected, 3) the dissolved CO_2 and aqueous kinetics affects the treatment design parameters. We believe that performing these more geochemically accurate simulations is another step forward towards fully capturing the complex wormholing phenomenon.

ملخص الرسالة

الاسم الكامل: محمد شريف مصطفى كمال محروس

عنوان الرسالة: نمذجة جيوكيميائية لإذابة حمض الهيدروكلوريك للكربونات بإستخدام "TOUGHREACT"

التخصص: هندسة البترول

تاريخ الدرجة العلمية: مايو 2017

ان نمذجة الاذابة الحمضية للنسيج الصخري تعتبر مشكلة بحثية ذات تحدي كبير لكونها عملية معقدة تطلب دمج الجيوكيمياء، تدفق الموائع متعددة الحالات، الجيوميكانيكا و انتقال المجموعات الكيميائية. حتى الان، لا يوجد نموذج يحتوى على كل الجوانب السابق ذكرها لدراسة ظاهرة الثقب الدودي في الصخور و لذلك يتطلب هذا تطوير اضافي لنماذج اكثر دقة ثلاثية الابعاد متعددة الفيزياء و الحالات. ان كل النماذج السابقة التي حاولت دراسة الاذابة الحمضية للنسيج الصخري فرضت تدفق احادي الحالة متجاهلين تأثير ثاني اكسيد الكاربون الناشيء. في هذه الدراسة، تم استخدام كود "TOUGHREACT" الجيوكيميائي للمرة الاولى لمحاكاة اذابة الصخور الكربونية عن طريق حمض الهيدروكلوريك. يتميز هذا الكود بقدرته على الاخذ في الاعتبار تأثير ثاني اكسيد الكربون المذاب. يتم هذا عن طريق حل معادلة التفاعل-التأفق-الانتشار لآيونات الهيدروجين و المجموعات الكيميائية الاساسية، كما تم دمج معادلات الانتقال و التفاعل باستخدام اسلوب تسلسلي غير تكراري. اعتبرت حركية التفاعل المائية في حالة اتزان، اما حركية تفاعل الصخر مع الحمض تم تحديدها حركيا. تم استخدام "TOUGHREACT" لمحاكاة ثنائية و ثلاثية الابعاد لتدفق احادي ديكارتي لحقن حمض الهيدروكلوريك في معدن الكالسيت. اظهرت النتائج قدرة الكود "TOUGHREACT " في ادراك نماذج الاذابة المختلفة التي اقرت سابقا عن طريق التجارب، كما اظهرت المحاكاه المسار المقعر لاعلي لمنحنى الاذابة الحمضية. علاوة على ذلك، بينت الدراسة ان ثاني اكسيد الكربون المذاب يتحد مع ايون الهيدروجين مكونا حمض الكربونيك مما يقلل من تركيز الحمض الفعال في عملية الاذابة الحمضية.

CHAPTER 1

INTRODUCTION

Matrix acidizing is the process of injecting acids into the formation, to restore or improve the formation permeability, thus enhancing the oil or gas production[1]. After the well is drilled, some of the drilling fluid filtrate penetrates the formation to a certain depth, reducing its permeability and creating a "damaged" zone surrounding the well. The injected acids dissolve the formation rock, creating new flow paths that pass or "breakthrough" the damaged zone. These new flow paths create a highly conducting flow channels for the hydrocarbons to flow through the damaged zone to the well, thus increasing the oil and gas productivity.

Difference should be made between matrix acidizing and another common acidizing treatment; matrix fracturing. In matrix acidizing, the acid is injected at a pressure lower than the fracture pressure of the formation, which is the pressure that yields stresses on the formation higher than the formation compressive strength, resulting in the formation breakdown and creation of fractures in the formation. However, matrix fracturing injects acids at a pressure higher than the formation fracture pressure to purposefully fracture the formation.

In matrix acidizing, the shape of the newly created flow paths, named dissolution patterns, is determined by the level of rock heterogeneity and two rates; the rate of acid mass transfer to the rock surface, and the rate of reaction between the rock and the acid once the acid reaches the rock surface. The rate of acid transfer to rock is determined by the acid injection rate. The rate of reaction between the rock surface and the acid, also known as surface reaction kinetics, is function

of the reaction conditions of pressure, temperature and acid concentration. The two rates are conveniently expressed as a dimensionless quantity named Damköhler number (N_{Da}), which is the ratio between these two rates, defined as:

$$N_{Da} = \text{Reaction rate/Mass transfer rate} = aD^{\frac{2}{3}} \frac{l}{Q}$$

$$N'_{Da} = \kappa \pi d \frac{l}{Q} = \frac{1+\frac{1}{\nu K_{eq}}}{\frac{1}{K_1}+\frac{1}{k_r}+\frac{1}{K_{eq}K_2}} \pi d \frac{l}{Q}$$

Where "a" is a constant that depends on the carbonate core, "D" is the diffusion coefficient, "l" is pore length, "Q" is the flow rate. While N'_{Da} is the modified Damköhler number, with "d" as the pore diameter. κ is the overall dissolution rate constant, K_{eq} is the surface reaction equilibrium constant, k_r is the effective forward reaction rate constant, and K_1 and K_2 are the mass transfer coefficients for reactants and products.

There are three main types of dissolution patterns; (1) face dissolution, (2) wormhole, and (3) uniform dissolution, arranged in a decreasing magnitude of Damköhler number, shown in Figure (1.1). Some investigators[2, 3 & 4] prefer to subdivide the “wormhole” dissolution pattern into: (2a) conical wormhole, (2b) dominant wormhole, and (2c) ramified wormhole, all of which are shown in Figure (1.1) as well.

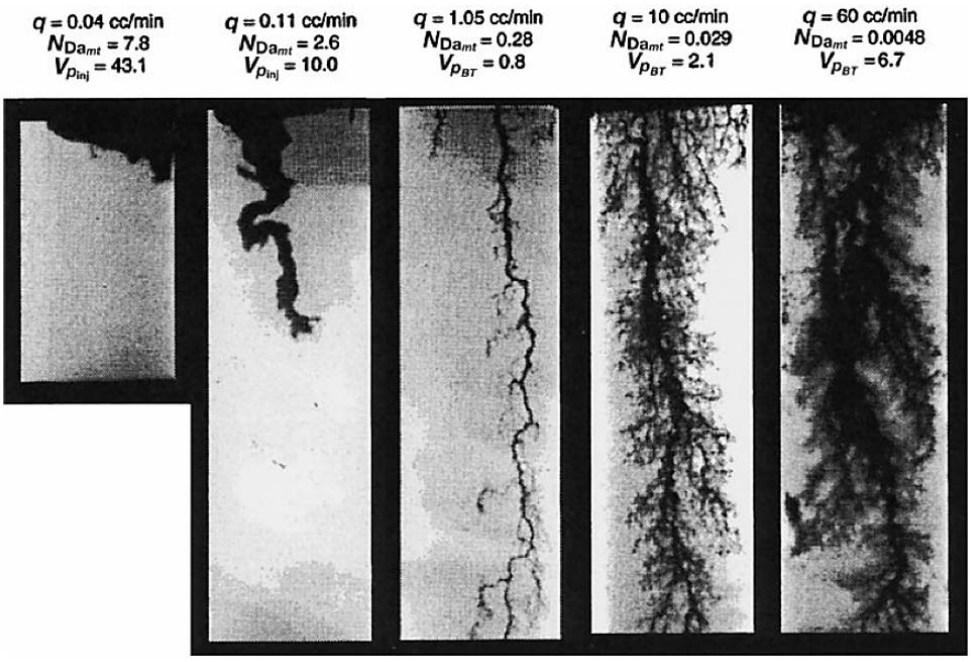

Figure 1.1 Dissolution patterns resulting from injecting Texas chalk by 0.5 M HCl (from left to right); (1) face dissolution, (2a) conical wormhole, (2b) dominant wormhole, (2c) ramified wormhole, and (3) uniform dissolution. After Fredd & Fogler[5].

The dissolution pattern that breaks through the damaged zone with minimum total volume of acid injected, is the "wormhole" dissolution pattern. The name "wormhole" is after the burrows created by earthworms in soil, due to the resemblance of the patterns created by the worms and acid injection. This "wormhole" pattern occurs at an optimal injection rate. Other dissolution patterns are not desirable in matrix acidizing because they either cannot break through the damaged zone or they consume larger amounts of acid to breakthrough.

As matrix acidizing became more common in the oil and gas industry, numerous experiments were conducted to find out the optimum injection rate. To best represent the findings of the matrix acidizing experiments, a plot of total volume of acid injected to breakthrough versus acid injection rate, named "acidization curve", is drawn. A typical acidization curve is shown in Figure (1.2). All

acidization curves exhibit the concave upward behavior, indicating the presence of an optimal injection rate; the rate that corresponds to minimum acid volume required to breakthrough.

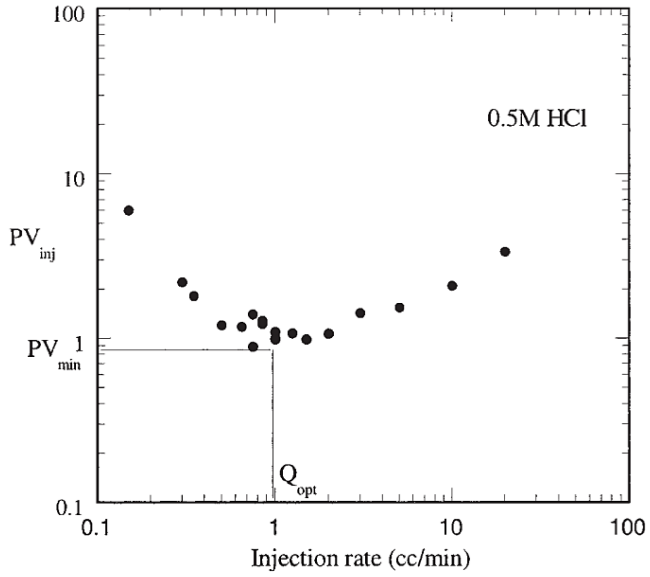

Figure 1.2 Typical acidization curve resulting from injecting 0.5 M HCl in limestone. After Panga[6]. Notice that the optimum injection rate is identified at the minimum volume injected to breakthrough.

However, many of the experimentally obtained optimum injection rates, when scaled up to field conditions, failed to secure a successful treatment and the oil or gas productivity wasn't enhanced. In an attempt to explain this discrepancy, as well as find the optimum injection rate for different rock/acid interactions without the need for setting up more expensive and time-consuming experiments, modeling of the wormhole phenomenon was introduced. The Models tackled different flow geometries (radial and linear flows in 1D, 2D & 3D) and different rock/acid combinations. However, all the models simulating the wormhole propagation assumed single-phase flow, as seen from the next section.

1.1. Problem Statement

In carbonate formations, hydrochloric (HCl) acid (usually 15% by weight) in water is the type of acid used in matrix acidizing. The acid reacts with the limestone ($CaCO_3$) of the formation according to the equation:

$$2HCl + CaCO_3 \rightarrow CaCl_2 + H_2O + CO_{2\,(g)} \uparrow + \text{Heat}$$

The reaction equation clearly states that CO_2 gas is evolved as a result of the reaction between the HCl acid and the limestone. All previous models simulated wormholes as a single phase phenomenon by assuming that all of the evolved CO_2 is dissolved in the injected acid. This raises the question about the CO_2 solubility limit in acids. More importantly, all previous models didn't account for the effect of the dissolved CO_2 on the rock/acid interactions.

1.1.1. Carbon Dioxide Solubility in Acidic Solutions

Unfortunately, data on solubility of CO_2 in solutions of acids in water, specifically HCl in water, is not available in the literature. However, literature on CO_2 solubility in pure water is abundant. Since the injected acid in carbonates is only 15% HCl by weight and the rest is water, one can use data on CO_2 solubility in pure water to find approximate solubility values for CO_2 solubility in acidic solutions[1].

The solubility of CO_2 in water is function of pressure, temperature, water pH, and amount of dissolved solids in water. The CO_2 solubility in water decreases as the temperature increases and as the pressure decreases. The solubility also decreases as pH value decreases, and amount of dissolved solid in water increases.

The CO_2 solubility in pure water at a pressure of 10,000 psi (70 MPa) and a temperature of 60°F (15°C) is about 0.091 kg CO_2/kg H_2O [6] (about 3.6 mol% [7]). From the reaction stoichiometry, one mole (44 grams) of CO_2 is produced for each 2 moles (2x36.5 grams) of HCl. Thus, for the all of the evolved CO_2 to be completely soluble in the acid, the required solubility should be 0.09 grams of CO_2/grams of 15%wt HCl; the quotient of the 2 masses multiplied by 0.15 to account for HCl being only 15% by weight of the injected fluid. So, even at these very optimistic conditions of pressure and temperature, the CO_2 solubility in water is just about enough to dissolve all of the evolved CO_2.

But in reality, the reservoir temperature is much higher than 60°F, the pressure can be lower than 10,000 psi, and the pH is lower than the pH of 7 of pure water (because of the added acid), and the water contains dissolved solids (as tap water, not pure water, is used in the field). All of this decreases the CO_2 solubility even more. And thus not all CO_2 will dissolve in the acid and it may exist as a separate phase, either in a gaseous or a supercritical phase depending on the pressure and temperature conditions.

1.1.2. Carbon Dioxide Speciation in Acidic Solutions

When carbon dioxide gas dissolves in water, it forms carbonic acid (H_2CO_3), according to the equation;

$$H_2O + CO_{2\,(g)} \rightarrow H_2CO_3$$

Carbonic acid is a weak diprotic acid. It is a weak acid because it rarely dissociates completely in water, and it is diprotic because it is capable of donating two hydrogen ions when it completely dissociates in water, as follows;

Carbonic acid loses when hydrogen ion and transforms into a bicarbonate ion (HCO_3^-);

$H_2CO_3 \rightarrow H^+ + HCO_3^-$

The bicarbonate ion loses another hydrogen ion and transforms into a carbonate ion (CO_3^{-2});

$HCO_3^- \rightarrow H^+ + CO_3^{-2}$

The above three chemical equations actually describe a single multi-step reaction, that is the dissolution of CO2 in water, and can be combined as follows;

$$H_2O + CO_{2\,(g)} \rightleftharpoons H_2CO_3 \rightleftharpoons H^+ + HCO_3^- \rightleftharpoons 2H^+ + CO_3^{-2}$$

decreasing H^+ concentration or increasing pH

The resulting species, whether aqueous carbonic acid (H_2CO_3), Bicarbonate ion (HCO_3^-), or carbonate ion (CO_3^{-2}), depends on the solution pH. At low pH, the solution is rich with H^+ ions, so the solution shifts to the direction of low H^+ ions concentration to achieve equilibrium, according to Le Chatelier's principle, and most of dissolved CO_2 exists as aqueous carbonic acid (H_2CO_3). At high pH, the solution is poor with H^+ ions, so the solution shifts to the direction of high H^+ ions concentration, again according to Le Chatelier's principle, and most of dissolved CO_2 exists as carbonate ion (CO_3^{-2}). At intermediate pH, most of the dissolved CO_2 exists as Bicarbonate ion (HCO_3^-). This is shown in the CO_2 speciation diagram in Figure 1.3. In this diagram, the y-axis is the mass fraction of each species present. We note that the shape of the diagram can change with the solution conditions; salinity, pressure, and temperature. From the above discussion, we would like to point out that:

1- The assumption made by previous models that all evolved CO_2 is dissolved in the injected acid might not be true, as the CO_2 solubility in acidic solutions is very limited.

2- The dissolved CO_2 changes the hydrogen ions concentration in the solution, which are the driving force for the acid/rock reaction. These effects are not accounted for in any of the previous models.

The question remains here, to what extent the assumption that CO_2 dissolve in the acid affects the accuracy of the wormholing models? The answer to this question is the main objective of this work.

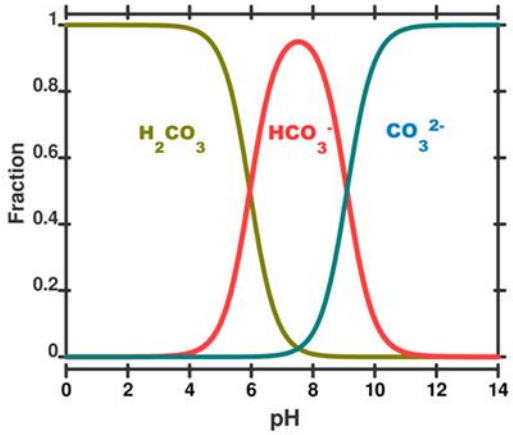

Figure 1.3 A typical speciation diagram for carbonic acid

1.2. Thesis Objectives

The objectives of this thesis work are:

1. To model carbonate acidizing more accurately from a geochemical point of view, using full chemical speciation and thermodynamic data in 2D and 3D linear flow geometries.
2. To validate the new model against experimental results
3. To introduce carbonates acidizing as a new application for TOUGHREACT

CHAPTER 2

LITERATURE REVIEW

2.1.Mathematical Modeling of Matrix Acidizing

A Mathematical Model is a representation of a behavior of a system using a set of mathematical equations. Similar to any mathematical model[8], mathematical models of matrix acidizing can be divided into:

1. Analytical Models
2. Semi-Empirical Models
3. Statistical (Stochastic) Models
4. Numerical Models

One can say that the way we deal with the set of mathematical equations that describes the system defines the type of model. If we seek an exact solution to the equations, then our model is analytical. If we solve for an approximate solution, then the model is numerical. If we simplify the equations with the aid of experimental data, then the model is semi-empirical. If we neglect the physics behind the equations and dealt with the system as a stochastic one, then the model is statistical.

2.1.1. Analytical Models

They are models in which we find a “closed form” solution to the set of mathematical equations that describe our system behavior. A “closed form” solution is the solution that can be expressed

as an analytic function, or more simply, and more importantly, it is the exact solution, thus the most accurate solution. Although analytical modeling provides accurate solutions, it has two crucial drawbacks. First, not all problems have analytical (exact) solutions. Second, the analytical solution is not easy to obtain. Moreover, the difficulty of obtaining the analytical solution increases with the complexity of the equations to be solved. Thus, when analytical modeling is to be used for complex phenomena, one must simplify the mathematical equations. This is done by making several assumptions till the system of equations is reduced to its elements and can be solved analytically.

When applied to the highly complex phenomenon of wormholing, the mathematical model had to be oversimplified to be solved analytically. This led to the failure of the models to quantitatively estimate the system parameters. However some of these models, as the models by Yuan[9], Hung's mechanistic model[10], Huang[11 & 12], and Istchenko[13], helped give guidance to the designing of matrix acidizing treatments.

2.1.2. Semi-Empirical Models

Empirical models are the models created solely by experimental data points. These points are then plotted, then either interpolated to find an equation that passes through all the points and thus fully describe the system behavior, or fitted to find an equation that best pass through all the points and thus closely describe the system behavior.

Empirical models excel in describing systems in which the interdependence of the systems variables is very limited, except for two variables, the relationship between them is required to be found. Since usually this condition is not satisfied, the relationship between each two variables is found while keeping other system variables constant. Another major drawback of empirical models

is that loses its ability to quantitatively estimate the system parameters, especially if the system parameters are varied significantly when compared to the parameters used to create the data points. The large number of parameters in the wormholing phenomenon and the high dependence of the matrix acidization variables on each other, as well as the need of a quantitatively accurate model to predict the optimum injection rate, deemed empirical modeling inapt for a complex phenomenon as matrix acidizing.

This gave rise to an amalgam of empirical and analytical modeling, named semi-empirical models. Semi-empirical models use experimental data to simplify the analytical model. An example of how experimental data can be used to simplify the analytical model is the assessment of the significance of an assumption made to simplify the model, as neglecting a parameter. If the parameter was experimentally found to be of considerable significance, then experimental data is used to estimate this parameter and feed it numerically to the model. If not, the parameter is neglected. Gong [14] and Buijse[15] used this type of mathematical modeling to simulate the wormholing phenomenon.

2.1.3. Statistical (Stochastic) Models

Statistical models are based on the assumption that the behavior of the system to be described is stochastic, i.e. purely random. In this type of models, a set of probability distributions is established from another set of experimental observations. Once this set of probability distributions is made, single-value parameters are input to give rise to a distinct probability distribution, from which the system behavior can be determined. However, a major disadvantage of these models is that it almost completely neglect the physical laws of the system, as the system is treated as a complex statistical problem.

The use of statistical modeling in matrix acidizing was an early attempt to tackle the tedious task of physically interpreting the complex phenomenon of wormholing propagation and developing mathematical equations that fully describe it. This was later encouraged by the experimental work of Daccord [16] who discovered the fractal nature of wormholes and described it as an "instable" phenomenon. The wormholing phenomenon was assumed to be of a stochastic nature in the models created by Pichler [17] and Xiaogang [18].

2.1.4. Numerical Models

They are models in which we find an approximate solution to the exact (analytical) solution of the set of mathematical equations that describe our system behavior. This done usually using one of the "finite" methods, namely; finite difference method, finite volume method, and finite element method. There are two main disadvantages associated with the numerical models. First, they are not exact solutions. They are just an approximation. Second, they are computationally expensive, specially, when the system of equations becomes non-linear. The first disadvantage is not a problem as long as the error between the numerical and exact solutions is within the accepted tolerance. This error tolerance is relatively large in most engineering applications and for most practical purposes. The second disadvantage was solved with the advancement in computers processing speed. On the other side, numerical models had an advantage over analytical models. Unlike analytical models, numerical models can solve complex mathematical description of physical systems without the need to oversimplify the mathematical equations. Also another advantage of the numerical models over all other types of mathematical models is its ability to allow for field of inputs, instead of single-value input used in the other models.

Once applied in wormholes modeling, numerical models proved to be the most successful type of mathematical models to best quantify the wormholing phenomenon parameters. Thus, it will be reviewed in more details.

Numerical Models of, not only matrix acidizing modeling, but also any geochemical reactive transport modeling, can be divided into [19]:

I. Pore-Scale Models

II. Continuum Models

III. Multiple Continua Models

The main difference between these different numerical models is the scale used to describe the behavior of the system. If the system is described on a microscopic pore level, i.e. in micrometers, then it is a pore-scale model. If the system is described on a macroscopic Darcy level, ranging from micrometers to centimeters, then it is a continuum model. However, if we describe the system with different characteristic length scales, then we need the multiple continua model. This model combines different continuum models, thus it is also known as hybrid models.

I. Pore-Scale Models

These models capture the reactive flow transport and chemical reactions in each individual pore space and between each two interconnected pore spaces. The most two common types of pore-scale models are pore network model and lattice Boltzmann model. While the latter has the advantage of being able to express the processes that might take place on a sub-pore scale, and thus being more rigorous modeling approach, it is computationally expensive. This limits the

lattice Boltzmann model to simple chemistry systems and very small scale problems. Thus, it was never used in modeling of the wormholing phenomenon.

In pore-network modeling, pores are represented as 3D shapes, usually spheres, called nodes. The size of the node is comparable to the size of the pore. In case of taking nodes as spheres, the radius of each sphere is taken equal to the average pore radius that the sphere represents. The connection between one pore to another is represented by tube of radius comparable to the pore throat radius. Thus, the physical system of pores and throats is converted to a network of nodes, hence the name pore-network modeling. Because of its tolerable computational power, there were several attempts to capture wormholing with these models as the models by Hoefner[20], Fogler[21], Yuan[22], Buijse[23] and Tansey[24]. Daccord [25 & 26] also created his capillary-tube model, in which he considered the matrix as a bundle of capillary tubes, hence the name. The flow inside these tubes is oversimplified by assuming it follows Poiseuille's law. While some of these pore-scale models managed to capture the experimentally observed dissolution patterns, they all overestimated the breakthrough pore volume.

II. Continuum Models

These models average the system parameters in an elementary control volume of a macroscopic length (Darcy scale; ranging from micrometers to centimeters). If the characteristic length scale of the system we are trying to model is of pore dimension (micrometers or smaller), then continuum model is null due to the averaging of the system parameters. The use of an elementary control volume follows that all the phases of the system co-exist as a single point in space, and that all the reactions are considered homogeneous with constant reaction rate in each grid at each time step.

The various simplistic assumptions of the continuum models and the need to capture many pore-scale parameters in the wormholing phenomenon, made the continuum models ill-suited to modeling of wormholing. Nevertheless, few attempts were made to use the continuum models by Golfier[4] and Cohen[27]. The reliability of continuum models was highly doubted when Li[28] showed that these models can yield large errors and it is, sometimes, unable to capture the correct direction of reaction.

III. Multiple Continua Models

These models are used in systems that integrate several characteristic length scales, where usage of single continuum or pore models leads to significant errors. Each characteristic length scale is formulated as a separate continuum as if it is the only scale to be modeled and it is a one-continuum model. Then, the continuum of each scale is coupled to the continua of the neighboring scales.

The use of multiple continua model in wormhole modeling is indispensable as wormholing occur at two characteristic length scales; the pore (micrometers) scale and the core (Darcy) (from micrometers to centimeters) scale. This derived the creation of a two-scale continuum model that couples the pore and Darcy scales.

Following is a detailed review of the work done using two-scale continuum models to describe the wormholing phenomenon.

In 2003, Panga [29] filed a patent for a "two-scale continuum model for wormhole formation during matrix stimulation for carbonates." The model couples the Darcy and pore scales through "the structure-property relationships (permeability-porosity, average pore size-porosity, and interfacial area-porosity) and the dependence of the fluid phase dispersion coefficient on the evolving pore scale variables (average pore size, local Reynolds and Schmidt numbers)." The model [30 & 31] was

run for 1D and 2D linear single-phase simulations. The runs showed the qualitative trends of optimum injection rates versus pore volumes of acid injected. Also, it showed a good quantitative match with the experimental work of Golfier[4].The 2D simulation managed to capture the different dissolution patterns characteristic of acid injection.

Kalia[32] used Panga's model to simulate wormhole formation in carbonate rocks for a 2D radial single phase flow. Qualitatively, their model matched the experimental work in the dissolution patterns and that a minimum level of heterogeneity must exist for the wormhole pattern of minimum pore volume to occur. Quantitatively, their model matched the experimental work in the fractal dimension of the wormhole pattern and that the wormhole length is function of (t^b); injection time raised to the power of an exponent (b). More importantly, Kalia's simulation runs found out that the optimum injection rate is function of the model aspect ratio; ratio between the inner and external radius (r_o/r_e). In these simulation runs, the model input porosity and permeability fields was calculated using semi-empirical correlations as the modified Carmen-Kozeny relation. Heterogeneity was introduced by adding uniformly distributed random fluctuations. To improve this model, Kalia suggested to use better structure-property relations that is based on experiments.

This led Izgec[33] to investigate the effect of heterogeneity on wormhole propagation. They flooded vuggy carbonate cores of 20 inches in length and 4 inches in diameter with 15% (by volume) HCl acid. They performed CT (Computed Tomography) scans on the cores before and after the acid flooding. The scans mapped the vugs and were used to feed the input of the simulation model. The simulation was for 3D linear single phase model. The model couples the Darcy and pore scales using the Darcy-Brinkman formulation. The model obtruded the effect of large scale heterogeneity (heterogeneity with vugs and/or fractures) on fluid flow by assuming the fluid to be non-reactive with the porous media. Nevertheless, the model showed that the "non-reactive" fluid created a

wormhole-like flow path. From which, the authors derived their main conclusion; large scale heterogeneities as vugs and fractures presides the propagation of wormholes not the chemical interaction between the rock and fluid. This is due to the small pressure drops across the vugs that makes the fluid prefer the flow paths of largest total volume of vugs. An ensuing conclusion is that wormholes propagation is much faster to breakthrough in vuggy carbonates than in homogeneous ones. Experimentally, they found that vuggy carbonates require number of pore volumes to break through that are an order of magnitude less than that of homogeneous carbonates.

As the effect of heterogeneity appeared to become more prominent. Liu[34] used Panga's model to create 2D radial single phase flow simulation of wormholes propagation with normally distributed porosities. They compared their work to that of Kalia who used uniformly distributed porosity fields. On comparison, it was found that a normally distributed porosity field has less breakthrough volume, thinner wormholes, larger number of wormholes, and faster wormhole propagation than uniformly distributed porosity field.

Liu[35] also used his previous simulation runs (2D radial single phase flow) to investigate the wormholes fractal nature. The model calculated the fractal dimension with an acceptable error ranging from 6 to 10% when compared to the experimentally measured fractal dimension of Daccord and Lenormand [25 & 26]. They made the runs for both weak and strong acids. On comparison, weak acids had lower optimum injection rate, wider wormholes and consumed more acid than strong acids. This matches the experimental results as the reaction between the rock and acid is reaction controlled in case of weak acids, and it is mass transfer controlled in case of strong acid.

Ratnakar[36] took modeling of wormholes to another level by modeling the non-Newtonian in situ cross-linked acids. They used Panga's model that assumes Newtonian behavior of the simulated

fluids, and tackled the non-Newtonian behavior using an empirical rheological model. The model gives viscosity as a function of temperature, shear rate, and pH. They also developed expressions for width and propagation speed of gel and reaction fronts as a function of these rheological parameters. Integrating the empirical model with Panga's model, the authors created 1D, 2D & 3D linear single phase flow simulation of wormholes propagation due to in situ cross-linked acids injection in carbonates. Matching what was found experimentally, the authors found that in-situ cross-linked acids had lower optimum injection rates and more branched wormholes than Newtonian acids.

Maheshwari[2] revisited the effect of heterogeneity with a more general approach by performing a sensitivity analysis of rock properties as initial average permeability and permeability–porosity relationships. He used Panga's model to create 3D linear single phase simulations. He found that less permeable carbonates has lower breakthrough pore volume and higher optimum injection rate than more permeable carbonates.

Building on his previous work, Maheshwari[37] modified Panga's model by used a new structure-property relation (the structure-property relation is one of the relations that couples the pore scale with the Darcy scale). Integrating two new parameters, pore-broadening and pore-connectivity, the new structure-property relation can relate pores radii, interfacial area per unit volume, and changes in permeability with change in porosity. The simulation was for 1D, 2D, and 3D linear single phase flow. The dissolution patterns of matrix acidization were all identified. A good match was obtained between the model acidization curve and the one made experimentally by Fredd and Fogler[5].

Maheshwari[38] extended the work of Ratnakar on non-Newtonian acids, by modeling wormholes propagation due to the injection of gelled and emulsified acids in carbonates. The simulation was

for 3D linear single phase flow. When compared to neat (Newtonian) HCl acid, gelled and emulsified acids had thinner wormholes and lower breakthrough volumes. Also, gelled and emulsified acids exhibited wider range of injection rates that yield the optimum wormhole dissolution pattern.

Ghommem[3] used Panga's model to create a 3D linear single phase simulation of wormhole propagation due to HCl injection in carbonates. When compared to a series of acid core-flooding experiments that they conducted, the model captures qualitatively the dissolution patterns and quantitatively the breakthrough pore volume. Their true contribution to the literature is that they introduced a novel concept for real-time monitoring and control of matrix acidizing using resistivity logs. In this new approach, the resistivity measurements are informative of the type of the acidizing regime and can be used to estimate the depth and speed of wormhole penetration. This is done by combining the acidizing model with Archie's law to evaluate the variations in the resistivity resulting from the dynamic change in the porosity and fluid conductivity during the dissolution process. Table (2.1) lists some of the constants used in previous numerical simulations.

Table 2.1 Constants Used in Previous Numerical Work

Paper	**Reaction Rate Constant**	**Diffusion Coefficient**	**Reactive surface area**	**Viscosity**
Ghommem (2016)	0.5 cm/s	$3.6x10^{-9}$ m^2/s	50 cm^{-1}	1 cp
Maheshwari (2016)	N/A	N/A	50 cm^{-1}	N/A
Golfier (2002)	N/A	$2x10^{-9}$ m^2/s	N/A	1 cp
Cohen (2008)	10 s^{-1}	2 $x10^{-9}$ m2/s	N/A	N/A

Our main point of interest in reviewing the literature is to note that all of the models that ever attempted capturing the wormholing phenomenon assumed that only acid is present. The models argued that any carbon dioxide produced by the reaction of HCl acid with carbonates is dissolved in the solution. In reality, sometimes natural gas is present as a separate phase, also at least a residual oil saturation is present if the rock is oil-wet, and CO_2 can exist as a separate phase that is either gaseous or supercritical phase depending on the pressure and temperature conditions. More importantly, this single phase assumption adopted by all previous models didn't account for the effect of the dissolved CO_2 on the rock/acid interactions, as mentioned earlier.

CHAPTER 3

METHODOLOGY

All reactive fluid flow simulations were done using "TOUGHREACT"; a code for reactive modeling of non-isothermal multiphase flow of fluids in physically and chemically heterogeneous porous and fractured media.

3.1. TOUGHREACT

The code is a part of the “TOUGH” software suite developed by the Earth Sciences Division in Lawrence Berkley National Laboratory for U.S. Department of Energy. This suite consists of the following codes;

3.1.1. TOUGH2:

TOUGH2 is a simulator for non-reactive non-isothermal multiphase flow in porous and fractured media developed in FORTRAN 77. It was originally developed for geothermal reservoir studies and high-level nuclear waste isolation. TOUGH2 is considered the father of the TOUGH software suite, meaning that other softwares in this suite was developed by modifying/improving the TOUGH2 code. TOUGH2 has 18 different modules, each module serves a different application. Table (3.1) lists the modules of TOUGH2, as well as the possible application of each module and the components transported.

Table 3.1 TOUGH2 Modules

TOUGH2 Module	Components	Application
EOS1	water, water with tracer, heat	Basic module for geothermal applications
EOS2	water, CO_2, heat	Near-surface, gaseous CO_2 applications
EOS3	water, air, heat	Vadose zone applications
EOS4	water, air, heat	Same as EOS3, including vapor pressure lowering effects
EOS5	water, hydrogen, heat	corrosion-gas producing waste repositories
EOS7	water, brine, air, heat	For multiphase, density-driven flows where salinity does not reach saturation levels
EOS7R	water, brine , air, radionuclide1, radionuclide2, heat	Same as EOS7, with parent-daughter radionuclides
EOS7C	water, brine, NCG (CO_2 or N_2), tracer, CH_4, heat	Applicable to CO_2 or N_2 in natural gas (CH_4) reservoirs
EOS7C-ECBM	water, brine, NCG (CO_2 or N_2), tracer, CH_4, heat, with ECBM isotherm and Dusty Gas Model	Same as EOS7C, with extended Langmuire isotherm for simulating enhance coal-bed methane, and the Dusty Gas Model for gas-phase diffusion
EOS8	water, air, oil, heat	Oil component is not volatile nor soluble, i.e., it is present only in the nonaqueous phase liquid (NAPL) phase, i.e. dead oil.
EOS9	water	Uses Richards equation instead of Darcy's law to model saturated-unsaturated flow
EOS9nT	water	Same as EOS9, but capable of transport of multiple, non-volatile solutes/colloids; radioactive decay (including ingrowth), adsorption, advection/diffusion/dispersion, filtration, colloid-assisted tracer transport, first-order chemical reaction

EWASG	water, NaCl, NCG (CO_2, air, CH_4, H_2, N_2), heat	Applicable to geothermal reservoirs with saline fluids and a noncondensible gas; temperature-dependent NaCl solubility; includes salt precipitation and dissolution
ECO2N	water, brine, CO_2	Geologic CO_2 sequestration in saline aquifers; CO_2 in gaseous, liquid and supercritical phases; no crossing of saturation line; salt precipitation and dissolution
ECO2M	water, brine, CO_2	Multiphase version of ECO2N; includes transition between super and sub-critical conditions, and phase change between liquid and gaseous CO_2
T2VOC	water, air, volatile organic compound (VOC), heat	Environmental applications
TMVOC	water, volatile organic compound (VOC), noncondensible gas (NCGs)	Same as T2VOC with the capability of simulating one or multiple noncondensible gas (NCGs)

3.1.2. TOUGH+:

TOUGH+ is the same as TOUGH2 with new capabilities added developed in FORTRAN 95. The most important added capability in TOUGH+ is its ability to simulate water freezing and thawing. This was done by extending the range of thermodynamic properties of water to include ice. TOUGH+ has 2 modules, each module serves a different application. Table (3.2) lists the modules of TOUGH+, as well as the possible application of each module.

Table 3.2 TOUGH+ Modules and its applications

TOUGH+ Module	Application
TOUGH+RGB	Simulates behavior of gas-bearing geologic formations. RGB is short for Real Gas Brine.

TOUGH+Hydrate	Simulates behavior of hydrate-bearing geologic formations, including formation and dissociation of ice-like hydrates with associated changes in porosity, permeability, and two-phase flow characteristics.

3.1.3. TOUGH2-MP:

TOUGH2-MP is a parallelized version of TOUGH2. It was developed for running on distributed-memory parallel computers to solve large simulation problems that may not be solved by the standard, single-CPU TOUGH2 code. MP is short for Massively parallel.

3.1.4. iTOUGH2:

Short for inverse TOUGH2, iTOUGH2 is a computer program that provides inverse modeling capabilities for the TOUGH codes. iTOUGH2 solves the inverse problem by automatically calibrating a TOUGH2 model (or any other model) against observed data. Any TOUGH2 input parameter can be estimated based on any observation for which a corresponding TOUGH2 output can be calculated. An objective function measures the difference between the model calculation and the observed data, and a minimization algorithm proposes new parameter sets that iteratively improve the match. Once the best estimate parameter set is identified, iTOUGH2 performs an extensive error analysis, which provides statistical information about residuals, estimation uncertainties, and the ability to discriminate among model alternatives. Furthermore, an uncertainty propagation analysis allows one to quantify prediction errors.

3.1.5. TOUGHREACT:

This code is yet another upgrade for the TOUGH2 code, in which reactive geochemistry was introduced to the already existing framework of multiphase fluid and heat flow. The first version of the TOUGHREACT code was released to the public through the US Department of Energy

Science and Technology Software Center (ESTSC) in August 2004. The code was developed in FORTRAN 77. Interactions between mineral assemblages and fluids can occur under local equilibrium or kinetic rates. The gas phase can be chemically active. Precipitation and dissolution reactions can change formation porosity and permeability.

TOUGHREACT has 7 different modules, each module serves a different application. Table (3.3) lists the modules of TOUGHREACT, as well as the possible application of each module and the components transported.

Table 3.3 TOUGHREACT Modules and its applications.

TOUGHREACT Module	Components	Application
EOS1	water, water with tracer, heat	Basic module for hydrothermal applications
EOS2	water, CO2, heat	hydrothermal gaseous CO2 applications
EOS3	water, air, heat	vadose zone and nuclear waste disposal applications
EOS4	water, air, heat	Same as EOS3, including vapor pressure lowering effects
EOS7	water, brine, air, heat	Same as EOS3, including density and viscosity effects of salinity, and density-driven flows where salinity does not reach saturation levels
EOS9	water	Uses Richards equation instead of Darcy's law to model saturated-unsaturated flow, with typical applications to ambient temperature and pressure reactive geochemical transport problems, as in the case of Vadose zones.
ECO2N	water, brine, CO2	Geologic CO2 sequestration in saline aquifers; CO2 in gaseous, liquid and supercritical phases; no crossing of saturation line; salt precipitation and dissolution

ECO2M *(Underdevelopment)*	water, brine, CO2	Multiphase version of ECO2N; includes transition between super and sub-critical conditions, and phase change between liquid and gaseous CO2

TOUGHREACT has already been used in over 180 research papers in a wide variety of geological and environment-related subsurface applications, including, but not limited to;

1. Subsurface nuclear waste emplacement
2. Contaminant transport
3. Acid mine drainage remediation
4. Diagenetic processes
5. Carbon dioxide underground storage
6. Groundwater quality
7. Geothermal systems
8. Scale formation prediction in injection wells

Other than the aforementioned applications, TOUGHREACT can be used to simulate a variety of subsurface thermophysical–chemical processes under a wide range of conditions of pressure, temperature, water saturation, ionic strength, and pH and Eh. The exact range of conditions varies with the module used. For instance, the module ECO2N can be applied for pressure ranging from 1 bar (14.7 psi) to around 600 bars (8700 psi), temperature from 32 to 570^{o}F (from 0^{o}C to 300^{o}C), and any value of pH and Eh.

3.2. TOUGHREACT in Matrix Acidizing

In the published literature, the code was never used before in simulation of matrix acidizing. However, it was used in simulation of carbonates dissolution due to injection of CO_2 saturated water to store and sequester CO_2 underground[44–50]. The main objective of these models is to study the petrophysical and geochemical effects of CO_2 sequestration in carbonate formations. In some of these simulations, wormholes were captured. This is because CO_2 dissolution in water yields the weak carbonic (H_2CO_3) acid. The carbonic acid dissolves the carbonates of the formation in a similar way, but at a much slower rate, as the strong hydrochloric acid dissolves carbonates.

This encouraged us to try using TOUGHRERACT in wormhole modeling due to HCl acid injection in carbonates. The latest version of TOUGHREACT, named "TOUGHREACT V3.0-OMP", was purchased by the department of petroleum engineering at King Fahd University of Petroleum and Minerals (KFUPM) on 12th February 2016, along with all of the modules listed in Table 3.3. The code license is under the name of the thesis advisor; Dr. Abdullah Sultan. The "V3" in TOUGHREACT V3-OMP is short for version 3. "OMP" is short for Open Multi-Processing, which is an API (application programming interface) that supports multiplatform shared memory multiprocessing programming. This OpenMP parallelization allows for much faster performance on multi-core shared memory computers.

3.3. CODE COMPILATION, CALIBRATION & TESTING

As we are attempting a new application to the code TOUGHREACT in simulating matrix acidizing of carbonates with HCl acid, the code had to be treated with utmost scrutiny. This was done on three separate phases:

1. Code compilation.

2. Code calibration.

To ensure proper code compilation, the code was calibrated against a published paper that used TOUGHREACT before. In the code calibration phase, we use exactly the same input as the input used in the paper, then compare the results we obtain with the published results.

3. Code testing.

TOUGHREACT only recognizes no-flow boundary condition. To ensure the code capability of simulating other special boundary conditions, the code is tested in simulating water advection under special boundary conditions for both homogenous and heterogeneous formations.

3.3.1 Code Compilation

TOUGHREACT was compiled using Intel® Parallel Studio XE OpenMP compiler. Appendix A is the script used for compiling the modules EOS1 (Appendix A.1) and ECO2N (Appendix A.2).

All TOUGHREACT runs were made on a High Performance Computing (HPC) E1350 Cluster, regulated by the Information Technology Center (ITC) at King Fahd University of Petroleum & Minerals. The cluster is operated by Red Hat Enterprise Linux 5 operating system. This cluster has 128 compute nodes. Each node has a 4GB RAM and a dual processor. Each processor is a Xeon E5405 2.0 GHz Quad-Core.

The number of cores to be used in each run is determined by the user. In parallel processing, the computation time decreases with increasing number of cores. This is because the total processing speed increases with increasing number of cores. However, the computation time doesn't continue to decrease with increasing number of cores indefinitely. The computation time reaches a minimum at which the number of cores is the optimum, then starts to increase as the number of cores increases further. This is because at some point each core is fast enough to solve more calculations than it takes to spread them out over many cores. In this work, we used 1, 2, 4, 8, or 16 cores depending on the problem size. Appendix B is the script used for submitting jobs to the HPC for the modules EOS1 (Appendix B.1) and ECO2N (Appendix B.2). In these scripts, the number of nodes to be used is assigned the variable "N".

After the code is compiled, we calibrate the code against previous a well-tested problem. This is done in the next section.

3.3.2 Code Calibration

As mentioned earlier, code calibration serves as checks and benchmarks to verify proper code installation. In this section, we calibrate the compiled code by trying to replicate the results of a previous work.

3.3.2.1 Calibration Problem #1: CO2 Underground Sequestration in Deep Formations

Problem Description:

The calibration problem is a carbon dioxide (CO_2) underground storage problem. Carbon dioxide storage/sequestration is the process of injecting CO_2 into geological formations to store and trap CO_2 underground. The purpose of this process is to prevent the release of CO_2 into the atmosphere. This reduces air pollution, mitigates the greenhouse effect, and defers global warming. By far, especially in large quantities, this method of disposing CO_2 is the most successful way to prevent the detrimental effects of atmospheric CO_2.

Xu[52] utilized TOUGHREACT to simulate CO_2 disposal in a Gulf Coast sediment from the USA. The general purpose of this type of simulations is to study the petrophysical and geochemical perturbations resulting from CO_2 storage. Another purpose is to get a rough estimation of the amounts of CO_2 that can be sequestered beforehand.

Model Description:

Xu[52] modeled the CO_2 disposal site with a 1-D radial mesh. The inner boundary of the mesh is the injection well and the outer boundary is a constant pressure boundary. The radial grid consists of 49 grid cells. The grid cells sizes increase logarithmically, then linearly, then logarithmically again, away from the well. Figure (3.1) shows the 1D radial mesh. The circles in the figure represents the centers of the 49 grid cells of the mesh.

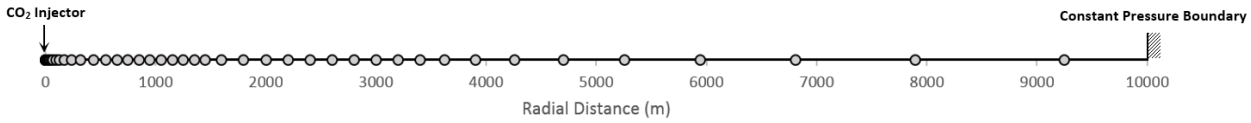

Figure 3.1 One-Dimensional Radial Mesh for Calibration Problem #1. Circles represents the centers of the grid cells.

The formation is assumed homogeneous with a porosity of 0.3, permeability of 100 md, and a uniform thickness of 100 m. The formation consists mainly of quartz (56%) and oligoclase (20%) minerals. Table (3.4) lists a detailed mineralogical composition of the formation. Initial formation water was assumed in equilibrium with 1 M NaCl solution. Initial conditions are 75^{o}C and 200 bar (2900 psi). CO_2 is injected at a constant rate of 90 kg/s for 10 years non-stop. Simulation run time is 1000 years.

Table 3.4 Chemical Composition for Calibration Problem #1

Mineral	Chemical Composition	Wt.%
quartz	SiO_2	56
oligoclase	$CaNa_4Al_6Si_{14}O_{40}$	20
K-feldspar	$KAlSi_3O_8$	8
smectite-Ca	$Ca_{0.145}Mg_{0.26}Al_{1.77}Si_{3.97}O_{10}(OH)_2$	4
clinochlore	$Mg_5Al_2Si_3O_{10}(OH)_8$	3
daphnite	$Fe_5Al_2Si_3O_{10}(OH)_8$	2
kaolinite	$Al_2Si_2O_5(OH)_4$	2
calcite	$CaCO_3$	2
illite	$K_{0.6}Mg_{0.25}Al_{1.8}(Al_{0.5}Si_{3.5}O_{10})(OH)_2$	1
organic	CH_2O	1
hematite	Fe_3O_3	1

Results Comparison:

Figures from 3.2 to 3.6 shows a comparison in the distributions of CO_2 gas saturation, pH, porosity, changes in Dawsonite mineral ($NaAlCO_3(OH)_2$), and changes in Ankerite mineral ($Ca(Fe,Mg,Mn)(CO_3)_2$), at different times, between results we obtained and that of Xu. In these figures, our results are shown on the left, while Xu results are shown on the right.

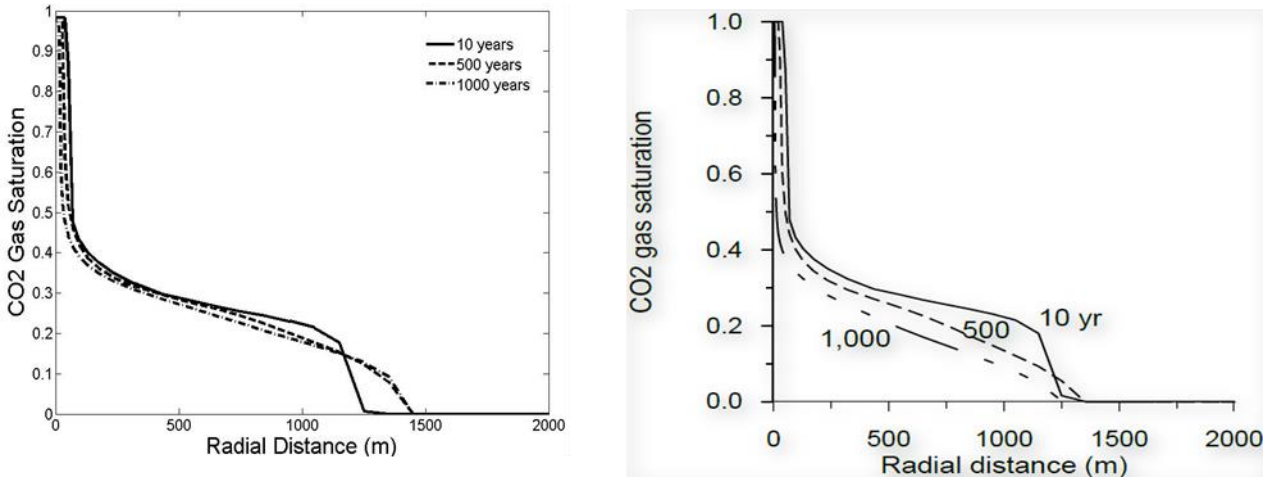

Figure 3.2 Comparison in CO2 Gas Saturation Distributions at Times 10, 500, and 1000 years between our results (left figure) and Xu (right figure).

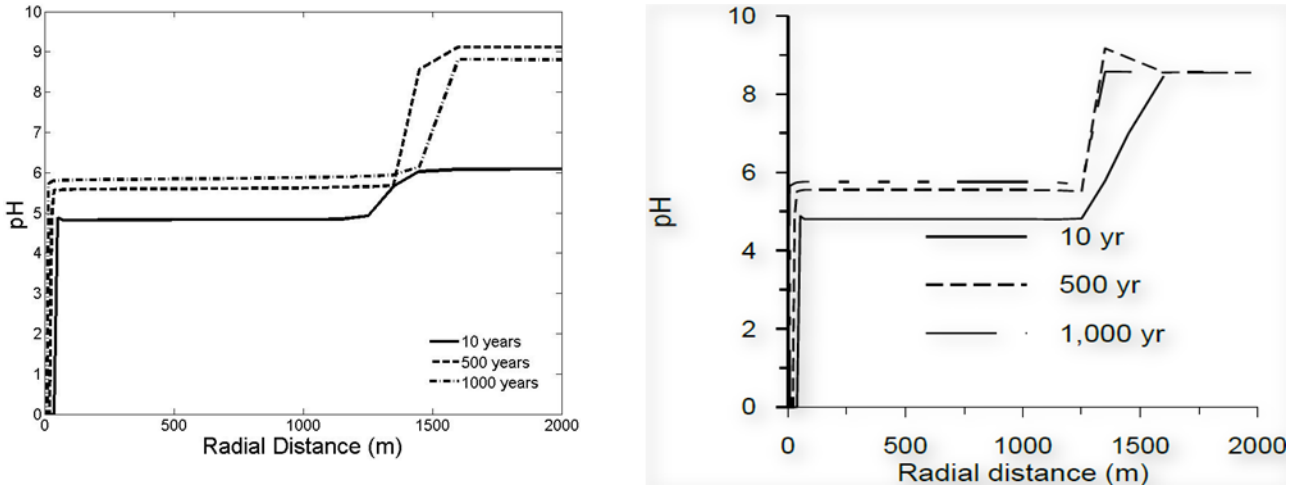

Figure 3.3 Comparison in pH Distributions at Times 10, 500, and 1000 years between our results (left figure) and Xu (right figure).

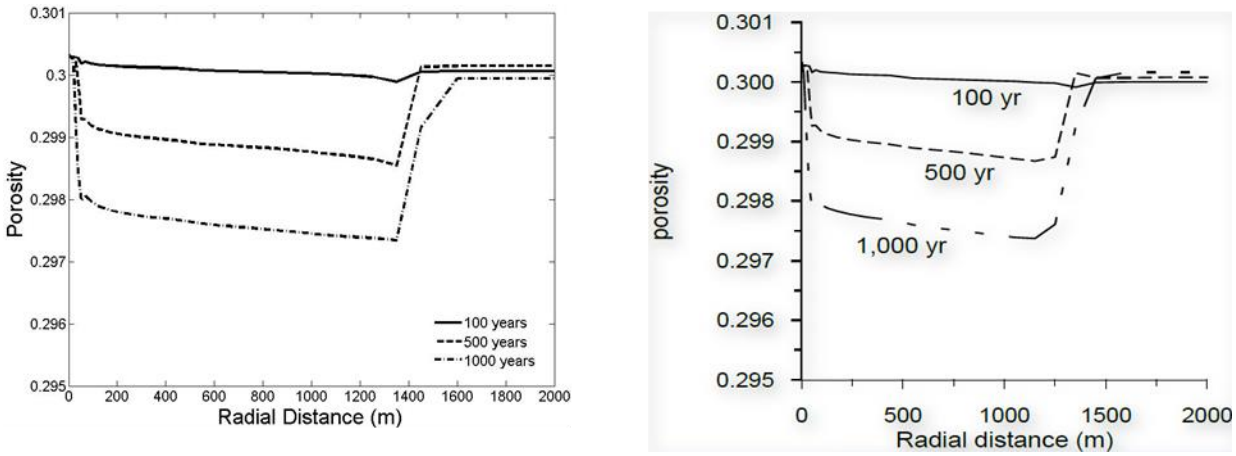

Figure 3.4 Comparison in Porosity Distributions at Times 100, 500, and 1000 years between our results (left figure) and Xu (right figure).

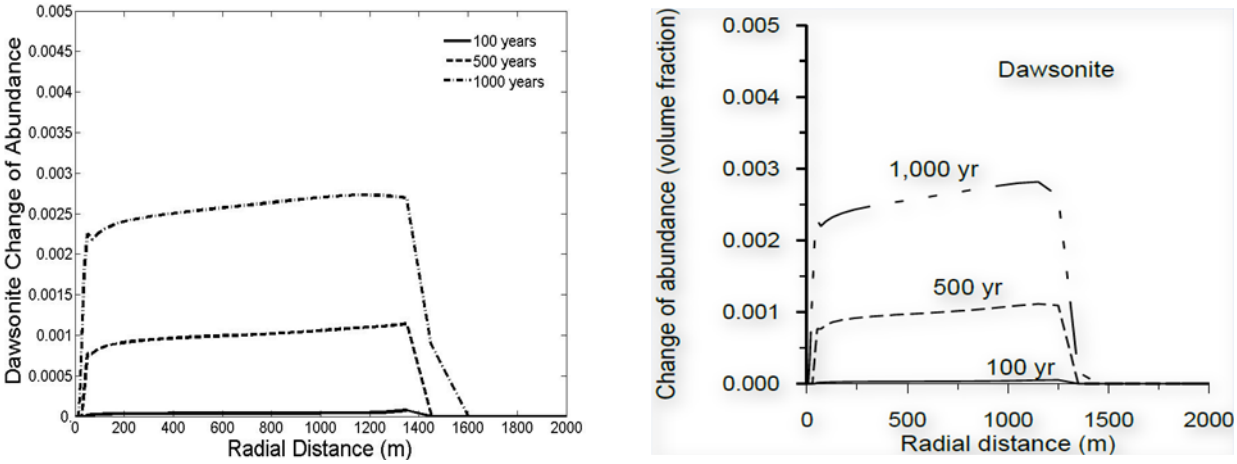

Figure 3.5 Comparison in Dawsonite Change of Abundance Distributions at Times 100, 500, and 1000 years between our results (left figure) and Xu (right figure).

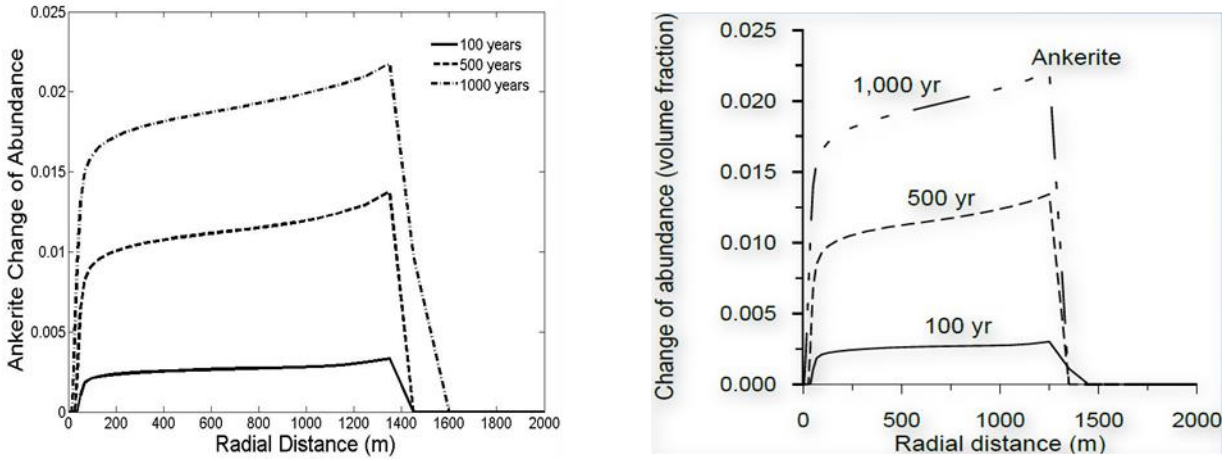

Figure 3.6 Comparison in Ankerite Change of Abundance Distributions at Times 100, 500, and 1000 years Between our Results (Left Figure) and Xu (Right Figure).

By comparing the two results in each figure, there is a good qualitative match, in general. However, there is a mismatch at radii greater than 1300 meters. While this mismatch is small in all the figures, it is relatively large in pH distributions (Figure 3.3), specifically at time 10 years. We suspect that this is a typo in the legend. The legend should be 100 years instead of 10 years. By plotting pH distribution at 100 years (Figure 3.7) we get a better match. This supports the typo postulation.

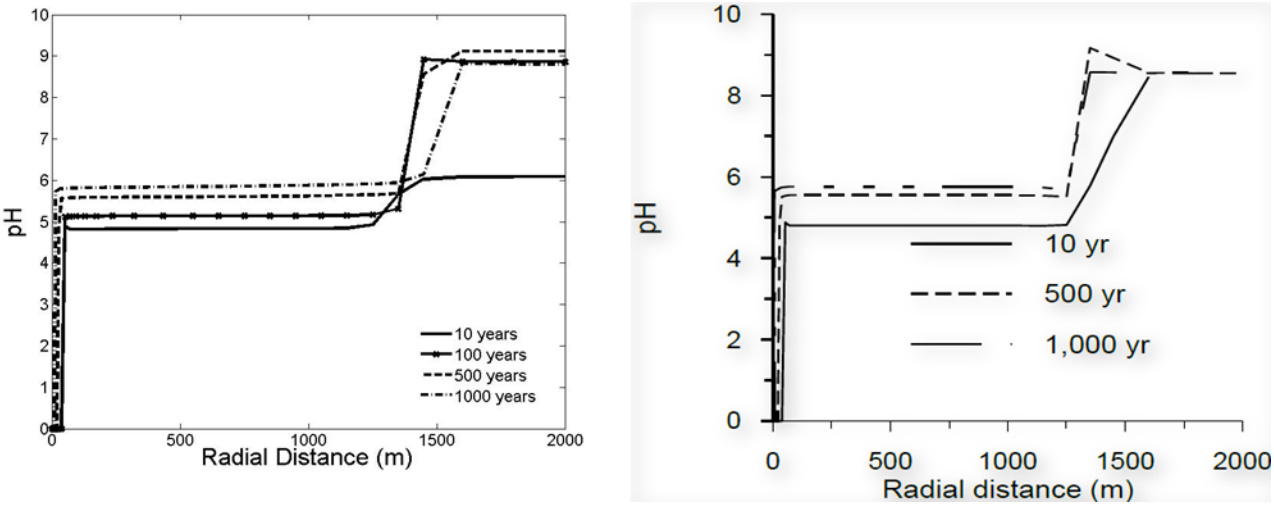

Figure 3.7 Replotting of figure (3.3): Comparison in pH Distributions at Times 10, 100, 500, and 1000 years between our results (left figure) and Xu (right figure).

The small mismatch in the rest of the figures can be attributed to:

1. Difference in TOUGHREACT versions used.

In his research paper, Xu[52] used an older version of TOUGHREACT, either V1.0 or V2.0, while we used V3.0. TOUGHREACT V3.0 has many improved formulations and bug fixes when compared to older versions.

2. Difference in time step information used.

Time step information is not mentioned in Xu[52]. We used an initial time step of 0.1 second, and doubled the time step size if convergence occurs in less than 5 iterations. The difference in time step information can yield small differences in results at each time step. In very long time-scale simulations (as in this problem), these small differences at each time step can add up to large differences in aqueous concentrations, mineral abundances, and porosity changes at later times.

If there is one thing to learn from this is the sensitivity of the reactive modeling results to time-stepping, it is advisable to run several simulations at smaller maximum time-steps to make sure that the results don't change significantly as the time step changes. Nevertheless, the match between the results was considered a good match, and calibration of TOUGHREACT was deemed successful.

3.3.3 Code Testing

The objective of this section test ability of TOUGHREACT to simulate advection with special boundary conditions in both homogenous and heterogeneous formations.

3.3.3.1 Testing Advection Problem #1: Homogeneous Formation

Problem Description:

The first testing problem is water production from a homogeneous aquifer. The west (left) boundary is a constant water influx boundary of 150 bbl/day, and the east (right) boundary is a constant pressure boundary of 5000 psi. Aquifer length, width, and thickness are 1200, 200, and 80 ft, respectively. The aquifer has a producer with a constant water production rate of 300 STB/day. Formation has a porosity of 0.2, a permeability of 50 md, and a compressibility of 0.000002 psi^{-1}. Formation fluid is water with 0.9 cp viscosity and 1.3 bbl/STB formation volume factor.

Our Model Description:

The problem described above represents advection of water (slightly compressible fluid) in a homogeneous porous medium. Thus, it can be modeled using the single-phase pressure transient flow equation of a slightly compressible fluid in a linear one-dimensional reservoir, given by;

$$\frac{\partial}{\partial x}\left(\frac{KA}{\mu B}\frac{\partial p}{\partial x}\right)\Delta x + q_{sc} = \frac{V_b \emptyset C_t}{B}\frac{\partial p}{\partial t}$$

Where p is pressure, K is permeability, A is cross-sectional area, B is formation volume factor, μ is water viscosity, q_{sc} is production rate, V_b is bulk volume, ∅ is porosity, and C_t is formation total compressibility.

The aquifer was modeled with a simple 1-D Cartesian mesh. The aquifer length is discretized into 4 grid cells, each with a constant spacing (Δx) of 300 ft. Figure 3.8 shows the 1D model. The above equation was solved numerically using a fully implicit finite difference scheme, yielding a system of linear equations. A script in MATLAB was written to solve the system of linear equations. Simulation run time is 5 days with a constant time step of 0.1 days.

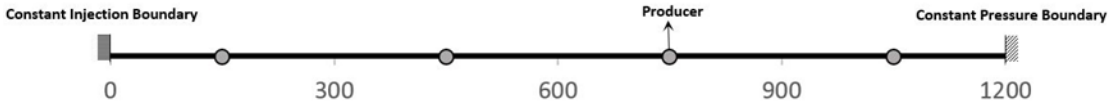

Figure 3.8 One-Dimensional Cartesian Mesh for Advection Testing Problem #1. Circles represents the centers of the grid cells.

Model Input in TOUGHREACT:

To simulate the same problem in TOUGHREACT, the exact parameters of the problem described above was input in TOUGHREACT, using the module EOS1. Unfortunately, as mentioned earlier, TOUGHREACT accepts meshes with only one type of boundary condition, that is a no-flux (sealed) boundary. To simulate the constant injection and pressure boundaries of the aquifer described above, the mesh has to be modified, as follows;

1. To simulate a constant injection boundary, an additional grid block is added, that has an injector with the same injection rate as the constant influx boundary. This added grid has an infinitesimal volume, usually several orders of magnitude smaller than the main domain grids. For instance, in the aquifer described above, each of the four grids of the main domain has a volume of $0.1359x10^{6}$ m^3 [= (Δx)(Δy)(Δz) = 300ft *x* 200ft *x* 80ft]. The infinitesimal grid cell that represents the constant injection boundary has a volume of $0.1359x10^{-6}$ m^3, i.e., it has a volume that is 12 orders of magnitude smaller than the main

domain cells. Also, the nodal distance from this infinitesimal grid cell center to the boundary was modified to a very small value of $1x10^{-9}$ m.

2. To simulate a constant pressure boundary, an additional grid block is added, that has an initial pressure equal to the pressure of the constant pressure boundary. This added grid has an infinite volume, usually several orders of magnitude larger than the main domain grids. In the aquifer problem described above, while each of the four grids of the main domain has a volume of $0.1359x10^{6}$ m^3, the infinite grid cell that represents the constant pressure boundary has a volume of $1x10^{50}$ m^3. Also, the nodal distance from this infinite grid cell center to the boundary was modified to a very small value of $1x10^{-9}$ m.

Thus, the 4-grid cell mesh with a constant injection boundary on the left and a constant pressure boundary on the right was simulated as a 6-grid cell mesh with an infinitesimal grid cell on the left and an infinite grid cell on the right. Figure 3.9 shows the modifications done on the mesh to simulate the special boundaries, as described above.

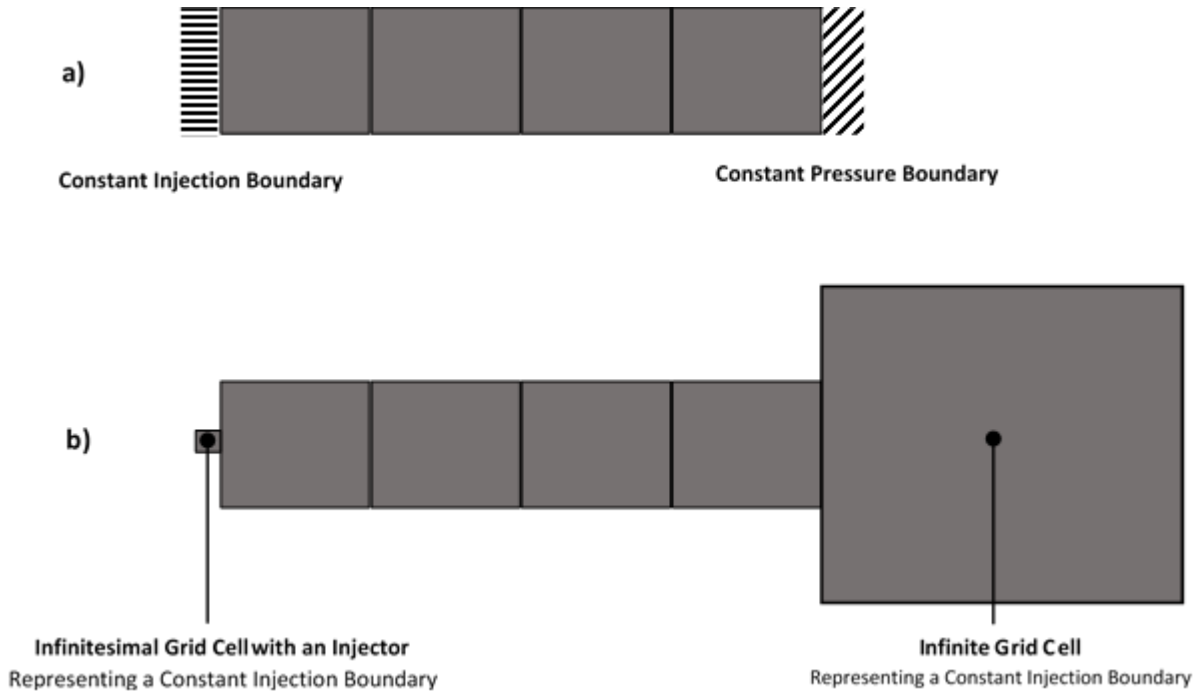

Figure 3.9 Modifications of the One-Dimensional Cartesian Mesh for Advection Testing Problem #1. Figure 3.9(a) shows the main mesh with the special boundary conditions depicted. Figure 3.9(b) shows the modifications done to simulate these boundary conditions.

Results Comparison:

Figure 3.10 shows a comparison in the results between the pressure distribution from our results and that of TOUGHREACT. While the results might seem identical, there is a slight difference in calculated pressures from TOUGHREACT and our results. Figure 3.11 shows the difference in calculated pressure between TOUGHREACT and our results ($\Delta P = P_{TOUGHREACT} - P_{Our\ Results}$) for each grid block. The maximum difference between the two results is smaller than 2 psi (from Figure 3.11), which represents an error percentage less than 0.04%.

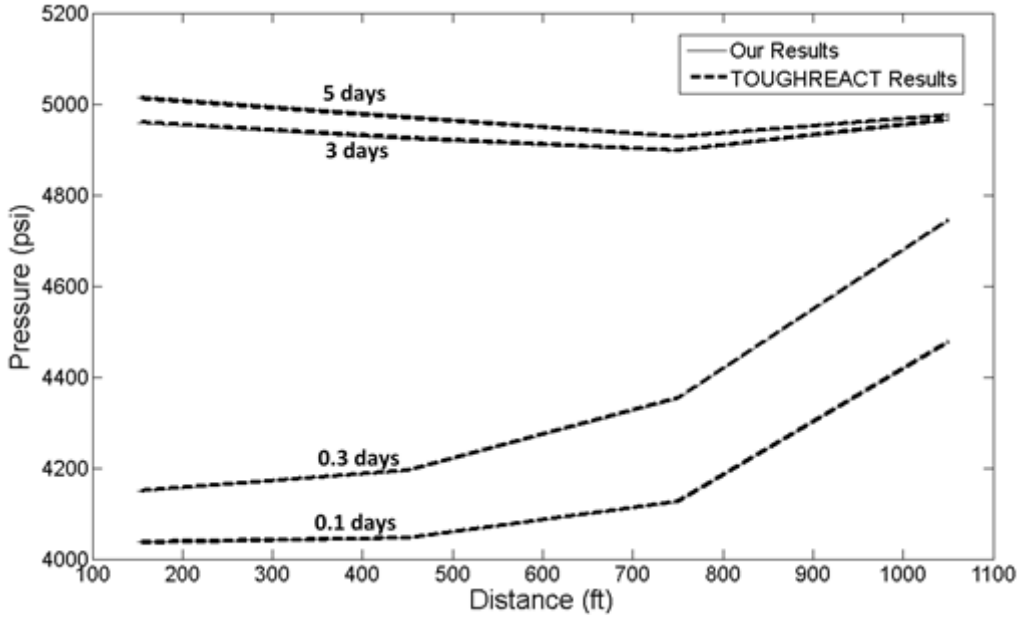

Figure 3.10 Pressure Distributions at Times 0.1, 0.3, 3, and 5 days of TOUGHREACT Against Our Calculations. Solid lines represent our results, while dashed lines represent TOUGHREACT.

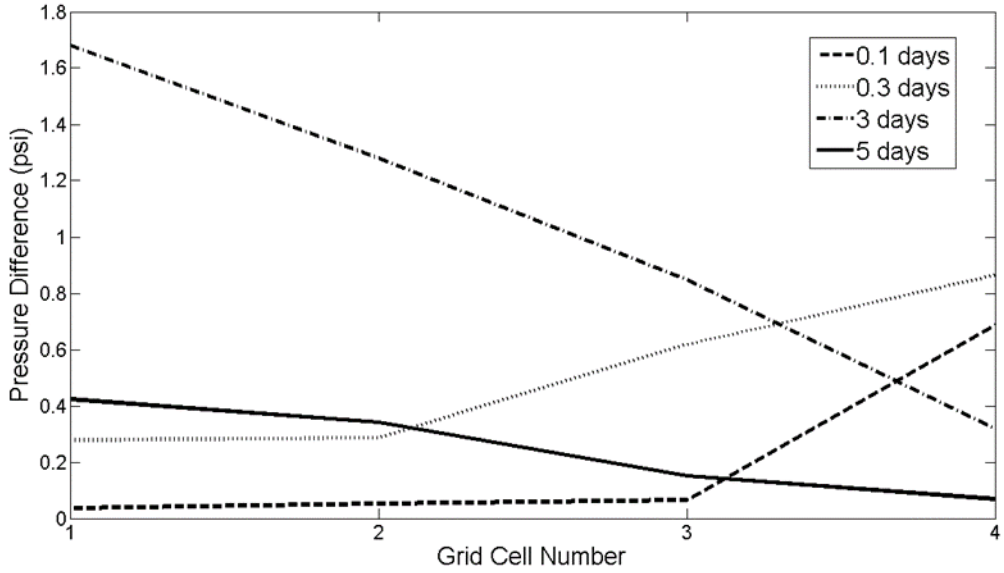

Figure 3.11 Difference Between TOUGHREACT Results and Our Results for Each Grid Cell at Different Times.

3.3.3.2 Testing Advection Problem #2: Heterogeneous Formation

Problem Description:

The second testing problem is water production/injection from/into a heterogeneous aquifer. The west (left) boundary is a constant pressure boundary of 4400 psi, and the east (right) boundary is a no-flux (sealed) boundary. The northern (top) boundary is a constant outflux boundary of 0.075 STB/day/ft^2, while the southern (bottom) boundary is a constant influx boundary of 0.04 STB/day/ft^2. Reservoir length, width, and thickness are 6400, 4800, and 80 ft, respectively. The aquifer has 3 producers and 2 injectors located at (600 ft, 450 ft), (2600 ft, 2550 ft), (5800 ft, 2850 ft), (3800 ft, 1050 ft), (1000 ft, 3150 ft), respectively, away from the south west corner of the aquifer. The production rates for the 3 producers are 650 STB/day, 550 STB/day, and 700 STB/day. The injection rates for the 2 injectors are 700 STB/day and 750 STB/day. Figure 3.12 depicts the boundary conditions described above as well as the locations of the wells. Formation total compressibility is 2.86×10^{-6} psi^{-1}. Formation fluid is water with 0.89 cp viscosity and 1 bbl/STB formation volume factor.

The aquifer is highly heterogeneous with an average porosity of 0.1 and average permeability of 310 md. The porosity and permeability distributions follow a log normal distribution in the ranges [0.0056, 0.97] and [17.4 md, 3000 md], respectively. When the reservoir is discretized to 16*x*16*x*1 grids in the x, y, and z directions respectively, each grid cell is assigned different porosity and permeability value, and the porosity and permeability distributions take the shape shown in Figures 3.13 and 3.14, respectively.

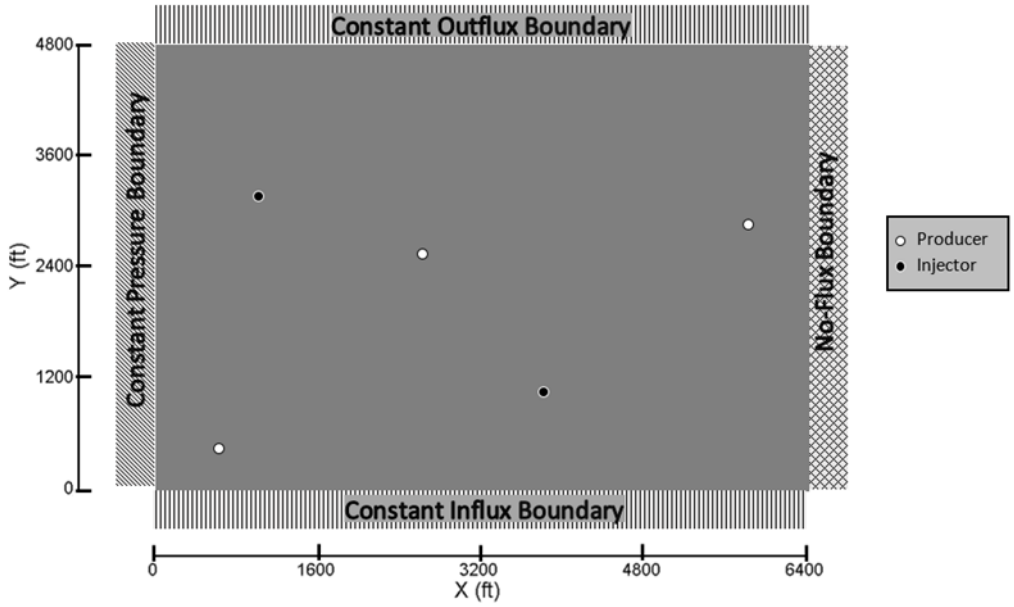

Figure 3.12 2D Schematic of Testing Advection Problem #2. Circles represent well locations.

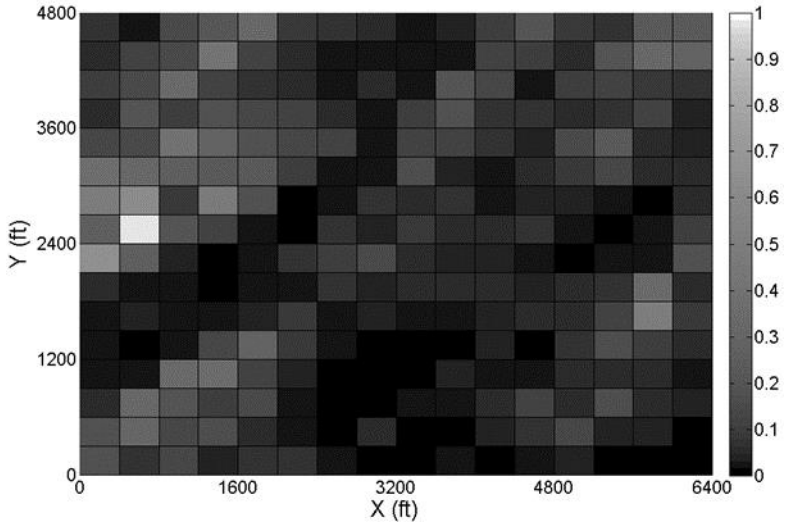

Figure 3.13 Porosity Distribution for Advection Testing Problem #2.

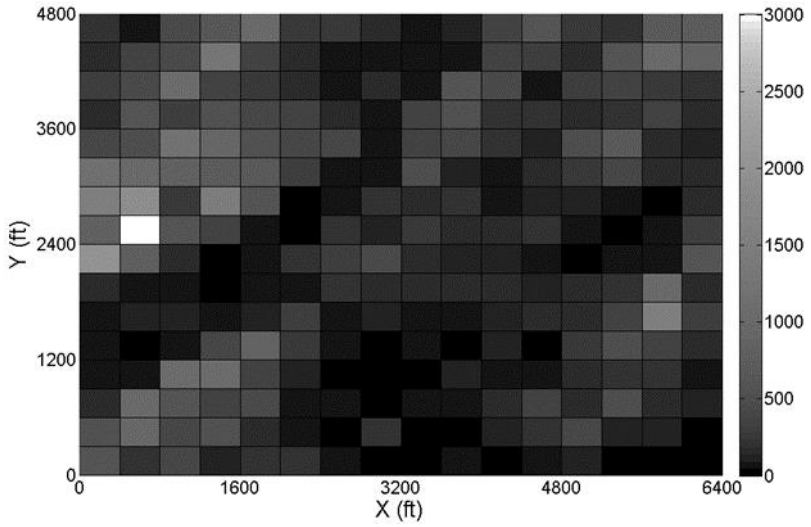

Figure 3.14 Permeability Distribution for Advection Testing Problem #2.

Our Model Description:

The problem described above represents advection of water (slightly compressible fluid) in a heterogeneous porous medium. Thus, it can be modeled using the single-phase pressure transient flow equation of a slightly compressible fluid in a linear two-dimensional reservoir, given by;

$$\frac{\partial}{\partial x}\left(\frac{KA}{\mu B}\frac{\partial p}{\partial x}\right)\Delta x + \frac{\partial}{\partial y}\left(\frac{KA}{\mu B}\frac{\partial p}{\partial y}\right)\Delta y + q_{sc} = \frac{V_b \emptyset C_t}{B}\frac{\partial p}{\partial t}$$

Where p is pressure, K is permeability, A is cross-sectional area, B is formation volume factor, μ is water viscosity, q_{sc} is production rate, V_b is bulk volume, ∅ is porosity, and C_t is formation total compressibility.

The aquifer was modeled with a 2-D Cartesian mesh. The aquifer length is discretized into 16 grid cells, each with a constant spacing (Δx) of 400 ft. The aquifer width is also discretized into 16 grid cells, each with a constant spacing (Δy) of 300 ft. Each gird cell was assigned a different porosity and permeability value as in the porosity and permeability distributions shown in figures 3.13 and 3.14. Figure 3.15(a) shows the discretized 2D mesh. The above equation was solved numerically

using a fully implicit finite difference scheme, yielding a system of linear equations. A script in MATLAB was written to solve the system of linear equations. Permeability was harmonically averaged. Simulation run time is 15 days with a constant time step of 0.025 days.

Model Input in TOUGHREACT:

To simulate the same problem in TOUGHREACT, the exact parameters of the problem described above was input in TOUGHREACT, using the module EOS1. To simulate the constant injection and pressure boundaries of the aquifer, the mesh has to be modified as described in advection problem #1. To simulate the no-flux (sealed) boundary of the aquifer, no modifications had to be made to the mesh, as the no-flux boundary is the only boundary recognized in TOUGHREACT. Figure 3.15 (b) shows the modifications done on the mesh to simulate the special boundaries. To model the heterogeneous nature of the aquifer, the value of permeability and porosity for each grid cell was input in TOUGHREACT as INtial CONditions in INCON block in the input file, according to the porosity and permeability distributions shown in figures 3.13 and 3.14, respectively. Permeability is harmonically averaged, as in our model.

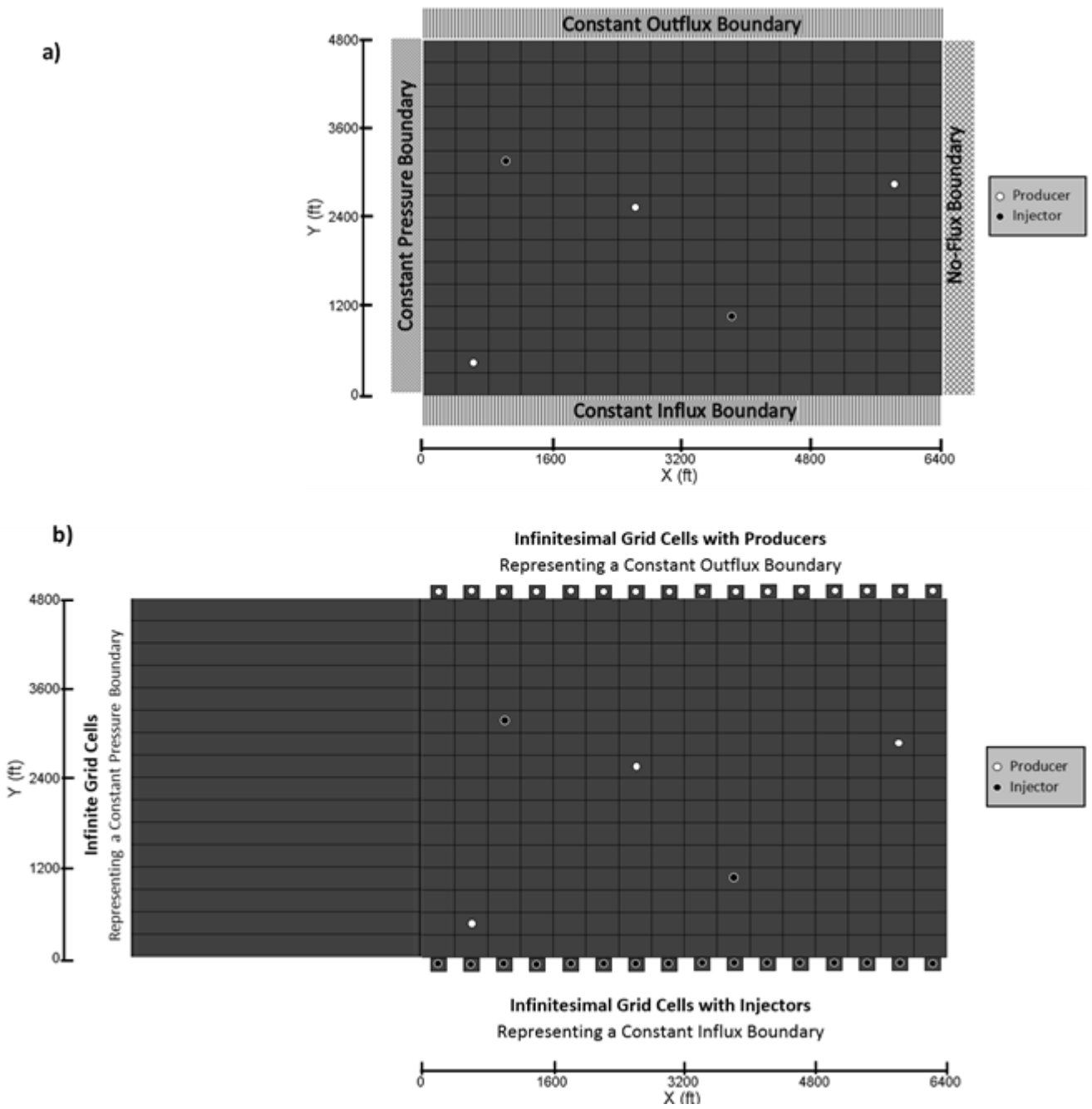

Figure 3.15 Modifications of the Two-Dimensional Cartesian Mesh for Advection Testing Problem #2. Figure 3.15.a shows the main mesh with the special boundary conditions depicted. Figure 3.15.b shows the modifications done to simulate these boundary conditions.

Results Comparison:

Figure 3.16 shows a comparison in the results between the pressure distribution from our results and that of TOUGHREACT.

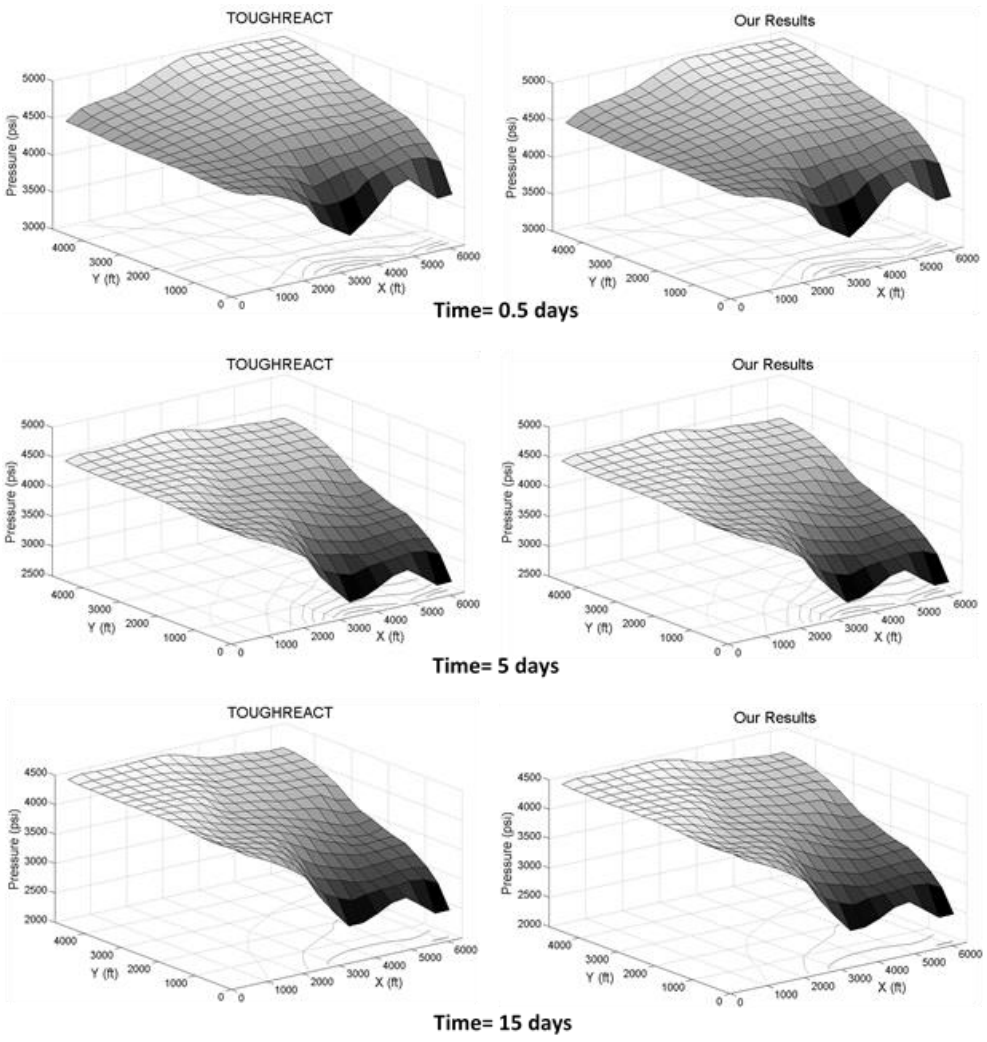

Figure 3.16 Pressure Distributions at Times 0.5, 5, and 15 days of TOUGHREACT Against Our Calculations. Figures on the left represent our results, while figures on the right represent TOUGHREACT.

While the results might seem identical, there is a slight difference in calculated pressures from TOUGHREACT and our results. Figure 3.17 shows the difference in calculated pressure between

TOUGHREACT and our results ($\Delta P = P_{TOUGHREACT} - P_{Our\ Results}$) for each grid block. The maximum absolute difference between the two results is smaller than 3 psi (from Figure 3.17), which represents an error percentage less than 0.06%.

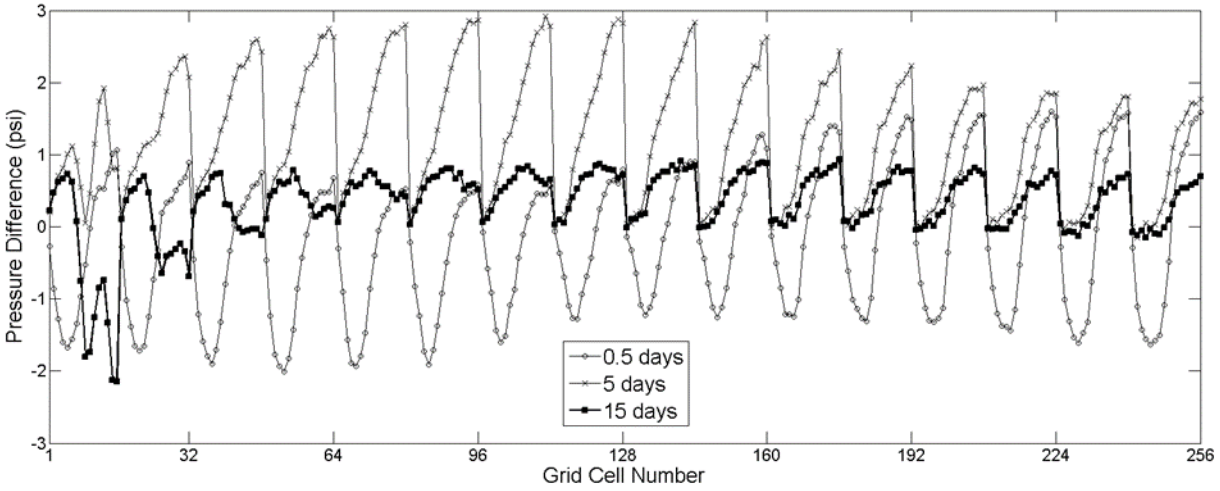

Figure 3.17 Difference Between TOUGHREACT Results and Our Results for Each Grid Cell at Different Times.

3.3.3.3 Results Discussion for Testing Advection Problem #1 and #2

From the comparisons made in Figure 3.11 and Figure 3.17, there is small difference between our results and that of TOUGHREACT. The maximum absolute difference percentage is 0.04% for testing advection problem#1 and 0.06% for testing advection problem#2. This small error might be because, in our calculations, we are using constant water properties (viscosity and density), i.e., water properties are insensitive to pressure changes. In TOUGHREACT, water properties change with changing pressure. TOUGHREACT calculates all water properties from the steam tables created by the International Formulation Committee in 1967. Nevertheless, we can say that there is a good match between our results and that of TOUGHREACT. This shows the ability of TOUGHREACT to simulate advection in both homogenous and heterogeneous formations. More

importantly, this shows that the above described method, for simulating special boundary conditions, is successful.

CHAPTER 4

REACTION ADVECTION DIFFUSION (RAD)

SIMULATIONS

Now as the code is compiled, calibrated, and tested, we can embark on using it in the new proposed application, that is simulation of carbonates acidizing with hydrochloric acid. This simulation will be referred later to as Reaction Advection Diffusion (RAD) Simulation.

4.1. Meshes Used in RAD Simulations

In this work, we are using two meshes in RAD simulations. One 2D mesh and one 3D mesh. Follows is a brief description for each mesh.

4.1.1. Two-Dimensional (2D) Mesh

This mesh is a (50*x*100*x*1) mm domain. The domain is discretized into 50*x*100*x*1 grids in the x, y, and z directions, respectively. This makes a constant grid spacing ($\Delta x=\Delta y=\Delta z$) of 1 mm and a constant grid volume of 1 mm^3. Figure 4.1 shows the mesh described above. The southern (bottom) boundary is exposed to a constant acid injection. The injected acid is uniformly distributed over the southern boundary. The northern (top) boundary is held at a constant back pressure of 1000 psi. These special boundary conditions were input in TOUGHREACT as explained earlier in testing advection problem #1 and #2.

Each gird cell was assigned a different value of porosity and permeability. The porosity of the domain was randomly generated in a fashion that it follows a uniform distribution within the range [0.15, 0.2] with an average (ϕ_{mean}) of 0.175. Figure 4.2 shows the porosity distribution, and Figure 4.3 shows the probability density function of the porosity distribution

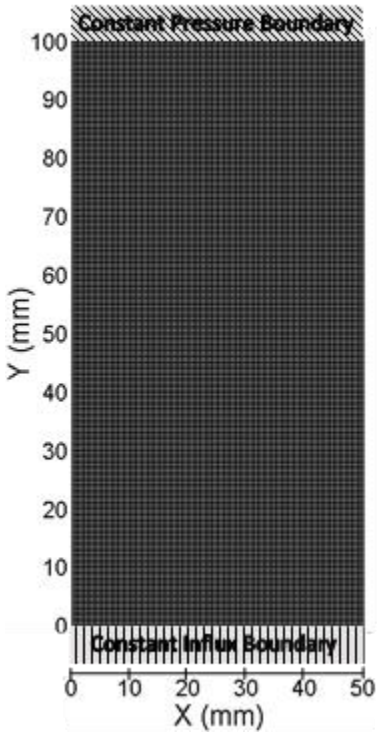

Figure 4.1 Two-Dimensional Mesh for Reaction Advection Diffusion Simulations

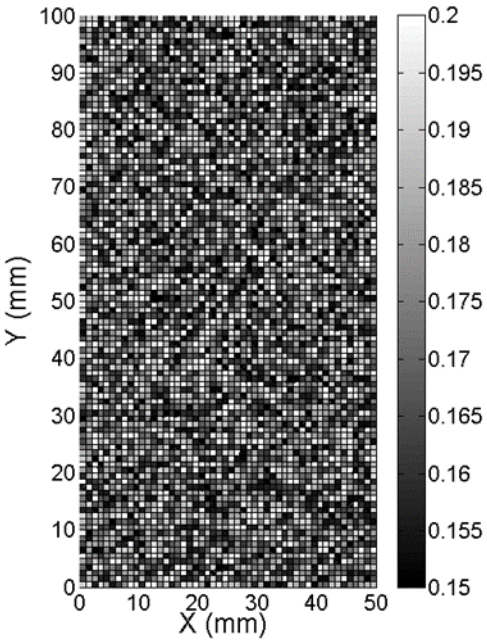

Figure 4.2 Porosity Distribution of the Two-Dimensional Mesh of Reaction Advection Diffusion Simulations

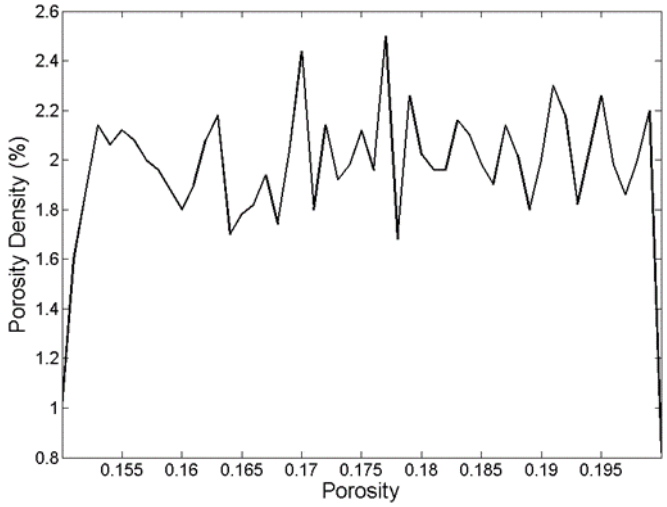

Figure 4.3 Uniform Porosity Probability Density Function of the Two-Dimensional Mesh of Reaction Advection Diffusion Simulations.

The permeability distribution was calculated from the porosity distribution using the Verma-Pruess porosity-permeability relationship with Ki=1.4 md, ϕ_c=0, and n=7.6, given by;

$$k_j = k_i\left(\frac{\phi_j-\phi_c}{\phi_{mean}-\phi_c}\right)^n \qquad \text{for j=1,m.}$$

Where k_j is permeability of grid j, k_i is the initial permeability, ϕ_j is porosity of grid j, ϕ_c is the critical porosity at which permeability goes to zero, ϕ_{mean} is the average initial porosity of the domain, n is an exponent, and m is the total number of grids.

The resulting permeability distribution follows -more or less- a log normal distribution. Figure 4.4 shows the permeability distribution, and Figure 4.5 shows the probability density function of the permeability distribution.

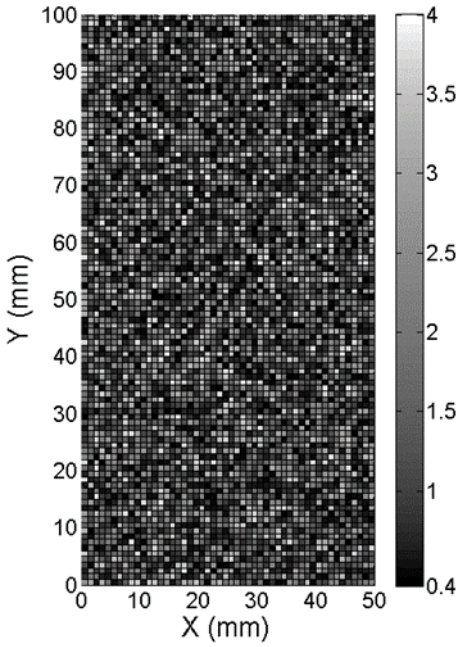

Figure 4.4 Permeability Distribution of the Two-Dimensional Mesh of Reaction Advection Diffusion Simulations

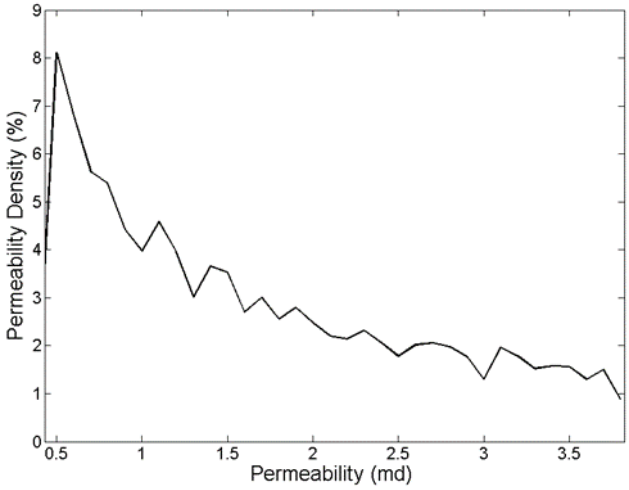

Figure 4.5 Log Normal Permeability Probability Density Function of the Two-Dimensional Mesh of Reaction Advection Diffusion Simulations

4.1.2. Three-Dimensional (3D) Mesh

This mesh is based on the experimental work of Dong & Hill[53]. They used a cylindrical core of 1 inch (25.4 mm) in diameter and 4 inches (101.6 mm) in length. Acid is injected at a constant rate from one face of the cylindrical core, while the other face is subjected to a constant back pressure. The lateral (circumferential) area of the core is sealed. Figure 4.6 shows a schematic of the core used in Dong & Hill[53] experiment.

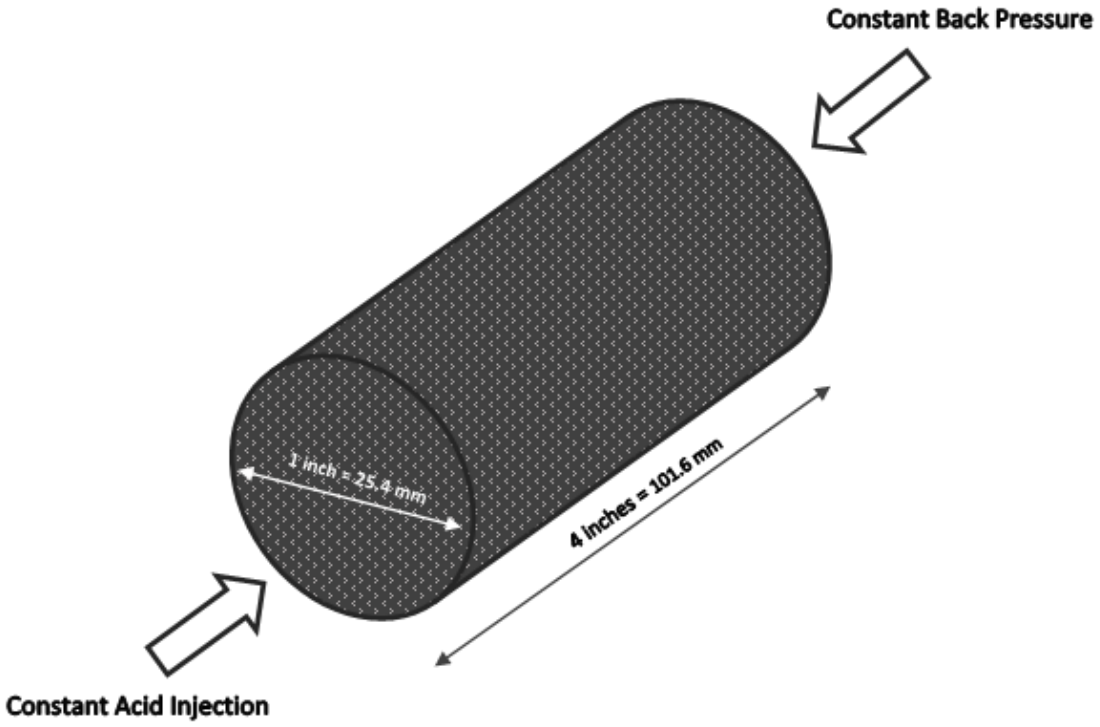

Figure 4.6 Schematic of the 1"x4" Core Used in Dong & Hill Experiment.

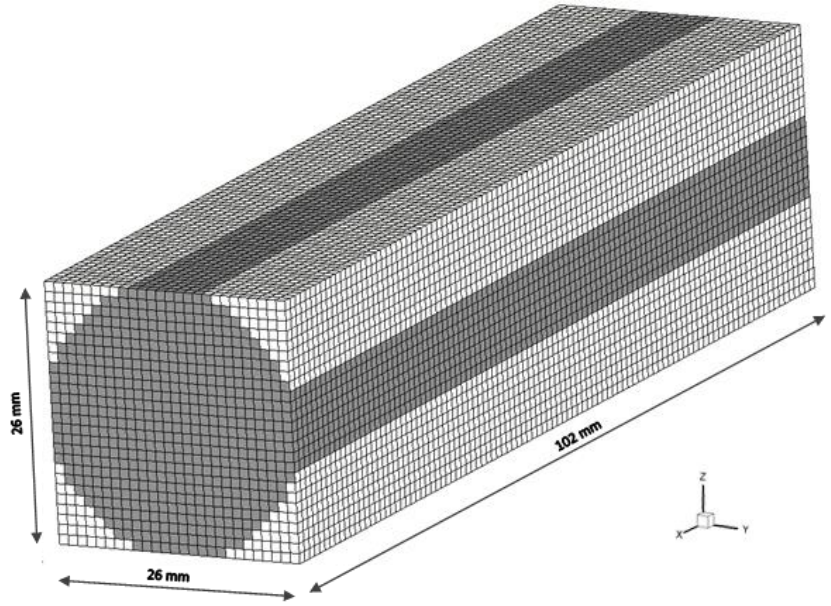

Figure 4.7 Three-Dimensional Mesh for Reaction Advection Diffusion Simulations. Dark grey cells represent the 1"x4" cylindrical core, while white cells represent no-flow cells.

To simulate the cylindrical core into the Cartesian (rectangular) system, the cylindrical core is inscribed in to a cuboid of a comparable length and width to the core diameter and has almost the same length as the core length. While the core has a diameter of 25.4 mm, the cuboid has a length and a width of 26 mm. And while the core has a length of 101.6 mm, the cuboid has a length of 102 mm. The rectangular domain is discretized into 102*x*26*x*26 grids in the x, y, and z directions, respectively. This makes a constant grid spacing ($\Delta x=\Delta y=\Delta z$) of 1 mm and a constant grid volume of 1 mm^3. Figure 4.7 shows the 3D mesh of the 1"*x*4" core inscribed in the rectangular domain. Dark cells represent the cylindrical core, while white cells represent the remainder of the rectangular domain. In this mesh, the dark cells are sealed from the white cells by a no-flow boundary. Thus, flow is only allowed in the dark cells, while the white cells are no-flow cells.

Each gird cell was assigned a different value of porosity and permeability. The porosity of the domain was randomly generated in a fashion that it follows a uniform distribution within the range [0.1, 0.2] with an average (ϕ_{mean}) of 0.15. Figure 4.8 shows the porosity distribution, and Figure 4.9 shows the probability density function of the porosity distribution.

The permeability distribution was calculated from the porosity distribution using the Verma-Pruess porosity-permeability relationship with K_i=5 md, ϕ_c=0, and n=7.6. The resulting permeability distribution follows -more or less- a log normal distribution. Figure 4.10 shows the permeability distribution, and Figure 4.11 shows the probability density function of the permeability distribution.

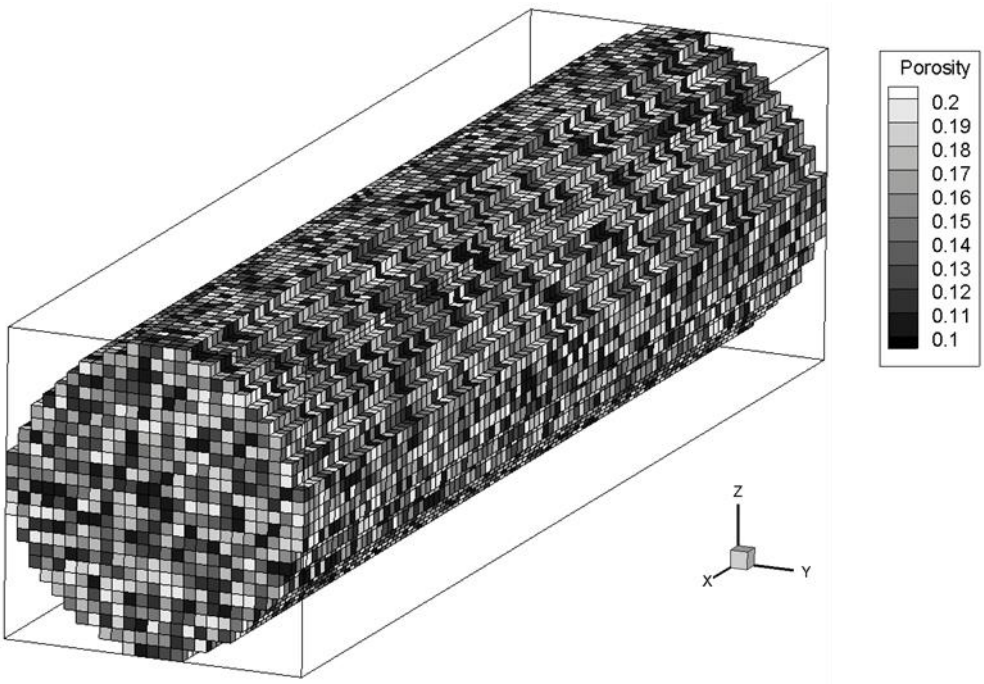

Figure 4.8 Porosity Distribution of the Three-Dimensional Mesh of Reaction Advection Diffusion Simulations.

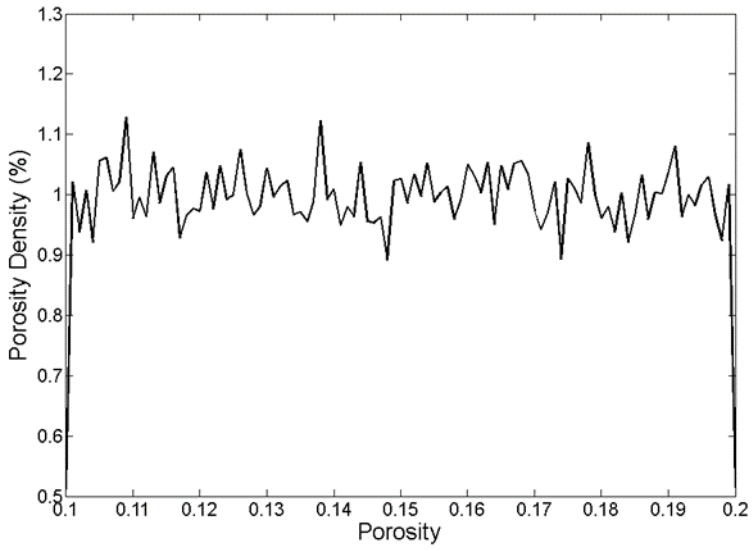

Figure 4.9 Uniform Porosity Probability Density Function of the Three-Dimensional Mesh of Reaction Advection Diffusion Simulations

.

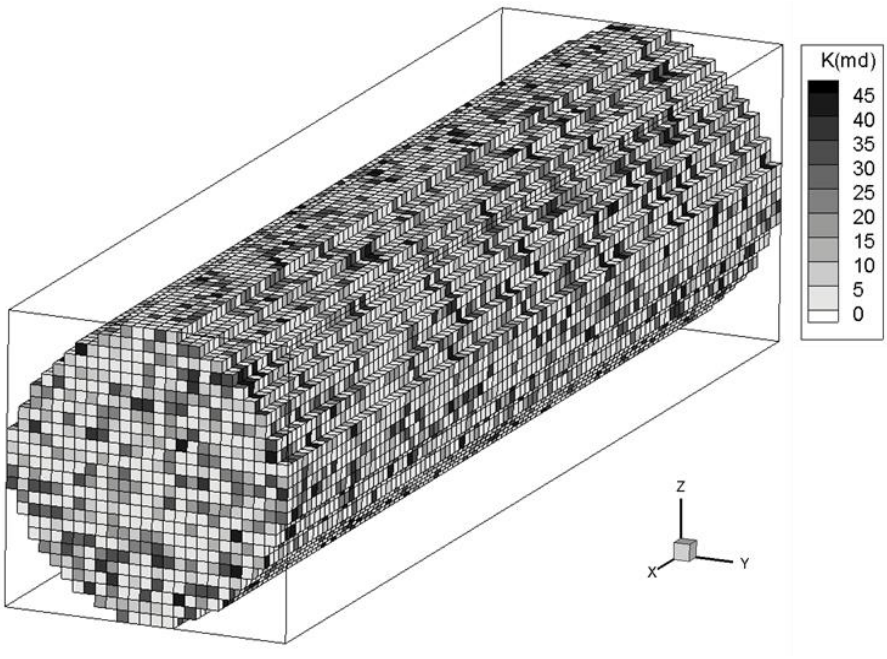

Figure 4.10 Permeability Distribution of the Three-Dimensional Mesh of Reaction Advection Diffusion Simulations

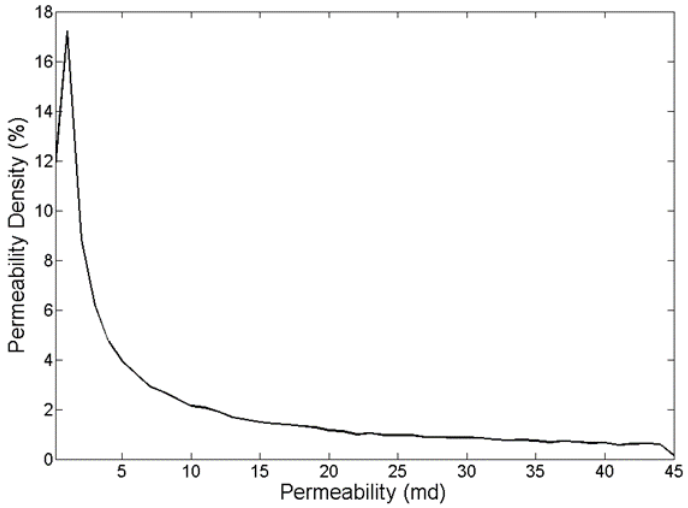

Figure 4.11 Log Normal Permeability Probability Density Function of the Two-Dimensional Mesh of Reaction Advection Diffusion Simulations

The acid injection face of the core was modeled as a constant injection boundary, while the core face exposed to a constant back pressure was modeled as a constant pressure boundary. The constant injection and constant pressure boundaries were input in TOUGHREACT as explained earlier in testing advection problem #1 and #2. The sealed lateral (circumferential) area of the core was modeled as a no-flux boundary. At the core face were the acid is injected, the acid is not uniformly distributed throughout the entire core face. The acid is injected via an inlet that has a concentric nozzle. The nozzle is connected to two concentric circular troughs. Figure 4.12(a) shows a picture of the acid inlet used in experiments. To model the acid distribution as close as possible to that of the experiment, the acid is injected only into two concentric circles. Figure 4.12(b) shows the locations of the injectors. The total acid injection rate is distributed evenly among these injectors.

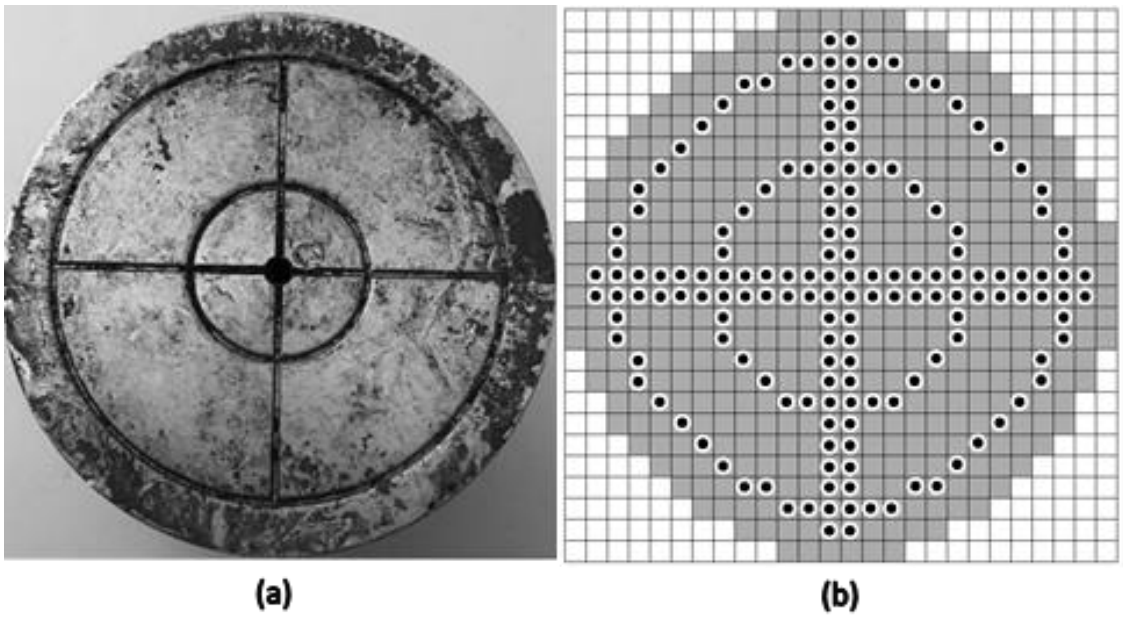

Figure 4.12 Acid Inlet in Experiments (left) and Our Simulations (Right). Figure (a) shows a picture of an experimental acid inlet. Figure (b) shows how the inlet is modeled in our simulations, where circles represent acid injectors.

4.2. Definition of the Chemical System

4.2.1. Choice of the System Species

In this work, the only mineral reaction we have is the reaction of calcite mineral ($CaCO_3$) with hydrogen ions (H^+). This reaction yields calcium and bicarbonate ions. However, this is not the only reaction occurring in the entire system. There are other reactions occurring between the solution ions/species. These reactions, known as aqueous kinetics, along with the single mineral reaction are listed in Table 4.1.

Table 4.1 List of Chemical Reactions in the HCl/Calcite System

Chemical Reaction Type	Chemical Reaction Equation
Heterogeneous (mineral/acid) reaction	$CaCO_3 + H^+ \rightarrow Ca^{+2} + HCO_3^-$
Homogeneous (aqueous) reactions	1. $H^+ + OH^- \rightarrow H_2O$ 2. $HCl_{(aq)} \rightarrow H^+ + Cl^-$ 3. $CO_{2(aq)} + H_2O \rightarrow H^+ + HCO3^-$ 4. $H^+ + CO_3^{-2} \rightarrow HCO_3^-$ 5. $H^+ + CaCO_{3\,(aq)} \rightarrow Ca^{+2} + HCO_3^-$ 6. $CaHCO_3^+ \rightarrow Ca^{+2} + HCO_3^-$ 7. $CaOH^+ + H^+ \rightarrow Ca^{+2} + H_2O$ 8. $CaCl^+ \rightarrow Ca^{+2} + Cl^-$ 9. $CaCl_2 \rightarrow Ca^{+2} + 2Cl^-$

Based on the reactions defined in Table 4.1, we have 14 different species, namely;

1. H_2O
2. H^+
3. Ca^{+2}
4. HCO_3^-
5. Cl^-
6. OH^-
7. $HCl_{(aq)}$
8. $CO_{2(aq)}$
9. CO_3^{-2}
10. $CaCO_{3(aq)}$
11. $CaHCO_3^+$
12. $CaOH^+$
13. $CaCl^+$
14. $CaCl_{2(aq)}$

To reduce the computational cost of the problem, we need to solve the mass conservation equations for the minimum number of species. Thus, the above listed species are divided into primary species and secondary species, as adopted by Morel & Hering[54]. TOUGHREACT, as well as many other reactive transport codes, solves the mass conservation equations for the primary species only. Primary species concentrations are independent of other species concentrations. Primary species can be thought of as the building blocks of chemical systems, as all reactions involving minerals, gases, and secondary species are written as a function of the primary species only. Secondary species are all the other species that are not primary species. Secondary species are derived from primary species, as the secondary species concentrations depend on the concentrations of primary species through the reaction equilibrium constant (law of mass action). Table 4.2 shows the classification of the 14 species of the system into primary and secondary species, along with the chemical equations governing the derivation of secondary species from the primary species. The

primary species are defined so that their number is the minimum, and that all other species (secondary species) can be written in terms of the primary species.

Table 4.2 List of Primary and Secondary in the HCl/Calcite System

Primary Species	Secondary Species
1. H_2O 2. H^+ 3. Ca^{+2} 4. HCO_3^- 5. Cl-	1. OH^- *Equation:* $H^+ + OH^- \rightarrow H_2O$ 2. $HCl_{(aq)}$ *Equation:* $HCl_{(aq)} \rightarrow H^+ + Cl^-$ 3. $CO_{2(aq)}$ *Equation:* $CO_{2(aq)} + H_2O \rightarrow H^+ + HCO_3^-$ 4. CO_3^{-2} *Equation:* $H^+ + CO_3^{-2} \rightarrow HCO_3^-$ 5. $CaCO_{3(aq)}$ *Equation:* $H^+ + CaCO_{3\,(aq)} \rightarrow Ca^{+2} + HCO_3^-$ *6.* $CaHCO_3^+$ *Equation:* $CaHCO_3^+ \rightarrow Ca^{+2} + HCO_3^-$ *7.* $CaOH^+$ *Equation:* $CaOH^+ + H^+ \rightarrow Ca^{+2} + H_2O$ *8.* $CaCl^+$ *Equation:* $CaCl^+ \rightarrow Ca^{+2} + Cl^-$ *9.* $CaCl_{2(aq)}$ *Equation:* $CaCl_2 \rightarrow Ca^{+2} + 2Cl^-$

4.2.2. Choice of the Thermodynamic Database

As mentioned earlier, the concentrations of the secondary species are calculated based on the concentrations of the primary species from the reaction equilibrium constants, as stated by the law of mass action. This entails that we need to define the equilibrium constant for each reaction in our system, whether a homogenous or a heterogeneous reaction. A thermodynamic database is a library

that contains the equilibrium constants for all the reactions defined in the system at different temperatures. These libraries compile the equilibrium constants from different experimental work found in the literature. To choose a thermodynamic database for our work, we compare between the following databases compiled by two different research institutes;

LBNL#1: Compiled by Lawrence Berkley National Laboratory (LBNL) after database of EQ3/6 geochemical modeling code[55]. This database was used before for CO_2 sequestration problems.

LBNL#2: Compiled by Lawrence Berkley National Laboratory (LBNL) after EQ3/6 SUPCRT92 database[56]. This database was used before for formation damage prediction due to water injection problems.

LBNL#3: Compiled by Lawrence Berkley National Laboratory (LBNL) after EQ3/6 geochemical modeling code[55] with modifications. This database was used before for CO_2 sequestration problems.

BRGM#1: Compiled by the French geological survey "Bureau de Recherches Géologiques et Minières" (BRGM), after Thermoddem database[57]**.** This database was used before for CO_2 sequestration problems.

BRGM#2: Compiled by the French geological survey "Bureau de Recherches Géologiques et Minières" (BRGM), after Thermoddem database[57] with modifications, available on their website[58].

The comparison is made in the values of equilibrium constants (k) of the reactions listed in table 4.1. Figure 4.13 and appendix C show a comparison in the variation of the logarithm of equilibrium constant (log(k)) with changing temperature for the reactions of calcite mineral, hydroxide ion

(OH^-), aqueous hydrogen chloride $HCl_{(aq)}$, aqueous carbon dioxide $CO_{2(aq)}$, carbonate ion (CO_3^{-2}), aqueous calcium carbonate ($CaCO_{3(aq)}$), calcium bicarbonate ion ($CaHCO_3^+$), calcium hydroxide ion ($CaOH^+$), calcium chloride ion ($CaCl^+$), and aqueous calcium chloride ($CaCl_{2(aq)}$), respectively. Shown below is the comparison for the heterogeneous reaction of the calcite mineral, the remainder of the comparisons for the aqueous (homogeneous) reactions are shown in appendix C.

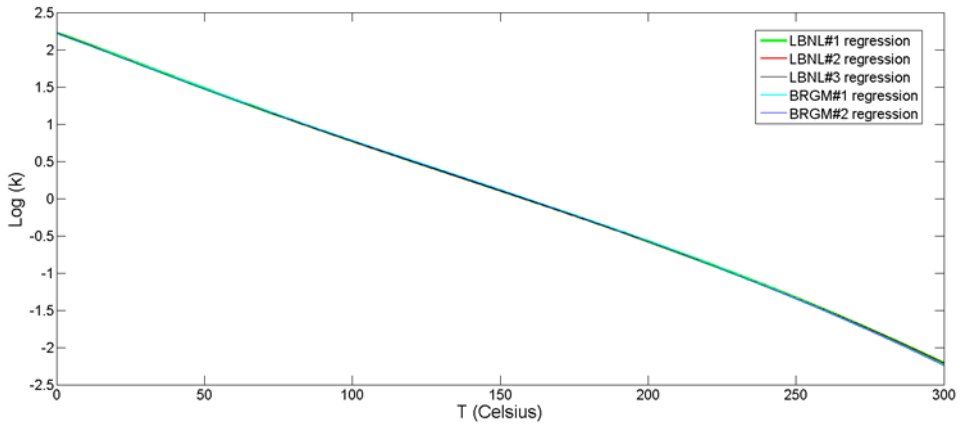

Figure 4.13 Comparison in Reported Equilibrium Constant Variation with Temperature for Calcite Mineral Reaction from Different Thermodynamic Databases

From the comparison in the Figure 4.13 and appendix C, there is almost identical log K values for all species reactions except for calcium chloride ion ($CaCl^+$), aqueous hydrogen chloride ($HCl_{(aq)}$), aqueous calcium carbonate ($CaCO_{3(aq)}$), calcium bicarbonate ion ($CaHCO_3^+$), and calcium hydroxide ion ($CaOH^+$). In this work, we will be using the thermodynamic database BRGM#2, being the most up to date database of all databases compared between.

4.3. Model Initialization

Initialization is the process of defining the initial conditions (pressure, temperature, and concentration) of the simulation domain.

4.3.1. Pressure Initialization

In acid core flooding experiments, a common practice is to inject a non-reactive fluid into the core prior to acid injection. The non-reactive fluid, usually de-ionized water or KCl-saturated water, is injected into the core till steady state is achieved. After steady state is achieved, the non-reactive fluid injection ceases and the acid injection starts.

In our simulations, we follow the same steps of the experiments. We start by injecting de-ionized water till steady state is achieved. Steady state is indicated by the pressure distribution no longer changing with time. These non-reactive runs will be referred to later as steady state runs. The initial pressure of the steady state runs is set equal to the back pressure of 1000 psi. The final pressure distribution of the steady sate runs is used as the initial pressure distribution for the reactive runs, in which acid is injected.

Figure 4.14 shows the evolution of pressure distribution in the 2D mesh, at times 0, 1, 60, 120, and 300 seconds. Since the pressure distribution doesn’t change after 60 seconds, this indicates that the steady state condition is achieved. In all of the reactive runs, the pressure distribution at steady state conditions is used as the initial pressure distribution for reactive runs.

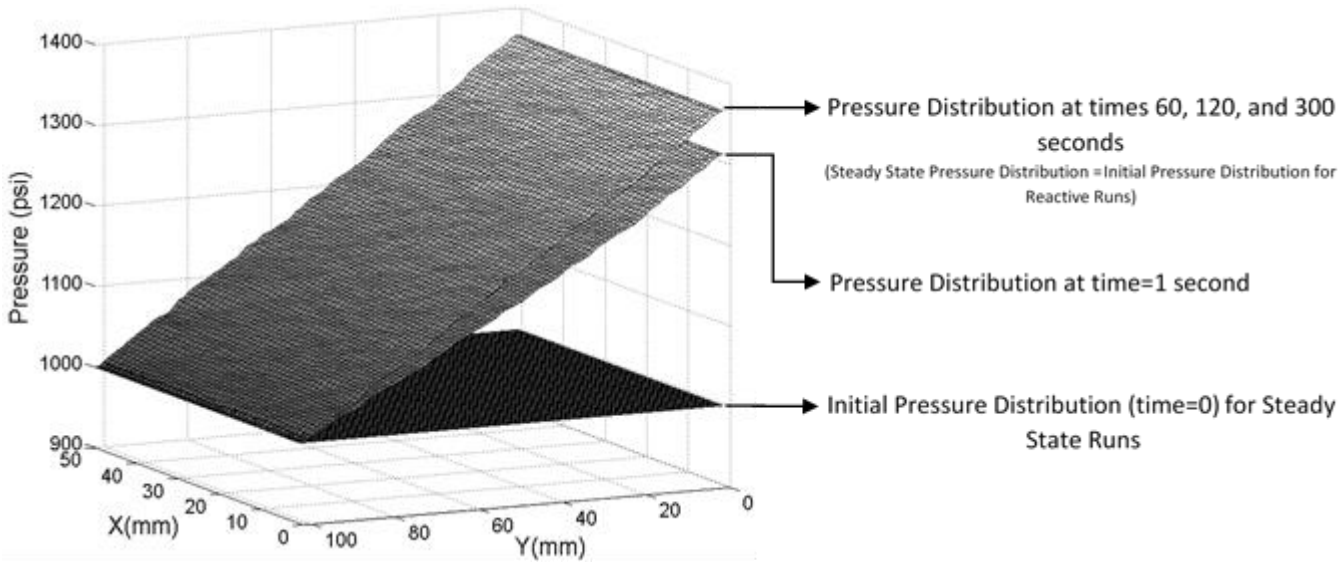

Figure 4.14 Pressure Distributions for the Steady State Runs in the 2D Mesh for an injection rate of 0.1 cc/min at times 0, 1, 60, 120, and 300 seconds.

4.3.2. Temperature Initialization

As for the temperature, the initial temperature distribution is assumed even throughout the entire simulation domain. The temperature is 25^{o}C for the 2D domain and 22^{o}C for the 3D domain. The reactive simulations are assumed isothermal, thus the domain temperature doesn't change with time.

4.3.3. Concentrations Initialization (Initial Speciation Calculations)

Initial speciation calculations are batch (zero-dimensional and equilibrium-based) calculations done to estimate the concentration of each species in the system at equilibrium. These calculations are done for each water type. In this work, there are two types of waters;

1. Initial water: This is the water that initially saturates the domain. In our case, the domain is composed of pure limestone (100% calcite mineral) and is saturated with de-ionized water (pH=7). The water is assumed in equilibrium with calcite.

2. Injection water: This is the water introduced to the domain. In our case, this is 15% (weight percentage) hydrochloric acid. This acid concentration is equal to 4.84 molal (moles of HCl/ kg of water) or 4.42 molar (moles of HCl/liter of water).

In each of the above defined waters, knowing the total concentrations of all primary species, it is required to estimate the concentrations of all species at equilibrium. This is done by the initial speciation calculations. The species concentration at equilibrium is used as the initial concentration in our simulations.

In this work, the initial speciation calculations are made using Aqion; an open-source hydrochemistry software tool, that utilizes PhreeqC as an internal numerical solver. PhreeqC (PH REdox EQuilibrium in C language) is an open-source geochemistry software developed by the United States Geological Survey (USGS) that is based on the work of Parkhurst[59]. The software is used for speciation calculations, batch reaction simulations, and one-dimensional transport simulations.

Tables 4.3 and 4.4 show the total and equilibrium concentrations for initial and Injection waters respectively. As mentioned earlier, the equilibrium concentrations are used as the initial concentrations in our simulations. The concentrations of secondary species are calculated internally in TOUGHREACT, using the equilibrium constants provided in the thermodynamic database.

Table 4.3 Total and Equilibrium Concentrations of Primary Species for Initial Water

Primary Species	Total Concentration (molal)	Equilibrium Concentration (molal)
H^+	1.003839E-07	1.261889E-10
Ca^{+2}	1.230651E-04	1.172382E-04
HCO_3^-	1.230651E-04	8.339955E-05
Cl^-	0.276300E-12	0.276300E-12

Table 4.4 Total and Equilibrium Concentrations of Primary Species for Injection Water

Primary Species	Total Concentration (molal)	Equilibrium Concentration (molal)
H^+	0.484000E+01	0.304000E+01
Ca^{+2}	0.276300E-12	0.276300E-12
HCO_3^-	1.470363E-05	2.274642E-06
Cl^-	0.484000E+01	0.304000E+01

4.4. Model Input Parameters

4.4.1. Acid Density

In all of our simulations, 15 wt% HCl acid was used as an injection water. It is required to know the acid density to convert the acid volumetric injection rate into mass injection rate at each simulation temperature. In our 2D simulations, we are using a temperature of 25ºC and in our 3D simulations we are using a temperature of 22ºC. Figures 4.15 and 4.16 show the HCl acid density at different acid concentrations for 22 and 25 ºC after Perry's Chemical Engineers Handbook[60]. In our simulations, we use the values of acid density reported in these figures.

4.4.2. Acid Diffusion Coefficient

The acid diffusion coefficient was calculated as a function of temperature by the following empirical correlation (after Conway[61]);

$$D = \exp\left(-\frac{2918.54}{T} + 0.0452[H] - 4.995\right)$$

Where D is the diffusion coefficient in m^2/s, T is the temperature in degree Celsius, and [H] is the concentration of hydrogen ions in molar (moles/liter).

Figure 4.17 shows the variation of acid diffusion coefficient with temperature. In our simulations, we use the values of acid diffusion coefficient reported in this figure.

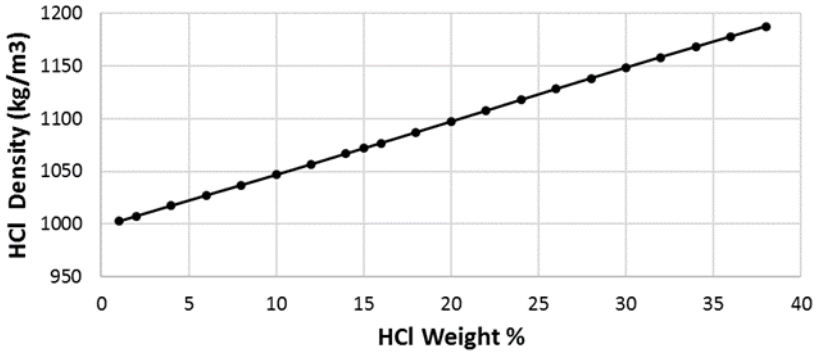

Figure 4.15 HCl Density at 22 ºC for Different Concentrations

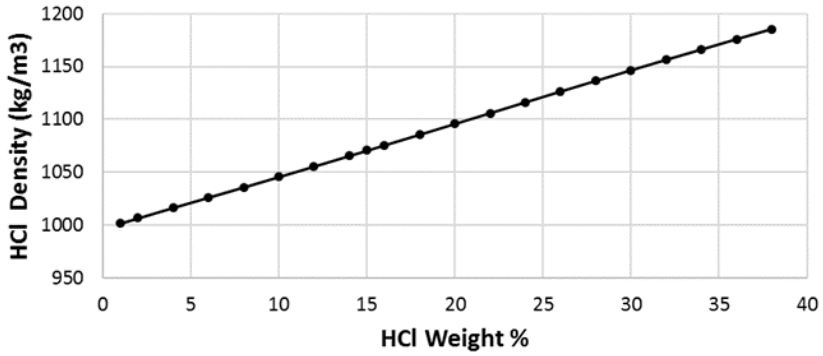

Figure 4.16 HCl Density at 25 ºC for Different Concentrations

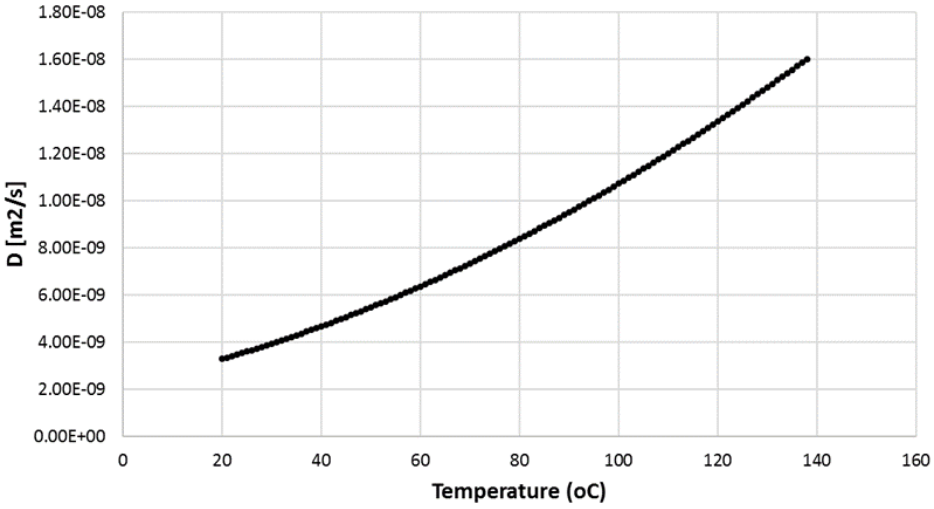

Figure 4.17 Diffusion Coefficient Variation with Temperature

4.4.3. Reaction Rate Constant

In this work, all reactions (listed in table 4.1) are assumed at equilibrium, with the exception of the acid/mineral reaction which is kinetically constrained. It follows that we need to define a reaction rate constant for the acid/mineral reaction. The reaction rate constant was calculated as a function of acid concentration and temperature by the following correlation (after Schecter[62]);

$$K = 7.314 \times 10^{10} \times C_{HCl}^{n} \times exp\left(-\frac{\Delta E}{RT}\right)$$

Where K is the reaction rate constant in moles/m^2.second, C_{Hcl} is the acid concentration in molar (moles/liter), n is the reaction order (=0.63, after Lund[63]), ΔE is the activation energy (=62.76 KJ/mole, after Lund[63]), R is the universal gas constant (=8.314 J/mole.K), and T is the temperature in Kelvin.

Figure 4.18 shows the variation of reaction rate constant with temperature. In our simulations, unless otherwise is stated, we use the values of reaction rate constant reported in this figure.

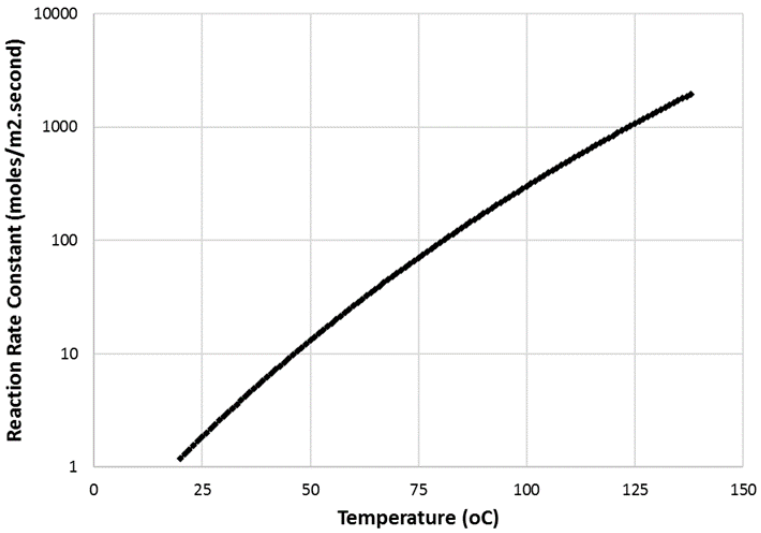

Figure 4.18 Reaction Rate Constant Variation with Temperature

4.4.4. Other Input Parameters

The remainder of the input parameters are constants that are independent of simulation temperature and/or acid concentration. Table 4.5 lists these input parameters.

Table 4.5 Input Parameters for Reactive Simulations

Reactive Surface Area (cm^2/gram)	18.45 (=50 cm^2/cm^3)
Tortuosity Factor for Binary Diffusion	1.0
Pore Compressibility (Pascal-1)	4.5e-10
Rock Grain Density (kg/m^3)	2710
Activation Energy (KJ/mole)	62.76
Porosity-Permeability Relationship	Verma-Pruess Relationship; $k_j = k_i(\frac{\phi_j - \phi_c}{\phi_{mean} - \phi_c})^n$
ϕ_c parameter in Verma-Pruess Relationship	0.0
n exponent in Verma-Pruess Relationship	7.6
Calcite Volume Fraction	1.0
Calcite Molar Volume (cm3/mole)	36.93
Back Pressure (Pressure of the Constant Pressure Boundary) (psi)	1000

4.5. Time Step Information and Breakthrough Criterion

Initially the time step size is very small (0.00001 second), then the time step size changes based on the status of the convergence criteria. If the convergence criterion is not met within 8 iterations for transport calculations and/or 300 iterations for chemistry calculations, time step is reduced by a factor of 4 until convergence occurs. If the convergence criterion is met within five iterations or less for transport calculations, the time step is increased by a factor of 2 (i.e., doubled). The convergence criterion for relative error of transport calculations is 1E-5, while the convergence criterion (as relative change of aqueous concentrations) of chemistry calculations is 1E-6. A sequential non-iterative approach (SNIA) is used where transport and chemistry are sequentially solved without iteration. Xu[52] showed that the difference in the sequential non-iterative approach (SNIA) and the sequential iterative approach (SIA) is small if the courant number ($C= v\Delta t/\Delta x$) is smaller than unity. This condition ($C<1$) is enforced during our simulations. Thus, time step can also be reduced to maintain a courant number below unity. From our simulations, a time step size of 0.01 second was found to be the size that fits all of the above mentioned convergence criteria and Courant condition. Table 4.6 summarizes the limiting conditions and convergence criteria used in our simulations.

Table 4.6 Convergence Criteria for RAD Simulations

Transport Convergence criterion for relative error	1.E-5
Maximum number of transport iterations per time step	8
Chemistry convergence criterion for relative change of aqueous concentrations	0.100E-05
Maximum number of iterations allowed for solving chemical speciation	300
Number of sub-iterations between calculation of activity coefficients and secondary species concentrations at the beginning of each chemical Newton-Raphson iteration.	2
Number of sequential iterations between transport and chemistry	0, a sequential non-iterative approach is used where transport and chemistry are sequentially solved without iteration.
Courant Number (C) Upper Limit	0.5

The simulation continues until the acid breaks through the simulation domain. Breakthrough is the experimental term coined to describe the acid reaching the far end of the core when injected from the other end. In experiments, acid breakthrough is indicated by a negligible pressure drop across the core. In our simulations, we use the same breakthrough criterion of a negligible pressure drop across the simulation domain. This is done by calculating the pressure difference between the arithmetic average of the injectors pressures and the back pressure of the constant pressure boundary, as follows;

$$\Delta P = \frac{\sum_{j=1}^{n} P_j}{n} - P_{back}$$

Where ΔP is the pressure differential across the simulation domain, P_j is the pressure of the injector j, n is the total number of injectors, and P_{back} is the back pressure.

Initially this pressure differential is high, then decreases gradually till it flattens out at almost zero. The time at which pressure differential reaches almost zero is the breakthrough time (t_{BT}). Figure 4.19 shows a typical pressure differential decline curve, with time of breakthrough depicted.

Once t_{BT} is known, it is used to calculate the Pore Volumes of acid injected to achieve Break Through (PVBT), as follows;

$$PVBT = \frac{Total\ Volume\ of\ Acid\ Injected}{Inital\ Pore\ Volume\ of\ the\ Domain} = \frac{q_{inj}\ x\ t_{BT}}{\emptyset_i\ x\ Bulk\ Volume\ of\ the\ Domain}$$

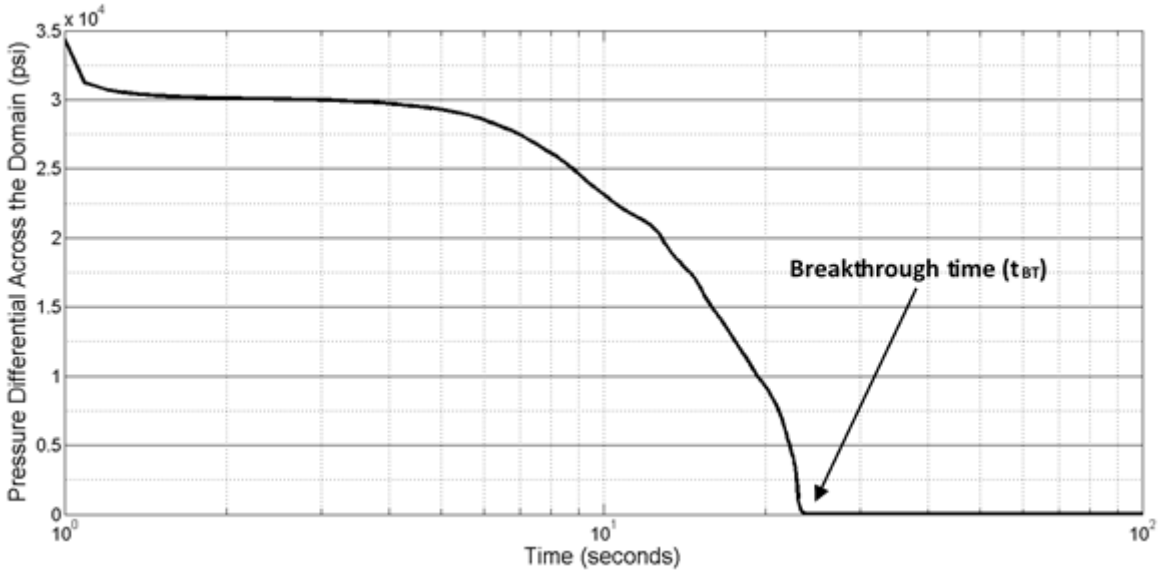

Figure 4.19 A typical Pressure Decline Curve from Acid Injection in the 2D Mesh at a rate of 10 cc/min

CHAPTER 5

RESULTS & DISCUSSION

5.1. Two-Dimensional (2D) Simulations Results

5.1.1. Dissolution Patterns

Dissolution patterns are the shapes of porosity distributions after acid penetration into the core. These patterns result from the acid dissolving the core matrix. Figure 5.1(a) shows the resulting porosity distributions (dissolution patterns) after acid injection for different injection rates. The distributions are arranged from left to right with increasing injection rate. It is observed that with increasing acid injection rate, there are five different dissolution patterns. These patterns are:

1. Face Dissolution Pattern:

This pattern occurs at very low injection rates, where only the face or front of the simulation domain is dissolved, while the remainder of the simulation domain remains intact. Because of the low injection rate, the acid is unable to penetrate into the pore space, and it is completely spent on the domain inlet face. More importantly, the dissolution is stable, meaning that no preferential flow paths (wormholes) are created for the acid to flow into. At the low injection rate, the role of advection in acid transport is negligible and the main mechanism for acid transport is diffusion. Also at these low rates, the rock/acid chemical reaction is fast compared to the acid transport, resulting in high Damkholer number. Because the characteristic time for acid transport is very large compared to the time of rock/acid reaction, the dissolution is mass-transport limited, meaning

that the acid transport is the limiting mechanism for further rock dissolution. This dissolution pattern requires very large volumes of acid to achieve breakthrough. The amount of acid required to achieve breakthrough approaches the asymptotic limit that is equal to the amount of acid required to completely dissolve of the rock, as calculated from the acid dissolving power. The large amounts of acid that this pattern consumes, makes this pattern uneconomical for matrix acidizing treatments.

2. Conical Wormhole Dissolution Pattern:

This pattern occurs at a slightly higher injection rate than that of face dissolution pattern. The higher injection rate allows the acid to penetrate further in the pore space creating a wormhole and dissolution insatiability ensues. However, the rate is not high enough for the acid to reach the tip of the wormhole easily. So, instead of the acid dissolving the wormhole tip and creating longer wormhole, it erodes (dissolves) the walls of the created wormhole. This makes the wormhole has large diameter at the inlet, while having smaller diameter at the tip, resulting in a cone-shaped wormhole. At this slightly higher injection rate, the role of advection in acid transport comes into play, however acid transport by diffusion is still the dominant transport mechanism. As the injection rate is slightly increased, the Damkholer number of this dissolution pattern slightly decreased. However, the characteristic time for acid transport is still larger compared to the time of rock/acid reaction, hence, the dissolution is still mass-transport limited. The amount of acid required to achieve breakthrough in this dissolution patterns is smaller than that of face dissolution.

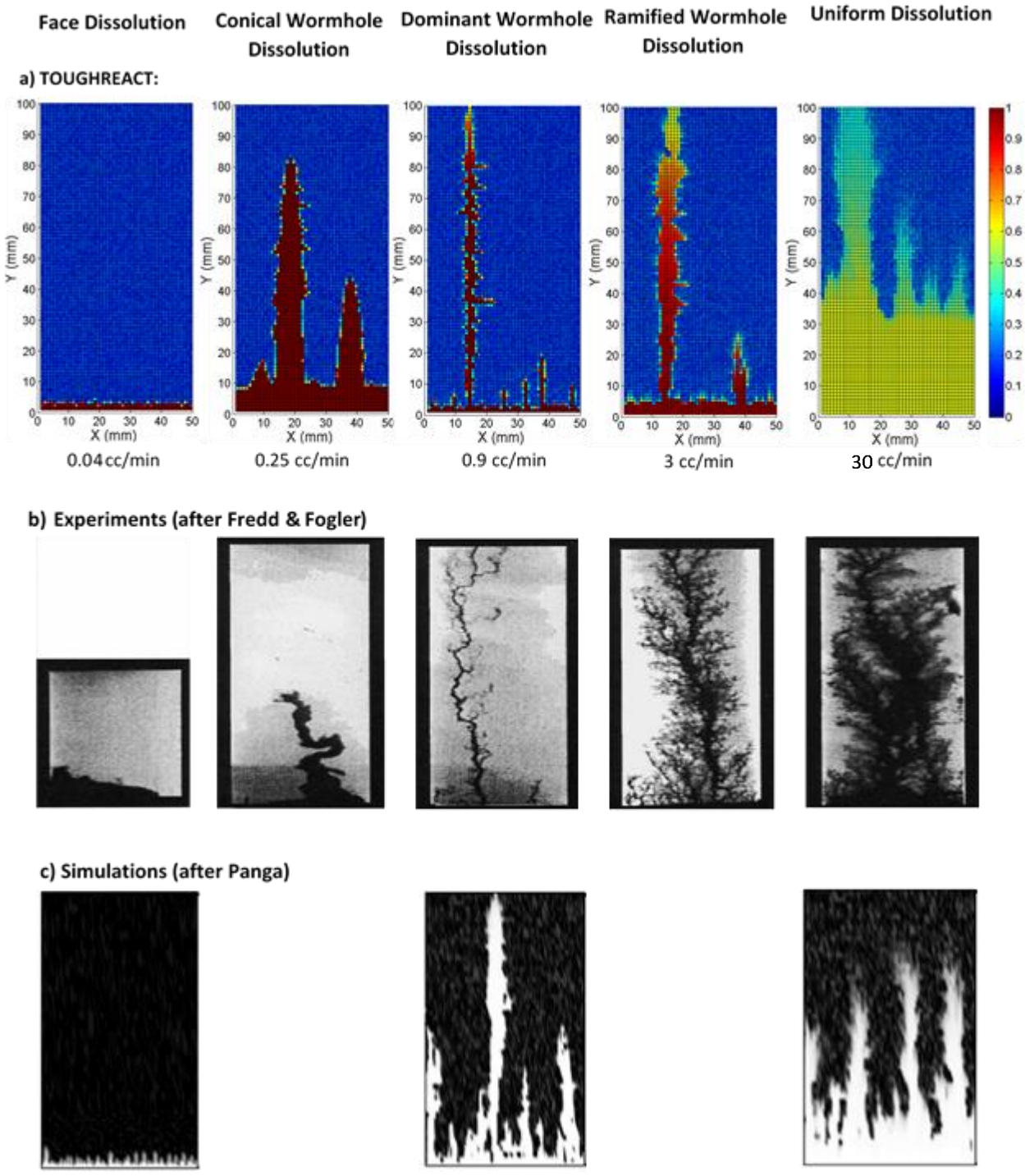

Figure 5.1 Comparison Between Dissolution Patterns from Our Results (fig a), Experimental Work (fig b), and Previous Numerical Simulations (fig c). All figures are arranged from left to right with increasing injection rate.

3. Dominant Wormhole Dissolution Pattern:

This pattern occurs at a higher injection rate than that of conical wormhole dissolution pattern. The higher injection rate not only allows the acid to penetrate further in the pore space creating a wormhole, but also allows the acid to reach the tip of the wormhole. This favors further rock dissolution at the tip of the wormhole, creating longer and thinner wormholes than that of any other dissolution pattern. This wormhole dissolution pattern is called dominant, because it has the shortest "non-breaking through" (secondary) wormholes compared to any other wormhole dissolution pattern. Initially, in all wormhole dissolution patterns (whether conical, dominant, or ramified), several wormholes are created but only one breaks through the domain while the others die (cease to grow). This is because of the competition between the created wormholes to take in the flowing acid. This competition between the wormholes continues until one wormhole dominates or takes in all of the injected acid. The dominant wormhole dissolution pattern has the lowest wormhole competition time among all other wormhole dissolution patterns. This means that it takes less time for one wormhole to dominate in the dominant wormhole dissolution pattern. This evident form the length of secondary (non-breaking through) wormholes. It is observed that the length of these secondary (non-breaking through) wormholes are shorter in dominant wormhole dissolution pattern than in any other wormhole pattern. At this higher injection rate, the role of advection in acid transport increases and becomes comparable to the role of acid transport by diffusion. As the injection rate is increased, the Damkholer number of this dissolution pattern is decreased. The characteristic time for acid transport is comparable to the time of rock/acid reaction, hence, the dissolution is a transition between mass-transport limited and reaction limited. The amount of acid required to achieve breakthrough in this dissolution pattern is the smallest among all other dissolution patterns. This makes the dominant wormhole dissolution pattern the

most favorable dissolution pattern in matrix acidizing treatments, not only because it is the most economical, but also because it preserves the rock integrity the most.

4. Ramified Wormhole Dissolution Pattern:

This pattern occurs at a higher injection rate than that of dominant wormhole dissolution pattern. The higher injection rate not only allows the acid to reach the tip of the wormhole, but also allows the acid to penetrate through the walls of the created wormhole. This increases the diameter of the wormhole uniformly and allows the wormhole to be more branched (ramified). At this higher injection rate, the role of advection in acid transport presides, diminishing the role of acid transport by diffusion. As the injection rate is increased, the Damkholer number of this dissolution pattern is decreased. The characteristic time for acid transport is smaller than the time of rock/acid reaction, hence, the dissolution is reaction limited, meaning that the acid/rock reaction is the limiting mechanism for further rock dissolution. The amount of acid required to achieve breakthrough in this dissolution pattern is the larger than that of dominant wormhole dissolution pattern.

5. Uniform Dissolution Pattern:

This pattern occurs at higher injection rates than that of any other dissolution pattern. The very high injection rate allows the acid to reach almost every point in the entire domain. Thus, the dissolution is uniform -more or less- throughout the entire domain, without creating distinct preferential flow paths (wormholes). At this high injection rate, advection is the dominant mechanism of acid transport, and the role of diffusion is negligible. As the injection rate is increased, the Damkholer number of this dissolution pattern is decreased. The characteristic time for acid transport is much smaller than the time of rock/acid reaction, hence, the dissolution is

strongly reaction limited. The amount of acid required to achieve breakthrough in this dissolution pattern is larger than that of ramified wormhole dissolution pattern.

These five dissolution patterns match what was reported in previous experimental and numerical works. Figure 5.1(b) shows the dissolution patterns as reported by the experimental work of Fredd and Fogler[5]. While Figure 5.1(c) shows the dissolution patterns as reported by the simulations of Panga[30]. In these figures, the dissolution patterns are arranged from left to right with increasing injection rate.

5.1.2. Acidization Curve

As explained earlier, the acidization curve is a plot of the acid injection rate versus the Pore Volumes of acid injected to achieve Break Through (PVBT). Figure 5.2 shows the acidization curve from our 2D simulations. Figure 5.2(a) is the acidization curve on Cartesian scale, while Figure 5.2(b) is the same curve on a log-log scale.

It is observed that:

- The curve exhibits a concave upward shape. At low rates, the PVBT's are high. As the rate increases, the PVBT's decreases until it reaches a minimum. Then, the PVBT's increases with further increase of injection rate. This shows the presence of an optimum injection rate; a rate that breaks through the simulation domain with lowest amount of acid injected. This matches all previous experimental and numerical work. As seen from the literature, there is a consensus that the acidization curve has this concave upward shape.
- The minimum on the curve that represents the optimum injection rate corresponds to the dominant wormhole dissolution pattern. This minimum divides the curve into two parts. Below the optimum injection rate, the dominant acid transport mechanism is diffusion, the dissolution

is mass transfer limited and the dissolution patterns are either face dissolution or conical wormhole. Above the optimum injection rate, the dominant acid transport mechanism is advection, the dissolution is reaction limited and the dissolution patterns are either ramified wormhole dissolution or uniform dissolution. Again, this matches previous experimental findings. Figure 5.3 shows the acidization curve and the resulting dissolution pattern as reported experimentally by Fredd and Fogler[5].

- On plotting the acidization curve on a log-log plot, the curve exhibits a slope of one third at rates above the optimum. This is shown in Figure 5.2 (b), where the dashed line represents the one-third slope. This one-third slope was reported previously by the experimental work of Bazin[64]. Figure 5.4 shows the acidization curve one-third slope as reported by Bazin[64].

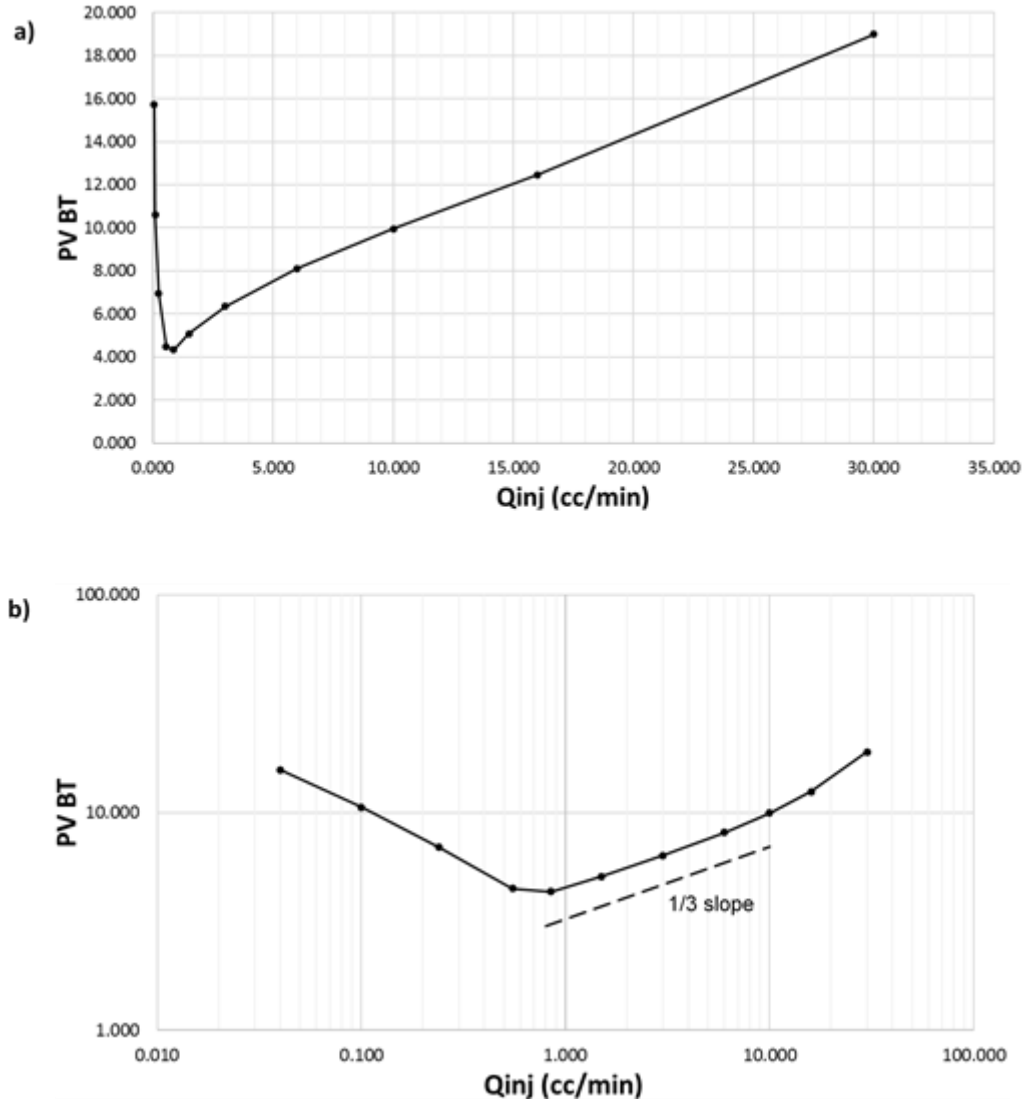

Figure 5.2 Acidization Curves from 2D RAD Simulations. Figure (a) has Cartesian scale, while figure (b) has log-log scale with the dashed line representing a slope of one third.

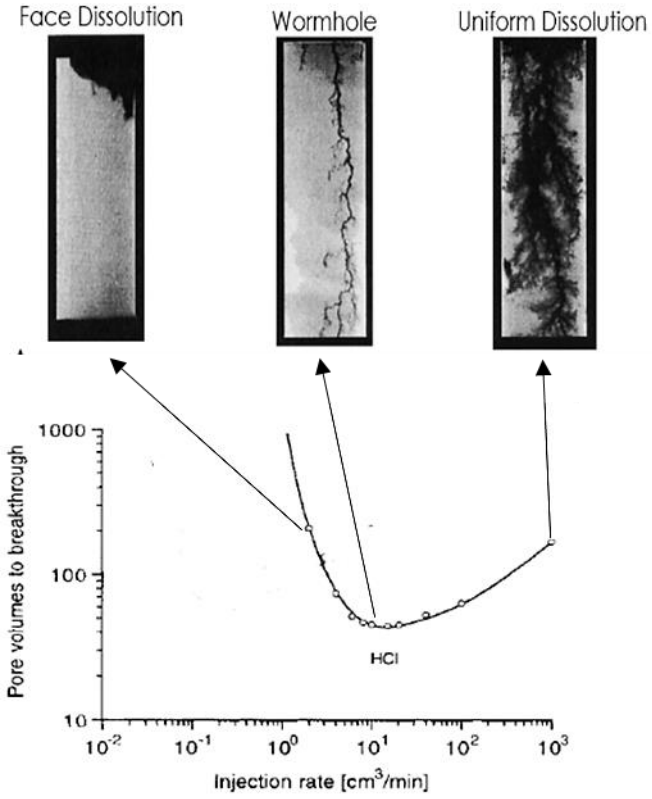

Figure 5.3 Acidization Curve and the Resulting Dissolution Pattern as Reported Experimentally by Fredd and Fogler

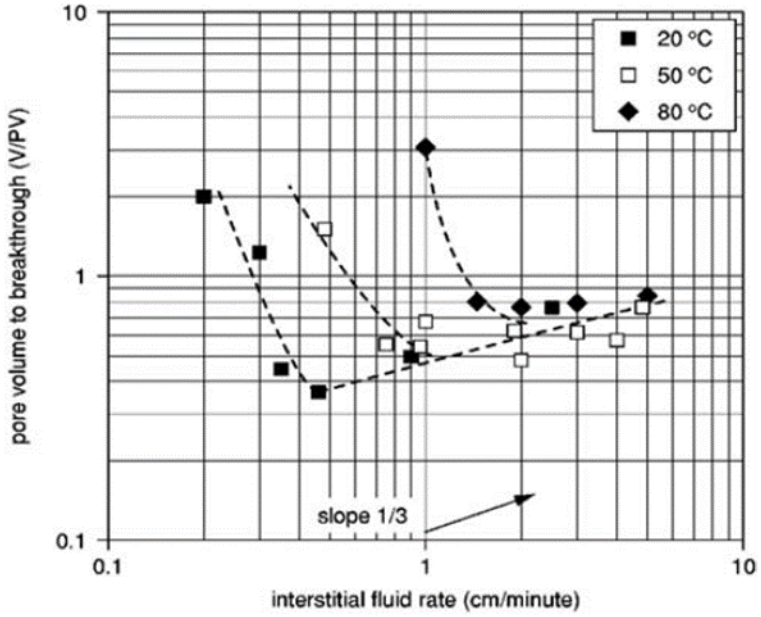

Figure 5.4 Acidization Curve at Different Temperatures as Reported Experimentally by Bazin. Notice the one-third slope for rates above the optimum.

5.2. Three-Dimensional (3D) Simulations Results and TOUGHREACT Experimental Validation

The objective of this section is to validate TOUGHREACT against real experimental work. We chose the experiments of Dong & Hill[53] because of their small core size of 1 inch by 4 inches. Details of the experimental conditions and simulation mesh was explained earlier in section 4.1.2. Figure 5.5 shows a comparison between the acidization curve of the experiments and that of our results.

It is observed that while TOUGHREACT predicts the optimum injection rate correctly, it clearly overestimates the PVBT's. This means that more acid is required to achieve breakthrough in TOUGHREACT than what was observed experimentally. This mismatch between our results and the experimental results might be due to uncertainty in some of the input parameters. These uncertainty parameters include, but not limited to;

1. Porosity and permeability initial values, distribution type, and range of distribution.
2. Porosity – permeability relationship.
3. Reactive Surface Area.
4. Reaction Rate Constant.

It is believed that using more accurate values for the above parameters can yield a better match.

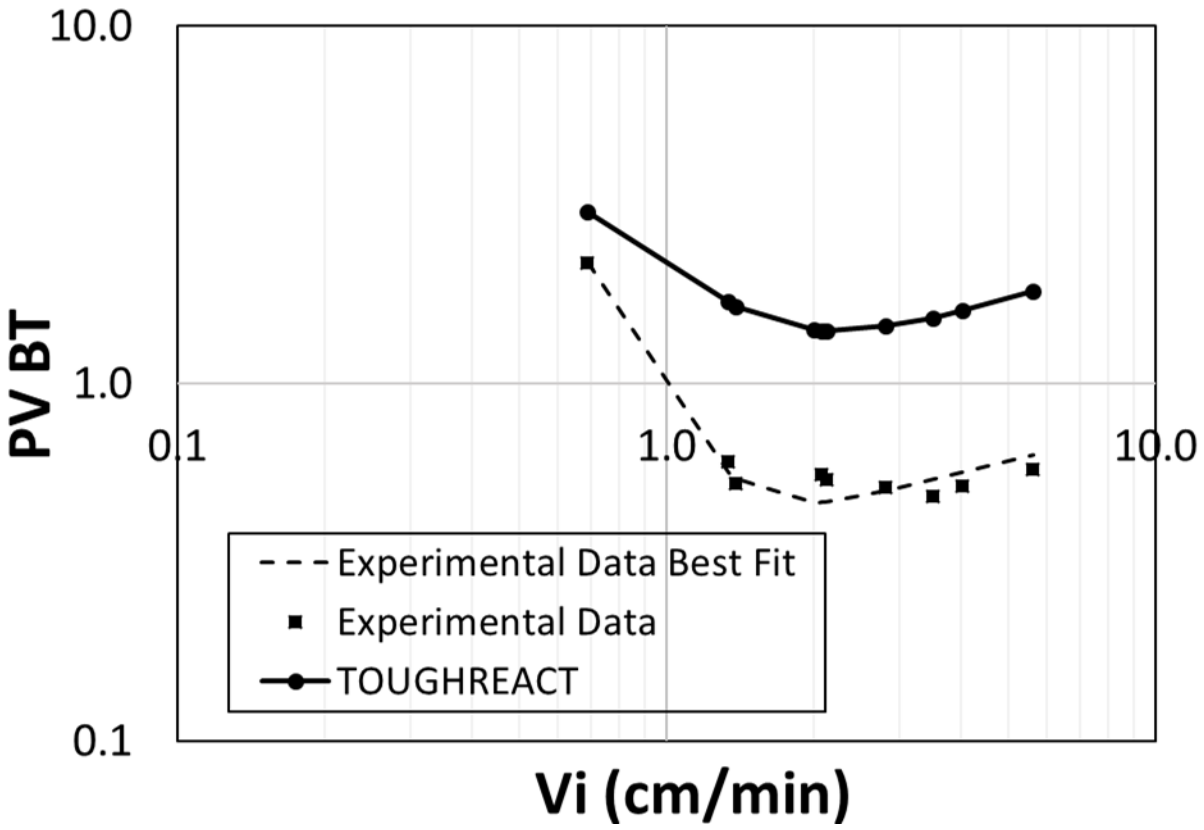

Figure 5.5 Acidization Curve Comparison Between Experimental Results and TOUGHREACT Results

5.3. Effect of Aqueous Kinetics on Acidization Curve and Dissolution Patterns

The main advantage of using TOUGHREACT in modeling matrix acidizing is that it takes into account the reactions occurring in the aqueous solution (aqueous kinetics). Aqueous kinetics were not accounted for in any of the previous models. To highlight this advantage, we compare between two types of simulations:

1-Basic Speciation: just H^+ ions reaction with calcite without any secondary species, as assumed by previous models.

2-Full Speciation: H^+ ions reaction with calcite with all the secondary species, including dissolved CO_2 species. This is the same speciation described earlier in section 4.2.1.

Table 5.1 shows the primary species, secondary species, and minerals defined in the Basic and full speciation simulations respectively.

Table 5.1 Basic and Full Speciation Systems

	Basic Speciation	Full Speciation
Primary Species	H_2O, H^+, Ca^{+2}, HCO_3^-	H_2O, H^+, Ca^{+2}, HCO_3^-, Cl-
Secondary Species	None	OH- Equation: $H^+ + OH^- \rightarrow H_2O$ HCl(aq) Equation: $HCl_{(aq)} \rightarrow H^+ + Cl^-$ $CO_{2(aq)}$ [$H_2CO_{3(aq)}$] Equation: $CO_{2(aq)} + H_2O \rightarrow H^+ + HCO3^-$ CO_3^{-2} Equation: $H^+ + CO_3^{-2} \rightarrow HCO_3^-$ $CaCO_{3(aq)}$ Equation: $H^+ + CaCO_{3\,(aq)} \rightarrow Ca^{+2} + HCO_3^-$ $CaHCO_3^+$ Equation: $CaHCO_3^+ \rightarrow Ca^{+2} + HCO_3^-$ $CaOH^+$ Equation: $CaOH^+ + H^+ \rightarrow Ca^{+2} + H_2O$ $CaCl^+$ Equation: $CaCl^+ \rightarrow Ca^{+2} + Cl^-$ $CaCl_{2(aq)}$ Equation: $CaCl_2 \rightarrow Ca^{+2} + 2Cl^-$
Mineral	$CaCO_3$ Mineral/Acid reaction is kinetically constrained. Equation: $CaCO_3 + H^+ \rightarrow Ca^{+2} + HCO_3^-$	

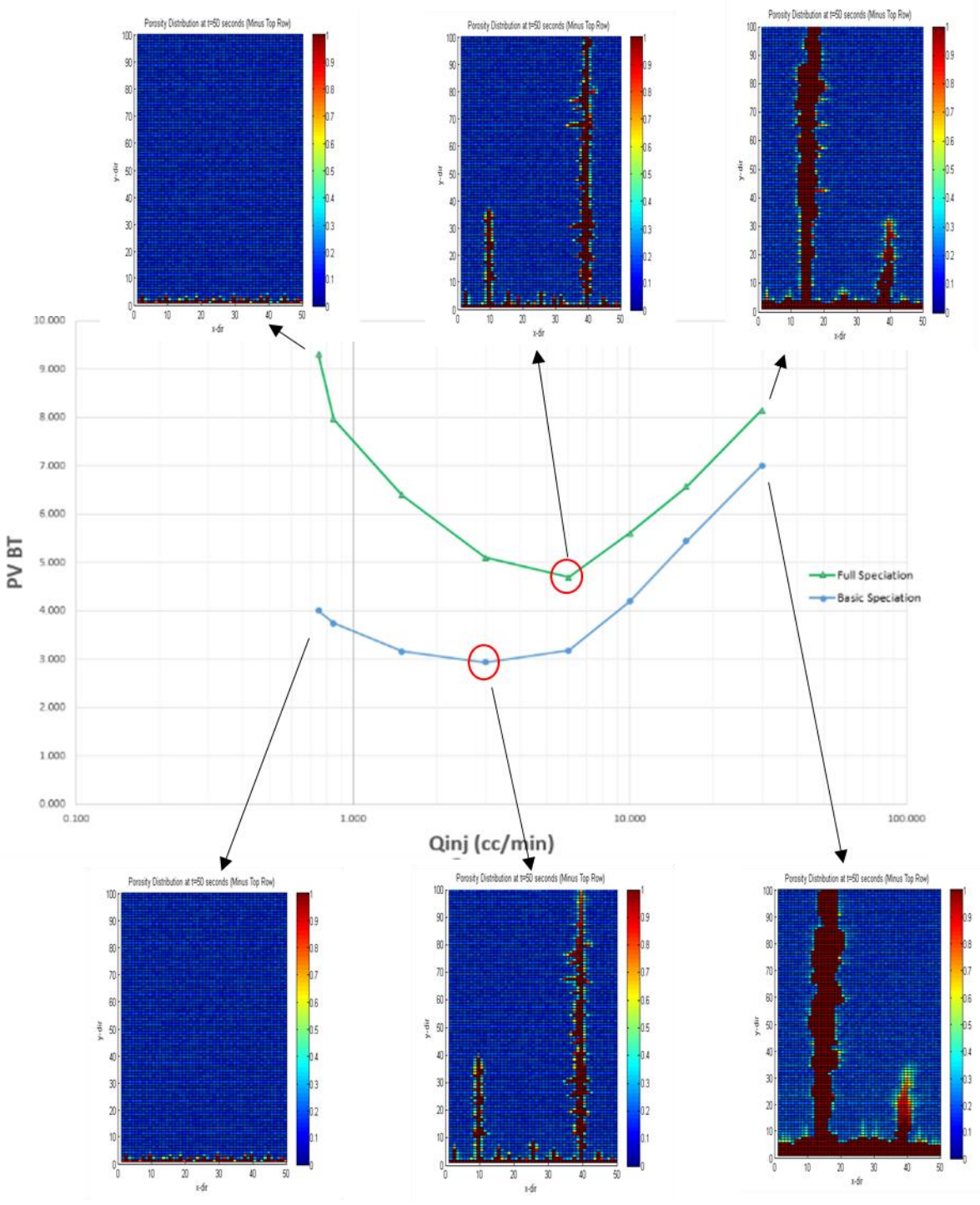

Figure 5.6 Acidization Curve and the Resulting Dissolution Pattern for Basic and Full Speciation Simulation.

Figure 5.6 shows the porosity distributions after 50 seconds of acid injection for three different injection rates for both basic and full speciation simulations. It also shows the acidization curve for both basic and full speciation simulations. It is observed that:

- There is no difference in the dissolution patterns for basic and full speciation simulations.
- There is a huge difference in the acidization curve for basic and full speciation simulations. First, the basic speciation simulation has lower PVBT when compared to full speciation simulation. Second, the basic speciation simulation has lower optimum injection rate (shown in a red circle in Figure 5.6) when compared to full speciation simulation.

The lower PVBT and optimum injection rate of basic speciation simulation compared to full speciation simulation can be explained by the fact that full speciation has less free hydrogen ions. In the full speciation simulation, due to the high acidity of the medium (low pH) most dissolved CO_2 exists as aqueous carbonic acid (H_2CO_3) as indicated by Figure (1.3). However, in basic speciation simulation, the dissolved CO_2 always exists as bicarbonate ion (HCO_3^-), simply because no other secondary species defined. As explained earlier, aqueous carbonic acid is formed by combining H^+ ion with bicarbonate ion. This makes the free hydrogen concentration in full speciation less compared to basic speciation. In other terms, it is as if the full speciation has less acid concentration compared to basic speciation. This conclusion is based on the experimental work of Wang and Hill[65], who observed similar trends when varying the acid concentration during HCl injection in limestone cores shown in Figure 5.7. The acidization curve shown on the right in figure 5.7 is the same as the one shown in figure 5.6, but with Cartesian scale instead of semi-log scale.

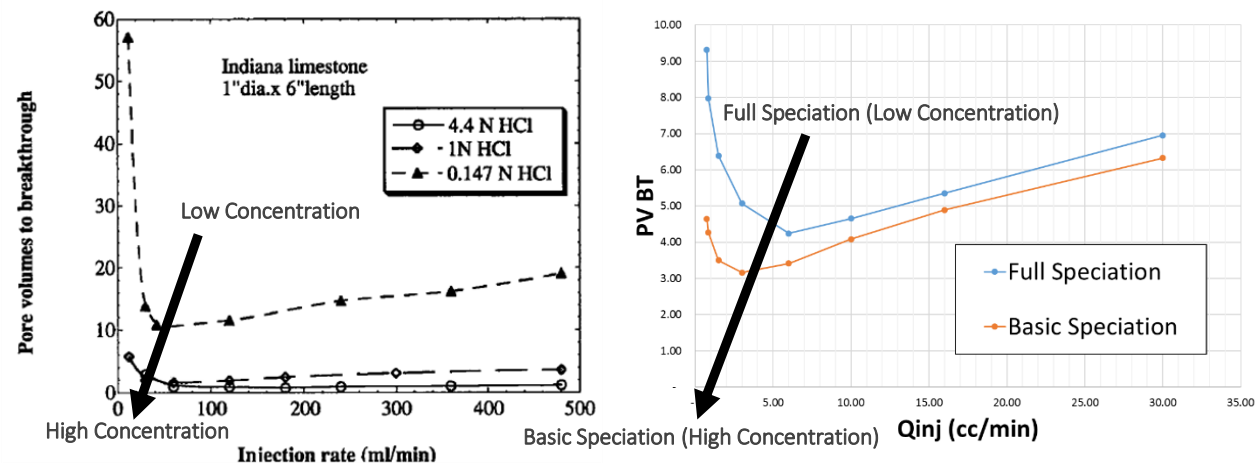

Figure 5.7 Effect of Different Acid Concentrations on the Acidization Curve After Wang and Hill (Left). Effect of Full Speciation and Basic Speciation on the Acidization Curve (Right). Notice the Similarity in Trends.

5.4. Pressure Decline Curve

As explained earlier in section 4.5, initially when the acid is injected, the pressure differential across the domain is high. As dissolution of the domain occurs, this pressure difference decreases/declines gradually till it flattens out at almost zero, which marks breakthrough. The pressure decline curve is a plot of the pressure difference with time. Figure 5.8 shows the pressure decline curve of the 2D simulations at the optimum injection rate (6 cc/min), along with the evolution of the wormhole dissolution pattern with time. It is observed that the pressure drop across the domain goes through three main stages, these are:

I. **Initial Plateau Stage:** Initially the pressure drop remains almost the same, forming a horizontal plateau on the pressure decline curve. During this stage, almost no dissolution occurs in the simulation domain, as observed in the corresponding dissolution pattern (Figure 5.8 b) which has the same porosity distribution as the initial porosity distribution (Figure 5.8 a). This initial plateau stage is brief at the optimum injection rate. However, it appears to be long in the figure because of the log scale of the x-axis. It was also observed that the length of the initial plateau stage is inversely related to the injection rate, i.e., the initial plateau stage becomes longer with lower injection rate. This is expected, since the lower the injection rate, the longer the time needed for the acid to penetrate in to the domain and to initiate the dissolution, hence the longer the initial plateau stage.

II. **Decline Stage:** As some of the simulation domain is dissolved by the injected acid, the acid flowing through the domain faces less flow resistance, and the pressure differential across the domain starts to decline. This decline in the pressure difference is initially gentle then becomes steep. The gentle decline stage corresponds to the wormhole competition period (explained earlier in section (5.1.1.3)), during which several wormholes are created without any being

dominant. This is evident from the corresponding dissolution pattern (Figures 5.8 c & d). During this stage, the created wormholes compete among each other to take-in the injected acid, until one wormhole offers the least pressure drop and becomes preferred by the acid. Once one wormhole takes-in all of the injected acid (i.e., becomes dominant), the pressure differential across the domain drops significantly, commencing the steep decline stage. The steep decline stage corresponds to the wormhole dominance period, during which one wormhole takes-in all of the injected acid. This stage favors the growth of the dominant wormhole only, until it breaks through the domain. This is indicated by the corresponding dissolution pattern (Figure 5.8 e), where it is observed that all other wormholes have ceased to grow except for the dominant one. It was also observed that the injection rate is directly related to the length of the gentle decline stage and inversely related to the steep decline stage, i.e., the gentle decline stage becomes longer and the steep decline stage becomes shorter with lower injection rate. This is also expected since at very low injection rates, the wormhole competition stage never end and a single wormhole never dominate the domain, hence the resulting dissolution pattern is always face dissolution.

III. **Final Plateau Stage:** Eventually, the dominant wormhole breaks through the domain, creating a high speed flow channel with little to no flow resistance. Thus, the pressure drop across the domain becomes almost zero and retains this state, creating another horizontal plateau. This final plateau stage occurs whether at the optimum injection rate or any other rate, i.e., it is rate-independent.

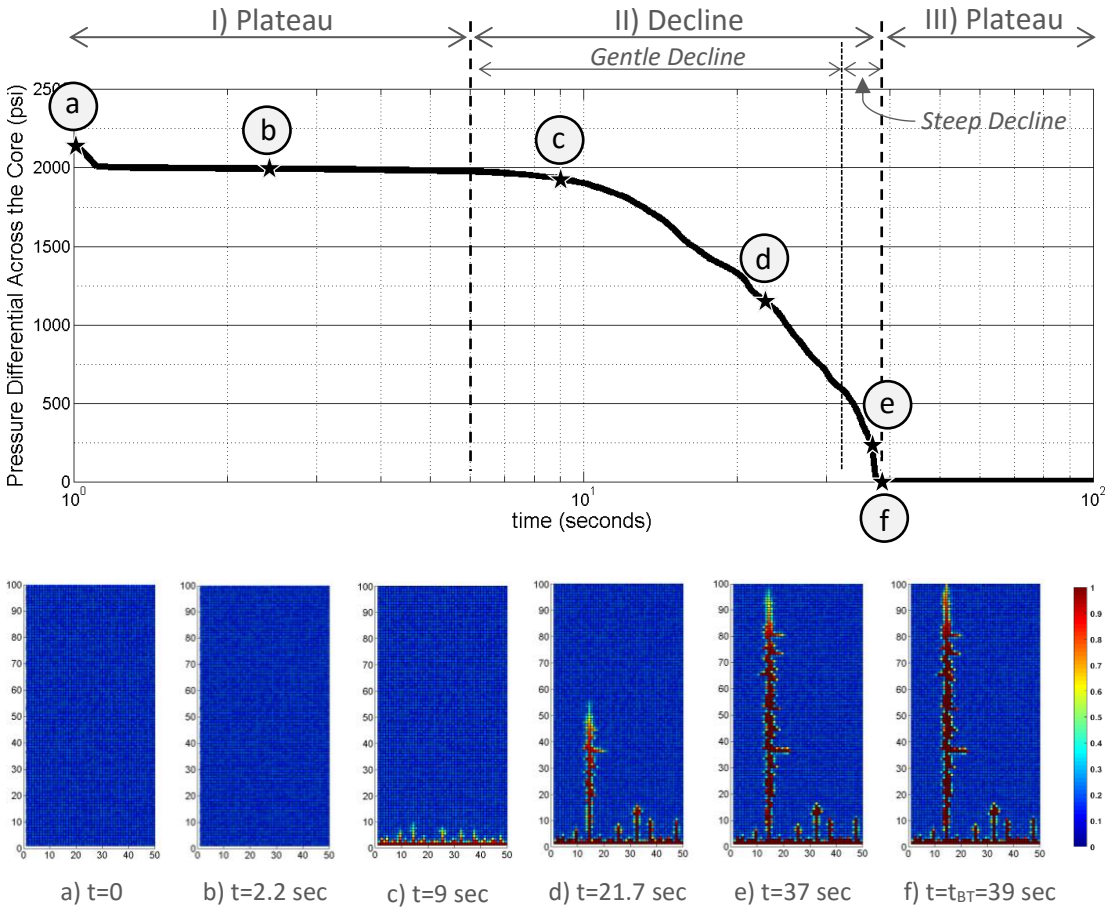

Figure 5.8 Time Evolution of Pressure Decline Curve and Dissolution Pattern at the Optimum Injection Rate.

Unfortunately, the pressure decline curve for matrix acidizing treatments gained little attention in the literature[66]. However, it is believed that, with further investigations, the pressure response during the acid injection can provide real-time feedback of the dissolution progress during the treatment. It can also help diagnose the treatment failure or success in post-treatment analysis.

CHAPTER 6

CONCLUSIONS & RECOMMENDATIONS

6.1. Conclusions

1. A new application is introduced to the geochemical code TOUGHREACT. The model used in TOUGHREACT considers aqueous kinetics and performs full-speciation transport.
2. The new model capability of capturing the qualitative trend of the acidization curve being concave upwards is demonstrated using 2D simulations. This confirms the existence of an optimum injection rate.
3. Two dimensional simulations were used to demonstrate the ability of the model to capture the different dissolution patterns reported experimentally.
4. When validated against previous experimental work, the new model predicts the optimum injection rate correctly, but overestimates the volumes of acid injected.
5. Aqueous kinetics and full speciation transport simulations reduces the effective hydrogen ions concentration compared to previous models. This, in turn, affects the optimum injection rate and the volumes of acid injected.
6. When compared to basic speciation simulations, the full speciation simulations have higher optimum injection rates and higher volumes of acid injected.

6.2. Recommendations

For future work, we recommend the following:

1. Performing sensitivity analysis for the uncertainty input parameters used in simulating matrix acidizing.

2. Extending the work to other acid/rock combinations.

3. Extending the work to non-isothermal simulations, as this topic has gained little attention in the literature[67].

4. Extending the work to radial flow geometry, to investigate the following aspects:

    4.1. Extending the work from constant injection rate to increasing injection rate in a radial flow geometry.

    4.2. Extending the work to different aspect ratios, to investigate the existence of a critical aspect ratio[67 & 68] for radial flow geometry.

5. Extending the work from single phase (acid only) to two-phase (acid/CO_2) to take into account the effect of non-dissolved CO_2 as a separate phase.

Appendix A: Scripts for TOUGHREACT Modules Compilation

Appendix A.1. Module EOS1 Compilation Script:

```
----------------------------------------
#!/bin/sh

module purge

module load Intel_Compilers Intel_MPI

echo ''

echo 'Compiling Toughreact V3.0-OMP'

echo ''

rm *.o

make eos1 -f makefile_linux_intel

echo ''

echo 'Done Compiling Toughreact V3.0-OMP'

echo ''
----------------------------------------
```

Appendix A.2. Module ECO2N Compilation Script:

```
----------------------------------------
#!/bin/sh

module purge

module load Intel_Compilers Intel_MPI

echo ''

echo 'Compiling Toughreact V3.0-OMP'

echo ''

rm *.o

make eco2n -f makefile_linux_intel

echo ''

echo 'Done Compiling Toughreact V3.0-OMP'

echo ''
----------------------------------------
```

Appendix B: Scripts for Submitting Jobs to the HPC Cluster

Appendix B.1. Module EOS1 Job Submission Script:

```
----------------------------------------
#!/bin/bash -l

#BSUB -q high_priority

#BSUB -eo error.err

#BSUB -oo output.out

#BSUB -J  fortran

#BSUB -n  N

module purge

module load Intel_Compilers Intel_MPI

echo '---------  START -------------'

mpirun -np N  ./treactv3omp_eos1_linux_intel > out.log

echo '-------- END   ----------------'
----------------------------------------
```

Appendix B.2. Module ECO2N Job Submission Script:

```
----------------------------------------
#!/bin/bash -l

#BSUB -q high_priority

#BSUB -eo error.err

#BSUB -oo output.out

#BSUB -J  fortran

#BSUB -n  N

module purge all

module load Intel_Compilers Intel_MPI

echo '---------  START -------------'

mpirun -np N  ./treactv3omp_eco2n_linux_intel> out.log

echo '-------- END   ----------------'
----------------------------------------
```

Appendix C: Comparison between Reported Equilibrium Constants for Aqueous Reactions

For OH^-:

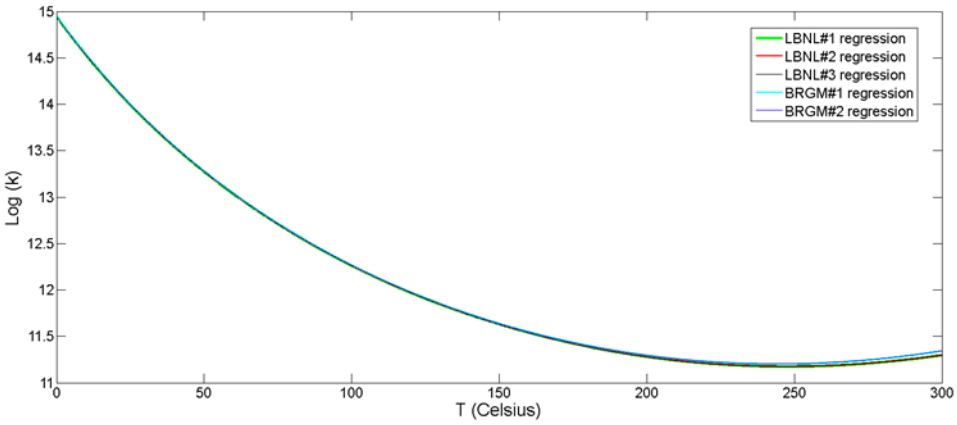

Figure C.1 Comparison in Reported Equilibrium Constant Variation with Temperature for OH^- Ion Reaction from Different Thermodynamic Databases

For $HCl_{(aq)}$:

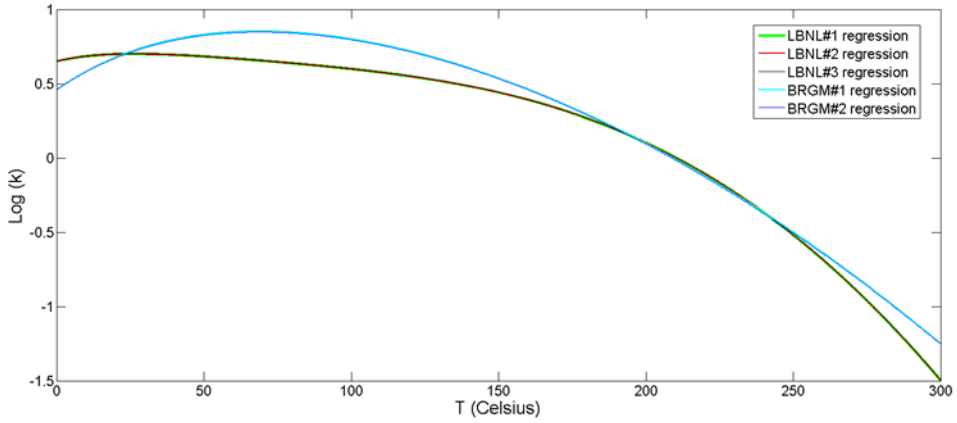

Figure C.2 Comparison in Reported Equilibrium Constant Variation with Temperature for aqueous HCl Reaction from Different Thermodynamic Databases

For $CO_{2(aq)}$:

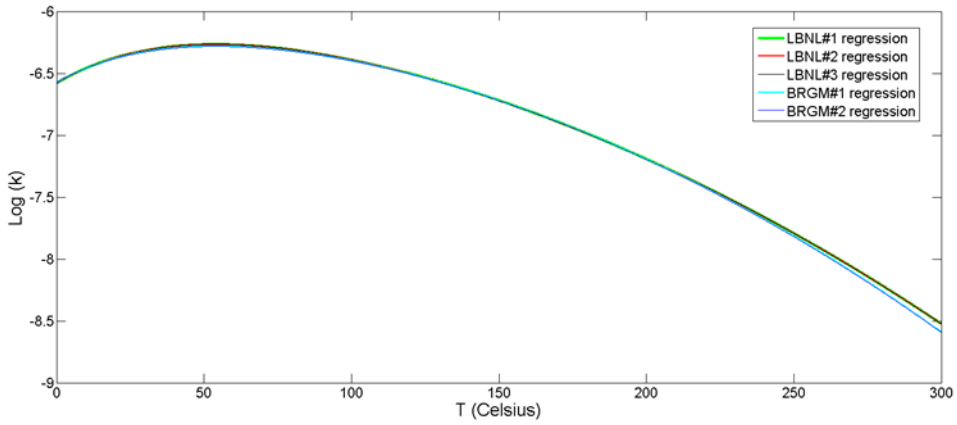

Figure C.3 Comparison in Reported Equilibrium Constant Variation with Temperature for aqueous CO_2 Reaction from Different Thermodynamic Databases.

For CO_3^{-2}

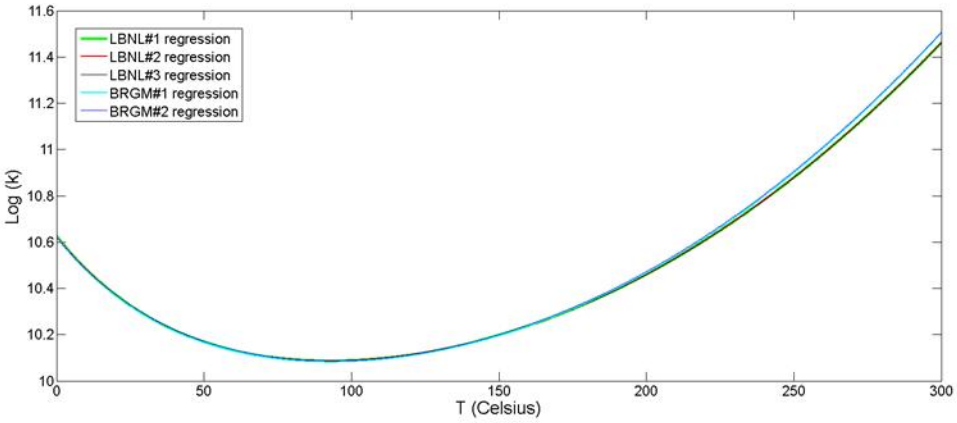

Figure C.4 Comparison in Reported Equilibrium Constant Variation with Temperature for Carbonate (CO_3^{-2}) Ion Reaction from Different Thermodynamic Databases.

For $CaOH^+$:

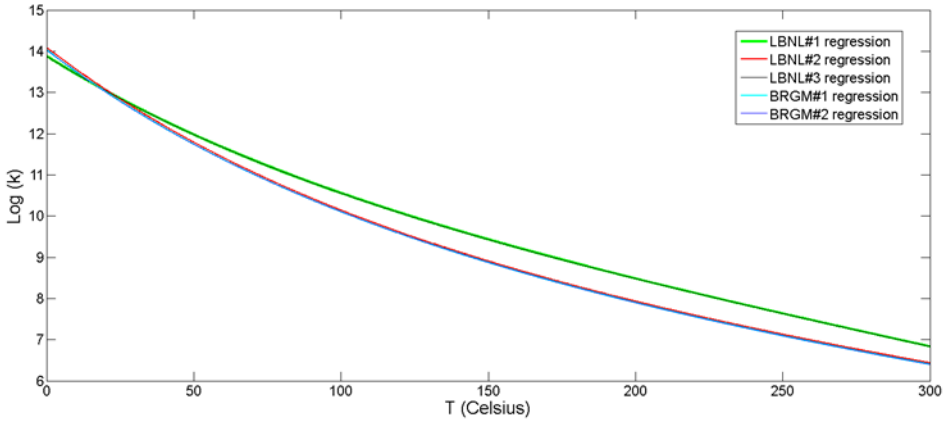

Figure C.5 Comparison in Reported Equilibrium Constant Variation with Temperature for Calcium Hydroxide Ion ($CaOH^+$) Ion Reaction from Different Thermodynamic Databases

For $CaCl^+$:

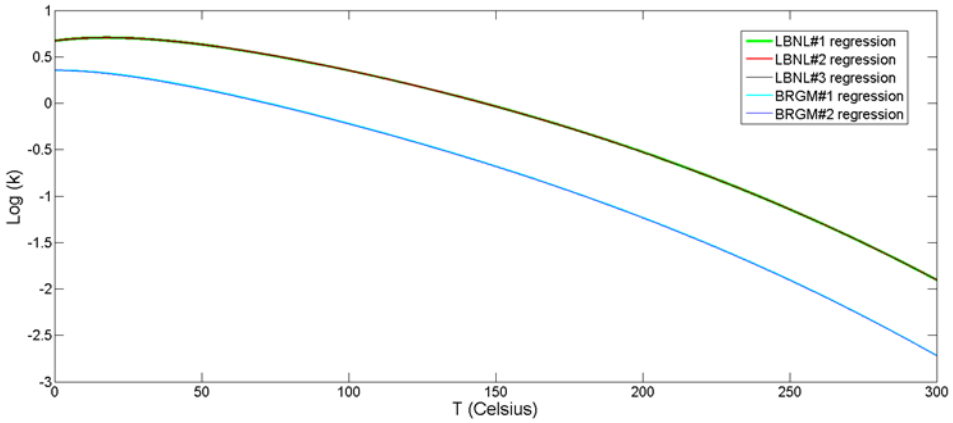

Figure C.6 Comparison in Reported Equilibrium Constant Variation with Temperature for Calcium Chloride ($CaCl^+$) Ion Reaction from Different Thermodynamic Databases

For $CaCl_{2(aq)}$:

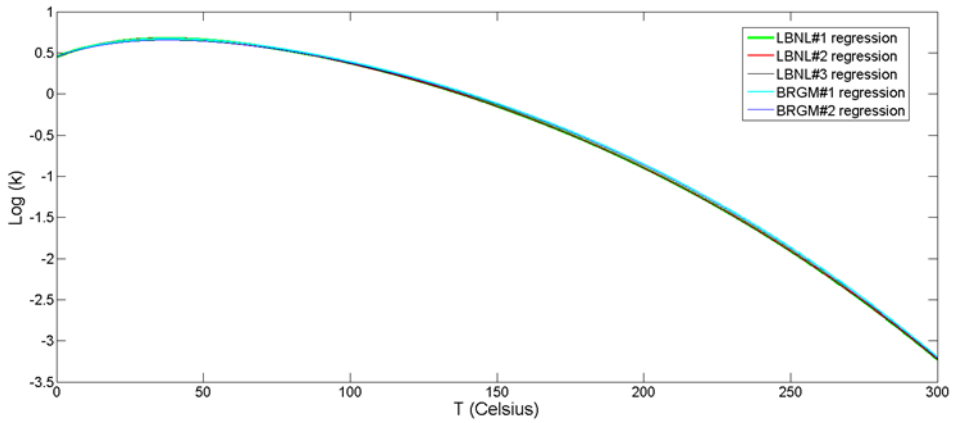

Figure C.7 Comparison in Reported Equilibrium Constant Variation with Temperature for Aqueous Calcium Chloride ($CaCl_{2(aq)}$) Reaction from Different Thermodynamic Databases

For $CaCO_{3(aq)}$:

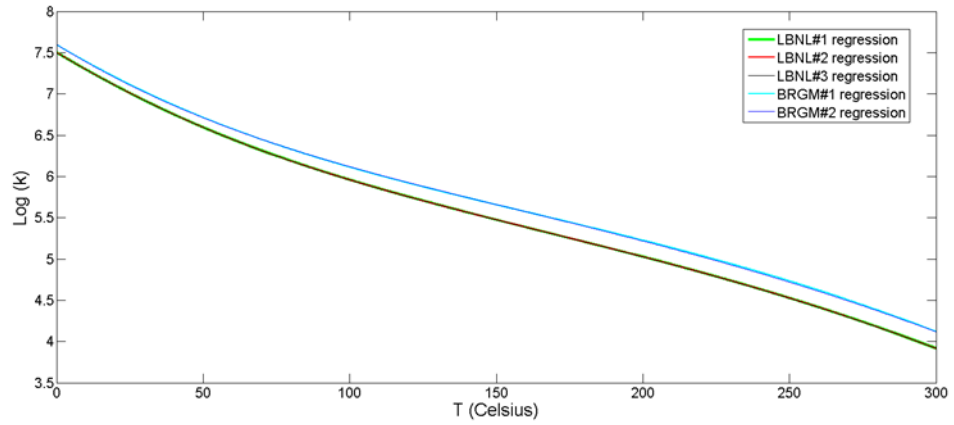

Figure C.8 Comparison in Reported Equilibrium Constant Variation with Temperature for Aqueous Calcium Carbonate ($CaCO_{3(aq)}$) Reaction from Different Thermodynamic Databases

For $CaCO_{3(aq)}$:

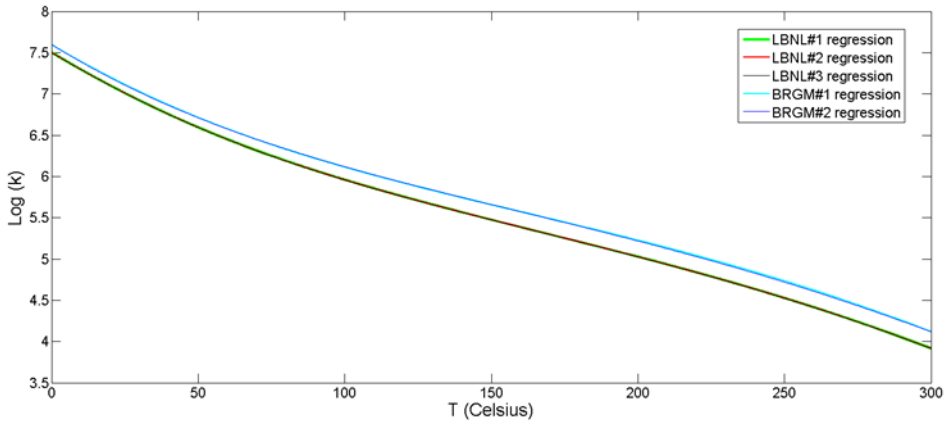

Figure C.9 Comparison in Reported Equilibrium Constant Variation with Temperature for Aqueous Calcium Carbonate ($CaCO_{3(aq)}$) Reaction from Different Thermodynamic Databases

References

1. Bert B. Williams, John L. Gidley, R. S. S. *Acidizing Fundamentals*. (SPE Monohraph Series, 1979).

2. Maheshwari P., Ratnakar R.R., Kalia N., B. V. 3-D simulation and analysis of reactive dissolution and wormhole formation in carbonate rocks. *Chem. Eng. Sci.* 90, 258–274 (2013).

3. Ghommem, M., Zhao, W., Dyer, S., Qiu, X. & Brady, D. Journal of Petroleum Science and Engineering Carbonate acidizing : Modeling , analysis , and characterization of wormhole formation and propagation. *J. Pet. Sci. Eng.* 131, 18–33 (2015)

4. Golfier, F. *et al.* Acidizing Carbonate Reservoirs: Numerical Modelling of Wormhole Propagation and Comparison to Experiments. in *SPE European Formation Damage Conference* (2001). doi:10.2523/68922-MS

5. Fredd, C. N., Fogler, H. S. & Michigan, U. Alternative Stimulation Fluids and Their Impact on Carbonate Acidizing. *Spe J.* 34–41 (1998).

6. Perkins, E. *Fundamental Geochemical Processes Between CO2 , Water and Minerals*.

7. Diamond, L. W. & Akinfiev, N. N. Solubility of CO 2 in water from − 1 . 5 to 100 ◦ C and from 0 . 1 to 100 MPa : evaluation of literature data and thermodynamic modelling. *Fluid Phase Equilib.* 208, 265–290 (2003).

8. Ertekin, T. (SPE T. S. V. 7. *Basic Applied Reservoir Simulation*. (Society of Petroleum Engineers, 2001).

9. Yuan, J., Babchin, A. & Tremblay, B. Modeling Wormhole Flow in Cold Production. in *49th Annual Technical Meeting of The Petroleum Society, Calgary, Alberta, Canada* (The Petroleum Society, 1998).

10. Hung, K. M., Hili, A. D. & Sepehrnoorl, K. A Mechanistic Model of Wormhole Growth in Carbonate Matrix Acidizing and Acid Fracturing. *J. Pet. Technol.* 59–66 (1989).

11. Huang, T Hill, A.D. Schechter, R. S. Reaction Rate and Fluid Loss- The Keys to Wormhole Initiation and Propagation in Carbonate Acidizing.pdf. in *SPE International Symposium on Oilfield Chemistry, Houston, Texas* (1997).

12. Huang, T., Hill, A. D., Schechter, R. S. & Texas, U. Reaction Rate and Fluid Loss : The Keys to Wormhole Initiation and Propagation in Carbonate Acidizing. *Spe J.* 5 (3), 287–292 (2000).

13. Istchenko, C. M. & Gates, I. D. Well / Wormhole Model of Cold Heavy-Oil Production With Sand. in *SPE Heavy Oil Conference and Exhibition, Kuwait City, Kuwait* (2014).

14. Gong, M. & El-Rabaa, A. M. Quantitative Model of Wormholing Process in Carbonate Acidizing. in *SPE Mid-Continent Operations Symposium, Oklahoma City, Oklahoma.* (1999).

15. Buijse, M., E, S. I. & Glasbergen, G. A Semiempirical Model T o Calculate Wormhole Growth in Carbonate Acidizing. in *SPE Annual Technical Conference and Exhibition, Dallas, Texas, U.S.A.* (2005).

16. Daccord, G., Touboul, E., Lenormand, R. & Schlumberger, D. Carbonate Acidizing : Toward a Quantitative Model of the Wormholing Phenomenon. *SPE Prod. Eng.* 63–68 (1989).

17. Pichler, T., Frick, T. P., Economides, M. J., Leoben, M. U. & Nittmann, J. Stochastic Modeling of Wormhole Growth in Carbonate Acidizing With Biased Randomness. in *The European Petroleum Conference, Cannes, France* (1992).

18. Xiaogang, L., Jie, T. & Zhaozhong, Y. Simulation of Wormhole in Carbonate Acidizing Using a New Diffusion Limited Aggregation Model. in *International Conference on Computational and Information Sciences* (2010). doi:10.1109/ICCIS.2010.89

19. Steefel, C. I., Depaolo, D. J. & Lichtner, P. C. Reactive transport modeling : An essential tool and a new research approach for the Earth sciences. *Earth Planet. Sci. Lett.* 240, 539–558 (2005).

20. Hoefner, M. L., Fogler, H. S. & Michigan, U. Fluid-Velocity and Reaction-Rate Effects During Carbonate Acidizing : Application of Network Model. *SPE Prod. Eng.* (1989).

21. Fogler, H. S. Competition Among Flow , Dissolution , and Precipitation in Porous Media Competition Among Flow , Dissolution , and Precipitation in Porous Media. *AIChE J.* 35, 1177–1185 (1989).

22. Yuan, J., Tremblay, B. & Babchin, A. A Wormhole Network Model of Cold Production in Heavy Oil. in *SPE International Thermal Operations and Heavy Oil Symposium, Bakersfield, California* (1999).

23. Buijse, M. A. Understanding Wormholing Mechanisms Can Improve Acid Treatments in Carbonate Formations. *SPE Prod. Facil.* 15 (3), 168–175 (2000).

24. Tansey, J. & Division, M. S. Pore-Network Modeling of Carbonate Acidization. in *SPE International Student Paper Contest at the SPE Annual Technical Conference and Exhibition, Amsterdam, The Netherlands.* (2014).

25. Daccord, G., Lenormand, R. & Liétard, O. Chemical dissolution of a porous medium by a reactive fluid — I. Model for the 'wormholing' phenomenon. *Chem. Eng. Sci.* 48, 169–178 (1993).

26. Daccord, G., Liétard, O. & Lenormand, R. Chemical dissolution of a porous medium by a reactive fluid—II. Convection vs reaction, behavior diagram. *Chem. Eng. Sci.* 48, 179–186 (1993).

27. Edouard, C., Ding, D., Quintard, M. & Bazin, B. From pore scale to wellbore scale : Impact of geometry on wormhole growth in carbonate acidization. *Chem. Eng. Sci.* 63, 3088–3099 (2008).

28. Li, L., Peters, C. A. & Celia, M. A. Upscaling geochemical reaction rates using pore-scale network modeling. *Adv. Water Resour.* 29, 1351–1370 (2006).

29. Panga, M., Balakotaiah, V. & Ziauddin, M. Modeling, simulation and comparison of models for wormhole formation during matrix stimulation of carbonates. (2003).

30. Panga, M. K. R., Ziauddin, M. & Land, S. Two-Scale Continuum Model for Simulation of Wormholes in Carbonate Acidization. *AIChE J.* 51, 3231–3248 (2005).

31. Panga, M., Ziauddin, M., Gandikota, R. & Balakotaiah, V. A New Model for Predicting Wormhole Structure and Formation in Acid Stimulation of Carbonates. in *SPE International Symposium and Exhibition on Formation Damage Control, Lafayette, Louisiana.* (2004). doi:10.2523/86517-MS

32. Kalia, N. & Balakotaiah, V. Modeling and analysis of wormhole formation in reactive dissolution of carbonate rocks. *Chem. Eng. Sci.* 62, 919–928 (2006).

33. Izgec, O., Zhu, D. & Hill, A. D. Numerical and experimental investigation of acid wormholing during acidization of vuggy carbonate rocks. *J. Pet. Sci. Eng.* 74, 51–66 (2010).

34. Liu, M., Zhang, S. & Mou, J. Effect of normally distributed porosities on dissolution pattern in carbonate acidizing. *J. Pet. Sci. Eng.* 94–95, 28–39 (2012).

35. Liu, M., Zhang, S. & Mou, J. Fractal nature of acid-etched wormholes and the influence of acid type on wormholes. *Pet. Explor. Dev.* 39, 630–635 (2012).

36. Ratnakar, R. R., Kalia, N. & Balakotaiah, V. Modeling, analysis and simulation of wormhole formation in carbonate rocks with in situ cross-linked acids. *Chem. Eng. Sci.* 90, 179–99 (2013).

37. Maheshwari, P. & Balakotaiah, V. Comparison of Carbonate HCl Acidizing Experiments With 3D Simulations. *SPE Prod. Oper.* 402–413 (2013). doi:10.2118/164517-PA

38. Maheshwari, P., Maxey, J. & Balakotaiah, V. Reactive-Dissolution Modeling and Experimental Comparison of Wormhole Formation in Carbonates With Gelled and Emulsified Acids. *SPE Prod. Oper.* (2015).

39. Daccord, G. Chemical Dissolution of a Porous Medium by a Reactive Fluid. *Phys. Rev. Lett.* 58, 479–482 (1987).

40. Frick, T. P., Mostofizadeh, B., Leoben, M. U. & Economides, M. J. Analysis of Radial Core Experiments for Hydrochloric Acid Interaction With Limestones. in *SPE international Symposium and Exhibition on Formation Damage Control, Lafayette, Louisiana.* 577–592 (1994).

41. Mostofizadeh, B. & Economides, M. J. Optimum Injection Rate From Radial Acidizing Experiments. in *SPE 69th Annual Technical Conference and Exhibition, New Orleans, LA, U.S.A.* 327–333 (1994).

42. McDuff, D., Jackson, S., Shuchart, C. & Postl, D. Understanding Wormholes in Carbonates: Unprecedented Experimental Scale and 3D Visualization. *J. Pet. Technol.* 62, 78–81 (2010).

43. Xu, T., Sonnenthal, E., Spycher, N. & Zheng, L. *TOUGHREACT V3.0-OMP Reference Manual: A Parallel Simulation Program for Non-Isothermal Multiphase Geochemical Reactive Transport*. (2014).

44. Hao, Y., Smith, M., Sholokhova, Y. & Carroll, S. Advances in Water Resources CO 2 - induced dissolution of low permeability carbonates . Part II : Numerical modeling of experiments. *Adv. Water Resour.* 62, 388–408 (2013).

45. Audigane, P., Azaroual, M., Menjoz, A. & Andre, L. Numerical modeling of fluid – rock chemical interactions at the supercritical CO 2 – liquid interface during CO 2 injection into a carbonate reservoir , the Dogger aquifer (Paris Basin , France). 48, 1782–1797 (2007).

46. Yu, Z., Liu, L., Liu, K., Yang, S. & Yang, Y. Petrological characterization and reactive transport simulation of a high-water-cut oil reservoir in the Southern Songliao Basin, Eastern China for CO2 sequestration. *Int. J. Greenh. Gas Control* 37, 191–212 (2015).

47. Varloteaux, C., Békri, S. & Adler, P. M. Pore network modelling to determine the transport properties in presence of a reactive fluid: From pore to reservoir scale. *Adv. Water Resour.* 53, 87–100 (2013).

48. Elkhoury, J. E., Ameli, P. & Detwiler, R. L. Dissolution and deformation in fractured carbonates caused by flow of CO2-rich brine under reservoir conditions. *Int. J. Greenh. Gas Control* 16, Supple, S203–S215 (2013).

49. Flukiger, F. & Bernard, D. A new numerical model for pore scale dissolution of calcite due to CO2 saturated water flow in 3D realistic geometry: Principles and first results. *Chem. Geol.* 265, 171–180 (2009).

50. Sadhukhan, S., Gouze, P. & Dutta, T. Porosity and permeability changes in sedimentary rocks induced by injection of reactive fluid: A simulation model. *J. Hydrol.* 450-451, 134–139 (2012).

51. Qiu, X. W. *et al.* Revisiting Reaction Kinetics and Wormholing Phenomena During Carbonate Acidizing. *International Petroleum Technology Conference, Doha, Qatar* (2014).

52. Xu, T., E.L. Sonnenthal, N. Spycher, and K. Pruess, TOUGHREACT - A simulation program for non-isothermal multiphase reactive geochemical transport in variably saturated geologic media: Applications to geothermal injectivity and CO2 geological sequestration, Computers & Geosciences, v.32, p.145-165, 2006.

53. Dong, K., Jin, X., Zhu, D., & Hill, A. D. (2014, February 26). The Effect of Core Dimensions on the Optimal Acid Flux in Carbonate Acidizing. Society of Petroleum Engineers. doi:10.2118/168146-MS.

54. Morel, Francois MM, and Janet G. Hering. Principles and applications of aquatic chemistry. John Wiley & Sons, 1993.

55. Wolery, Thomas J. EQ3/6: A software package for geochemical modeling of aqueous systems: package overview and installation guide (version 7.0). Livermore, CA: Lawrence Livermore National Laboratory, 1992.

56. Kong, Xiang-Zhao, Benjamin M. Tutolo, and Martin O. Saar. "DBCreate: A SUPCRT92-based program for producing EQ3/6, TOUGHREACT, and GWB thermodynamic databases at user-defined T and P." Computers & geosciences 51 (2013): 415-417.

57. Blanc, P., Lassin, A., Piantone, P., Azaroual, M., Jacquemet, N., Fabbri, A., & Gaucher, E. C. (2012). Thermoddem: A geochemical database focused on low temperature water/rock interactions and waste materials. Applied Geochemistry, 27(10), 2107-2116.

58. Thermoddem.brgm.fr. (2017). Toughreact database - Thermoddem. [online] Available at: http://thermoddem.brgm.fr/spip.php/rubrique14

59. Parkhurst, D. L., & Appelo, C. A. J. (1999). User's guide to PHREEQC (Version 2): A computer program for speciation, batch-reaction, one-dimensional transport, and inverse geochemical calculations.

60. Perry, R. H., & Green, D. W. (2008). Perry's chemical engineers' handbook. New York: McGraw-Hill.

61. Conway, M. W., Asadi, M., Penny, G. S., & Chang, F. (1999, January 1). A Comparative Study of Straight/Gelled/Emulsified Hydrochloric Acid Diffusivity Coefficient Using Diaphragm Cell and Rotating Disk. Society of Petroleum Engineers. doi:10.2118/56532-MS

62. Schechter, R. S. (1992). Oil well stimulation.

63. Lund, K., Fogler, H. S., McCune, C. C., & Ault, J. W. (1973, January 1). Kinetic Rate Expressions for Reactions of Selected Minerals with HCl and HF Mixtures. Society of Petroleum Engineers. doi:10.2118/4348-MS.

64. Bazin, B. (2001, February 1). From Matrix Acidizing to Acid Fracturing: A Laboratory Evaluation of Acid/Rock Interactions. Society of Petroleum Engineers. doi:10.2118/66566-PA.

65. Wang, Y., Hill, A. D., & Schechter, R. S. (1993, January 1). The Optimum Injection Rate for Matrix Acidizing of Carbonate Formations. Society of Petroleum Engineers. doi:10.2118/26578-MS

66. Ghommem, M., & Brady, D. (2016, April 25). Multifidelity Modeling and Analysis of Matrix Acidizing Under Radial Flow Conditions. Society of Petroleum Engineers. doi:10.2118/182743-MS.

67. Kalia, N., & Glasbergen, G. (2010, January 1). Fluid Temperature as a Design Parameter in Carbonate Matrix Acidizing. Society of Petroleum Engineers. doi:10.2118/135654-MS

68. Kalia, N., & Balakotaiah, V. Effect of medium heterogeneities on reactive dissolution of carbonates, Chemical Engineering Science, Volume 64, Issue 2, January 2009, Pages 376-390, ISSN 0009-2509, https://doi.org/10.1016/j.ces.2008.10.026.

Vitae

Name	: Mohamed Sherif Mostafa Kamal Mahrous
Nationality	: Egypt
Date of Birth	: 24th March 1991
Email	: m.mahrous91@gmail.com
Address	: 1(m) Ali Gad El-Hak street, Cairo, Egypt.
Academic Background	: B.Sc. in Petroleum Engineering, Faculty of Petroleum and Mining Engineering, Suez University, Egypt.